DISS. ETH No. 26419

# Narrow band gap Cu(In,Ga)$Se_2$ for tandem solar cell application

A thesis submitted to attain the degree of

DOCTOR OF SCIENCES of ETH ZURICH

(Dr. sc. ETH Zurich)

presented by

**Thomas Feurer**

Master of science ETH, Physik

born on 11.11.1983

citizen of Switzerland

accepted on the recommendation of

Prof. Dr. Ayodhya N. Tiwari, examiner

Prof. Dr. Susanne Siebentritt, co-examiner

Prof. Dr. Jüerg Leuthold, co-examiner

Dr. Stephan Bücheler, co-examiner

2019

# Contents

# Abstract

Photovoltaic (PV) energy generation has become one of the key pillars of the shift to a renewable energy future. Current devices, under favorable conditions, can already undercut the price per kWh electricity of other technologies on the market. Further reduction in the cost of installed PV systems and increase in solar module conversion efficiency will improve the affordability even more and will substantially aid in wider market penetration and enhance the volume of PV installations.

Currently the PV market is dominated by silicon wafer based solar cells, but alternative technologies offer some distinctive advantages, making them interesting for numerous applications. Thin film technologies, as for example based on $Cu(In,Ga)Se_2$ (CIGS) compound semiconductors with high optical absorption coefficient, are becoming important due to lower material and energy requirements for processing of high conversion efficiency solar cells. Inherent advantages are large area depositions with low production costs, and the possibilities for construction of lightweight, flexible devices with roll-to-roll manufacturing processes.

The highest efficiency of single-junction CIGS solar cells is approaching the thermodynamic limit, making the use of alternative concepts such as concentration or multi-junction (tandem-) devices the next logical step for further increase in efficiency beyond the Shockley-Queisser limit (S-Q limit). Especially the multi-junction technology, in which the thermodynamic losses are reduced by stacking of solar cells with different band gaps, decreasing thermalization of charge carriers excited with energies above the band gap, is a promising approach for enhanced utilization of the solar spectrum, yielding improved efficiency. Such devices, based on epitaxial layers of III-V compounds have already demon-

strated remarkably high efficiencies beyond the S-Q limit. However, these devices grown on rather expensive single crystal wafers and with small size are prohibitively pricey for low cost terrestrial solar electricity generation. On the other hand, multi-junction solar cell technology based on polycrystalline thin films is an attractive option for large area, low cost production, provided adequately high efficiencies are achieved. In this context, two-junction tandem devices, developed by stacking a semitransparent large band gap solar cell of 1.6-1.7 eV on top of a low band gap (~1.0 eV) bottom cell, is a viable option. Earlier attempts in this direction were not so successful, but with the rise of perovskite thin film solar cells as a compatible high efficiency wide band gap (>1.6 eV) top cell and CIGS with a tunable band gap as bottom cell, the prospect for all thin film tandem devices with efficiencies beyond the single-junction limitations has opened. Such all thin film devices hold the potential for the low cost production necessary for large scale terrestrial application.

This thesis focuses on the development of high efficiency narrow bandgap (1.0 eV) CIGS solar cells for application in all thin film tandem devices.

While for CIGS with band gap of around 1.15 eV efficiencies of over 23 % have been demonstrated, cells with a narrow band gap close to 1.0 eV only reach 15.0 %. The efficiency of these narrow band gap cells are limited by charge carrier recombination, leading to low open circuit voltage ($V_{OC}$) and reduced fill factor. For solar cell efficiency enhancement it is necessary to investigate the underlying reasons contributing to the deficits in PV parameters and develop processes to overcome the limiting factors.

An option to reduce recombination within the solar cell is the implementation of a band gap grading as discussed in Chapter 3. The increase of the band gap at the location of highest recombination leads to a reduction in diode current, and therefore an increase in $V_{OC}$. To keep the band gap of 1.0 eV a substantial part of the absorber needs to be Ga free. As the primary source of recombination is not obvious, different gradings (realized by a change in the Ga to In ratio) are implemented and compared. A single grading with increased band gap (higher Ga/In ratio) towards the front of the absorber shows no significant improvement on photovoltaic parameters. Any gain in $V_{OC}$ is offset by losses

in current due to reduced charge collection, mainly visible for long wavelength photons and probably a result of the upwards bending in the conduction band. A single back-grading (higher Ga/In ratio towards the back electric contact) on the other hand leads to substantial improvements in performance ($\eta$ from 12.0 % to 16.1 %). It is shown that the collection of photo-generated charge carriers improves and recombination is reduced. Measurements of the effective lifetime by time resolved photo-luminescence are carried out, showing an increase from approximately 20 ns to 100 ns when comparing ungraded with back-graded absorbers. By selectively changing the recombination speed at the back contact, strong differences in the behavior of cells with and without a band gap widening towards the back are observed. The results support that considerable recombination at the back contact is present in pure CIS solar cells, and that the single Ga back-grading approach is effective at suppressing this loss channel.

In Chapter 4 the alkali treatment of CIS based solar cells is investigated. Alkali elements are known to strongly influence doping and passivation in CIGS solar cells. It is shown that the amount of sodium necessary to reach sufficient doping levels for high performance CIS solar cells is not achieved using the processes developed for CIGS. This may be based on insufficient Na diffusion into the grain, as those cells generally show larger grains than their CIGS counter parts, and since alkali migration energies in CIS are reported to be higher compared to those in CGS. If CIS cells are grown on soda lime glass without any diffusion barrier and additionally receive post deposition treatment (PDT) with NaF they still show low apparent doping concentration and poor PV performance ($\eta$ = 10.9 %). However, additional annealing at $\sim$ 370 °C substrate temperature after PDT is shown to solve this problem, leading to an increase in apparent doping levels close to $10^{16}$ cm$^{-3}$ and cell efficiency of 15.0 %. The application of an additional heavy alkali PDT, specifically RbF, is shown to lead to further improvements in cell efficiency. Changes at the front interface due to the PDT allow a decrease of buffer layer thickness, leading to a higher photo current (approximately + 1.0 mAcm$^{-2}$). In addition, reduced recombination and the resulting increase in lifetime leads to additional gains in $V_{OC}$, resulting in considerably improved device performance, up to an efficiency of 18.0 %.

Further efficiency improvement is achieved by investigating the effect of close to sto-

ichiometric compositions of Cu to group III elements as described in Chapter 5. The sub-stoichiometric Cu composition of state-of-the-art CIGS absorbers leads to a high concentration of detrimental defects. The defect density within the absorbers is reduced by approaching a stoichiometric Cu composition. Improvements in the defect density are identified by the decrease of Urbach energy from 20 to 16 mV and an increase in doping is observed for cells with almost stoichiometric Cu content. Cells with high, and especially stoichiometric Cu composition tend to be limited by recombination at the front interface, leading to a decrease of $V_{OC}$ of about 20 mV. Using the modified absorber surface after heavy alkali PDT, these losses are suppressed. Based on these improvements, a narrow band gap cell with record breaking 19.2 % efficiency and an open circuit voltage of 609 mV is achieved.

Throughout the whole thesis the suitability of these cells for tandem devices with semi-transparent perovskite top cells is investigated by 4-terminal tandem measurements. The improvements achieved in this work led to CIS based solar cells that not only show outstanding single cell performance, but also enable highly efficient tandem devices up to 25.0 %. They outperform state-of-the-art single junction CIGS and perovskite cells while showing prospects for further efficiency improvement. Due to the low band gap of the CIS absorber the current density from the bottom cell is high enough to produce current matched tandem devices with high efficient perovskite top cells (19.2 to 18.6 $mAcm^{-2}$ in 4-terminal configuration), and also monolithic two-terminal configurations are feasible in the future.

# Zusammenfassung (Abstract in German)

Die Photovoltaik (PV) ist zu einer der wichtigsten Säulen für die Umstellung auf erneuerbare Energien geworden. Aktuelle Solarzellen können, unter günstigen Bedingungen, bereits den Preis pro kWh Strom anderer auf dem Markt befindlicher Technologien unterbieten. Eine weitere Senkung der Kosten für PV-Anlagen und eine Steigerung der Effizienz von Solarmodulen werden die Erschwinglichkeit noch weiter verbessern, die Marktdurchdringung erheblich fördern und die Menge installierter Solaranlagen erhöhen.

Derzeit wird der PV-Markt von Solarzellen auf Siliziumwafer-Basis dominiert. Alternative Technologien bieten jedoch einige besondere Vorteile, die sie für zahlreiche Anwendungen interessant machen. Dünnschichttechnologien, beispielsweise auf Basis von $Cu(In,Ga)Se_2$ (CIGS) Halbleitern mit hohem optischen Absorptionskoeffizienten, gewinnen aufgrund des geringeren Material- und Energiebedarfs für die Herstellung von Solarzellen mit hohem Umwandlungswirkungsgrad an Bedeutung. Inhärente Vorteile sind grossflächige Abscheidungen mit geringen Produktionskosten und die Möglichkeiten für den Bau leichter, flexibler Module mit Rolle-zu-Rolle Herstellungsprozessen.

Der höchste Wirkungsgrad von Einzel-Absorber CIGS-Solarzellen nähert sich der thermodynamischen Grenze und macht die Verwendung alternativer Konzepte wie Konzentrations- oder Mehrfach-Absorber- (Tandem-) Solarzellen zum nächsten logischen Schritt, um den Wirkungsgrad über die Shockley-Queisser-Grenze (SQ-Grenze) hinaus weiter zu steigern. Insbesondere die Mehrfachsolarzellentechnologie, bei der die thermodynamischen Verluste durch Stapeln von Solarzellen mit unterschiedlichen Bandlücken reduziert werden, wodurch die Thermalisierung von Ladungsträgern, die mit Energien oberhalb der Bandlücke angeregt werden, verringert wird, sind ein vielversprechender Ansatz zur verbesserten

Nutzung des Sonnenspektrums für verbesserte Effizienz. Derartige Solarzellen, basierend auf epitaktischen Schichten von III-V-Halbleitern, haben bereits bemerkenswert hohe Wirkungsgrade jenseits der S-Q-Grenze gezeigt. Diese Zellen, die auf ziemlich teuren und kleinen Einkristallwafern gewachsen sind, sind jedoch für eine kostengünstige terrestrische Solarstromerzeugung unerschwinglich teuer. Andererseits ist die Mehrfachsolarzellentechnologie auf der Basis von polykristallinen Dünnfilmen eine attraktive Option für eine grossflächige und kostengünstige Produktion, vorausgesetzt, es werden ausreichend hohe Wirkungsgrade erzielt. In diesem Zusammenhang sind Tandemzellen mit zwei Absorbern, die durch Stapeln einer halbtransparenten Solarzelle mit grosser Bandlücke von 1,6 bis 1,7 eV auf eine untere Zelle mit geringer Bandlücke (~1,0 eV) hergestellt werden, eine praktikable Option. Frühere Versuche in diese Richtung waren nicht sehr erfolgreich, aber mit dem Aufstieg von Perowskit-Dünnschichtsolarzellen als kompatiblen hocheffizienten Partner mit grosser Bandlücke (>1,6 eV) als Oberzelle und CIGS mit abstimmbarer Bandlücke als Unterzelle sind steigen die Aussichten auf komplett Dünnschicht Tandemsolarzellen mit Wirkungsgraden jenseits der Beschränkungen für Einzelzellen. Solche Solarzellen, vollständig auf Dünnschicht-Zellen aufgebaut, besitzen das Potential für eine kostengünstige Produktion, die für eine grossflächige terrestrische Anwendung erforderlich ist.

Diese Dissertation befasst sich mit der Entwicklung von hocheffizienten CIGS-Solarzellen mit schmaler Bandlücke (1.0 eV) für die Anwendung in voll-Dünnschicht Tandemsolarzellen.

Während für CIGS mit einer Bandlücke von etwa 1,15 eV Wirkungsgrade von über 23% nachgewiesen wurden, erreichen Zellen mit einer engen Bandlücke nahe 1,0 eV nur 15,0 %. Die Effizienz dieser Zellen mit schmaler Bandlücke wird durch die Rekombination der Ladungsträger begrenzt, was zu einer niedrigen Leerlaufspannung ($V_{OC}$) und einem verringerten Füllfaktor führt. Für die Effizienzsteigerung dieser Solarzellen ist es notwendig, die zugrunde liegenden Gründe zu untersuchen, die zu den Defiziten in PV-Parametern beitragen, und Prozesse zu entwickeln, um die begrenzenden Faktoren zu überwinden.

Eine Möglichkeit, die Rekombination innerhalb der Solarzelle zu reduzieren, ist die Implementierung eines Bandlückenverlaufs, wie in Kapitel 3 beschrieben. Die Zunahme der Bandlücke am Ort der höchsten Rekombination führt zu einer Verringerung des Dioden-

stroms und daher zu einer Zunahme des $V_{OC}$. Um die Bandlücke von 1,0 eV zu erhalten, muss ein wesentlicher Teil des Absorbers Ga-frei sein. Da die primäre Quelle der Rekombination nicht offensichtlich ist, werden verschiedene Bandlückenverläufe (die durch eine Änderung des Verhältnisses von Ga zu In realisiert werden) implementiert und verglichen. Eine vergrösserte Bandlücke (höheres Ga / In-Verhältnis) zur Vorderseite des Absorbers hin zeigt keine signifikante Verbesserung der photovoltaischen Parameter. Jeder Gewinn im $V_{OC}$ wird durch Stromverluste aufgrund einer verringerten Ladungsträgersammlung ausgeglichen, die hauptsächlich für langwellige Photonen sichtbar ist und wahrscheinlich auf die Aufwärtsbiegung des Leitungsbandes zurückzuführen ist. Eine Bandlückenerweiterung zum Rückkontakt führt andererseits zu wesentlichen Leistungsverbesserungen (von 12,0 % auf 16,1 %). Es wird gezeigt, dass sich die Sammlung von durch Licht erzeugten Ladungsträgern verbessert und die Rekombination verringert wird. Es werden Messungen durch zeitaufgelöste Photolumineszenz durchgeführt, die einen Anstieg der effektiven Lebensdauer von ungefähr 20 ns auf 100 ns durch den Bandlückengradienten zeigen. Durch gezielte Änderung der Rekombinationsgeschwindigkeit am Rück-kontakt werden starke Unterschiede im Verhalten von Zellen mit und ohne Bandlückenegradienten nach hinten festgestellt. Die Ergebnisse belegen, dass in reinen CIS-Solarzellen eine beträchtliche Rekombination am Rückkontakt vorliegt und dass der Ansatz eines einfachen Ga-Gradienten diesen Verlustkanal wirksam unterdrückt.

In Kapitel 4 wird die Alkalibehandlung von CIS-basierten Solarzellen untersucht. Es ist bekannt, dass Alkalielemente die Dotierung und Passivierung von CIGS-Solarzellen stark beeinflussen. Es hat sich gezeigt, dass mit den für CIGS entwickelten Verfahren die zur Erreichung ausreichender Dotierungsniveaus für Hochleistungs-CIS-Solarzellen erforderliche Natriummenge nicht erreicht wird. Dies kann auf einer unzureichenden Na-Diffusion in die Kristalle beruhen, da diese Zellen im Allgemeinen grössere Kristallkörner aufweisen als ihre CIGS-Gegenstücke, und da berichtet wird, dass die Alkalimigrationsenergien in CIS im Vergleich zu denen in CGS höher sind. Wenn CIS-Zellen auf Natronkalkglas ohne Diffusionsbarriere gewachsen werden und zusätzlich eine Nachbehandlung (PDT) mit NaF erhalten, zeigen sie immer noch eine geringe Dotierungskonzentration und eine schlechte PV-Leistung ($\eta$ = 10,9 %). Es hat sich jedoch gezeigt, dass ein zusätzliches Tempern

bei einer Substrattemperatur von ~ 370 °C nach PDT dieses Problem löst, was zu einem Anstieg des Dotierungsniveaus auf etwa 10 $^{16}$ cm$^{-3}$ und Zelleffizienz von 15,0 % führt. Es wird gezeigt, dass die Anwendung eines zusätzlichen schweren Alkali-PDT, insbesondere von RbF, zu weiteren Verbesserungen der Zelleffizienz führt. Änderungen an der vorderen Grenzfläche aufgrund des PDT ermöglichen eine Verringerung der Pufferschichtdicke, was zu einem höheren Photostrom führt (ungefähr +1,0 mAcm$^{-2}$). Darüber hinaus führt eine verringerte Rekombination und die sich daraus ergebende Verlängerung der Lebensdauer zu zusätzlichen Gewinnen im $V_{OC}$, was zu einer erheblich verbesserten Effizienz bis zu einem Wirkungsgrad von 18,0 % führt.

Eine weitere Verbesserung der Effizienz wird durch die Untersuchung des Effekts nahezu stöchiometrischer Zusammensetzungen von Cu zu den Elementen der Gruppe III erreicht, wie in Kapitel 5 beschrieben. Die unterstöchiometrische Cu-Zusammensetzung moderner CIGS-Absorber führt zu einer hohen Konzentration schädlicher Defekte. Die Defektdichte innerhalb der Absorber wird durch Annäherung an eine stöchiometrische Cu-Zusammensetzung verringert. Verbesserungen der Defektdichte sind durch die Abnahme der Urbach-Energie von 20 auf 16 mV zu erkennen, und bei Zellen mit nahezu stöchiometrischem Cu-Gehalt wird eine Erhöhung der Dotierung beobachtet. Zellen mit einer hohen und insbesondere stöchiometrischen Cu-Zusammensetzung neigen dazu, durch Rekombination an der vorderen Grenzfläche begrenzt zu werden, was zu einer Abnahme des $V_{OC}$ um etwa 20 mV führt. Durch die modifizierte Grenzfläche nach dem RbF PDT werden diese Verluste unterdrückt. Basierend auf diesen Verbesserungen wird eine Solarzelle mit schmaler Bandlücke mit einem Rekordwirkungsgrad von 19,2 % und einer Leerlaufspannung von 609 mV erreicht.

In der gesamten Arbeit wird die Eignung dieser Zellen für Tandemzellen mit semitransparenten Perowskit-Topzellen durch 4-Kontakt Tandemmessungen untersucht. Die Verbesserungen, die in dieser Arbeit beschrieben werden, führten zu CIS-basierten Solarzellen, die nicht nur eine hervorragende Einzelzellenleistung aufweisen, sondern auch hocheffiziente Tandemzellen bis zu 25,0 % ermöglichen. Sie übertreffen die besten CIGS- und Perowskit- Einzelzellen und zeigen den Weg für weitere Effizienzverbesserungen auf. Aufgrund der geringen Bandlücke des CIS-Absorbers ist die Stromdichte von der unteren

Zelle hoch genug, um stromangepasste Tandemzellen mit hocheffizienten Perowskit Solarzellen zu erreichen (19,2 zu 18,6 $mAcm^{-2}$ in 4-Kontakt Geometrie). In Zukunft sind daher auch monolithische Konfigurationen mit nur zwei Kontakten möglich.

# List of abbreviations

| | |
|---|---|
| Al:ZnO | Aluminium doped zinc oxide |
| ALD | Atomic layer deposition |
| AR coating | Anti reflection coating |
| AS | Admitance spectroscopy |
| ATP | Atom probe tomography |
| BIPV | Building integrated photovoltaic |
| BOS | Balance of system |
| CBD | Chemical bath deposition |
| CBM | Conduction band maximum |
| CGI | Cu to Ga+In ratio |
| CIS | $CuInSe_2$ |
| CIGS | $Cu(In,Ga)Se_2$ |
| CV | Capacitance-Voltage |
| Cf | Capacitance-frequency |
| EDX | Energy-dispersive X-ray spectroscopy |
| Eff / $\eta$ | Efficiency |
| EQE | External quantum efficiency |
| FF | Fill factor |
| GGI | Ga to Ga+In ratio |
| I-V | Current - Voltage |

| | |
|---|---|
| i-ZnO | Intrinsic ZnO |
| ICP-MS | Inductively coupled plasma mass spectrometry |
| ICP-OES | Inductively coupled optical emission spectrometry |
| IEA | International energy agency |
| IR | Infrared |
| IZO | Indium zinc oxide |
| J-V | Current density - Voltage |
| $J_{SC}$ | Short circuit current density |
| NIR | Near Infrared |
| PDT | Post deposition treatment |
| PI | Polyimide |
| PL | Photoluminescence |
| PV | Photovoltaic |
| SEM | Scanning electron microscopy |
| SLG | Soda lime glass |
| SQ | Shockley - Queisser |
| T-IV | Temperature dependent current - voltage |
| TCO | Transparent conductive oxide |
| TIPV | Transport integrated photovoltaic |
| TMM | Transfer matrix method |
| TOF-SIMS | Time of flight secondary ion mass spectrometry |
| TR-PL | Time resolved photoluminescence |
| UV-Vis | Ultraviolet - visible |
| $V_{OC}$ | Open-circuit voltage |
| XRD | X-ray diffraction |
| XRF | X-ray fluorescence |

# 1 Introduction

This chapter is partly based on the following publication:

[1] T. Feurer, P. Reinhard, E. Avancini, B. Bissig, J. Löckinger, P. Fuchs, R. Carron, T. P. Weiss, J. Perrenoud, S. Stutterheim, S. Buecheler, and A. N. Tiwari, *Progress in thin film CIGS photovoltaics - Research and development, manufacturing, and applications*, Progress in Photovoltaics: Research and Applications, Volume 25, 2017, Pages 645-667

## 1.1 Motivation

The world energy demand is expected to increase by more than one quarter from now to 2040 as projected by the international energy agency (IEA) [2]. At the same time, a large part of the worlds countries have agreed to reduce greenhouse gas emission in order to limit the global temperature increase to below 2 °C [3]. This can only be achieved by shifting large parts of energy generation from fossil fuels to renewable sources. Key technologies to facilitate this transfer are solar power and solar electricity in large scale deployment. Solar photovoltaic is already one of the cheapest forms of electricity under favorable conditions [4]. Nonetheless it is important to continue the development of these technologies by increasing efficiency and reducing the costs, making solar power the most competitive choice on the market.

## 1.2 Solar cells

Solar cells are photovoltaic devices that transform light directly into electricity. They operate on the basis of the photovoltaic effect, first demonstrated by Edmond Becquerel in 1839. Today, solar cells are a rapidly growing market. Silicon waver based technologies dominate the field with a share of almost 96 %, distributed about 2/3 in multi-crystalline and 1/3 in mono-crystalline silicon (c-Si). The remaining production is mostly thin-film technologies (~4.5 GWp/year), dominated by CdTe and Cu(In,Ga)$Se_2$ (CIGS) [5]. While their efficiencies are still lower than c-Si, those technologies offer several other advantages such as low material use, potential for low cost production, production of flexible devices and the possibility to modify the band gap by changes in composition. Moreover, the energy payback time and environmental impact for thin film modules is considerably lower than for traditional silicon [6].

As costs of solar cells and modules have decreased sharply over the last decade, the cost structure involved for residential or utility scale solar energy production has changed as well. The cost portion assigned to the actual solar modules in a rooftop PV-system in Germany has decreased from 71 % to 45 % between 2006 and 2018 [5]. The additional expenses (hardware, labor, inverters...), called balance of system costs (BOS), now take up more than half of the total system costs. As a result, increasing the efficiency of the solar cells without substantially raising the module cost becomes an important factor to improve the competitiveness to other power generation technologies.

## 1.3 CIGS solar cells

This thesis discusses CIGS-based thin film solar cells, one of the most promising photovoltaic technologie today. Key advantages of CIGS compared to other conventional photovoltaic technologies include the high energy yield (kWh/KWp installed), low temperature coefficient of power loss, low sensitivity to shadowing and short energy payback time [7–9]. Cost projections down to 0.35 Euro/Wp have been announced for the current technology, with potential for further reduction upon scale-up, allowing a significant reduction of the

total system cost [10]. The possibility to grow thin films of large area absorber onto a glass as well as light-weight, flexible substrates opens up the field for low-cost manufacturing methods as well as new applications. Applications such as building-integrated PV (BIPV), transport-integrated PV (TIPV), space flight or mobile power generation are market segments where those type of solar modules have greatest advantage compared with traditional PV technologies [11]. Champion cell efficiencies have been steadily increasing, with up to 23.35% [12] reported for laboratory scale absorbers. Efficiencies above 20% have been achieved on rigid and flexible substrates by different research institutes as well as industrial companies (see overview in Table 1.1).

The band-gap of CIGS semiconductor materials is determined by the composition of the absorber, more specifically on the ratio of Ga to In as well as Se to S or in some cases Ag to Cu. To a minor amount, the Cu excess in the absorber may also influence the band-gap of the material [13], but in our experiments we could not find a significant influence [14].

CIGS is often used as a general abbreviation for chalcopyrite solar cells based on the Cu(In,Ga)$Se_2$ system, even when additional elements such as S or Ag are added in non negligible amounts. Currently there is an annual production capacity of about 2 GWp installed world wide [5], with significant additions announced by several producers.

### 1.3.1 State of the art high efficiency CIGS solar cells

Research labs and companies around the world are working on CIGS. A short selection, highlighting the different deposition techniques and substrates used, can be found in Table 1.1. There is also a large number of other groups, working on the fundamental understanding of the material system, characterization, different deposition methods and new structures not listed here.

### 1.3.2 State of narrow bandgap CIS

While Table 1.1 represents the state of the art efficiency for traditional, double-graded CIGS with band gaps mostly in the range of 1.3-1.3 eV, this work in particular is looking

Table 1.1: CIGS cell efficiency at a few different research institutes and companies worldwide, highlighting the different technologies used for CIGS layer growth and solar cell processing. Cells marked with * are independently certified.

| Institute | Country | Cell $\eta$ [%] | Ref. | CIGS deposition method | Substrate | Notes |
|---|---|---|---|---|---|---|
| Solar Frontier | Japan | 23.35* | [12] | Sputtering, selenization & sulfurization (CIGSSe) | Glass | With NEDO and AIST |
| ZSW | Germany | 22.6* | [15] | Co-evaporation (CIGSe) | Glass | - |
| NREL | USA | 20.8 | [16] | Co-evaporation (CIGSe) | Glass | - |
| | | 18.6 | [17] | Evaporation & selenization | Glass | Zn(O,S) buffer layer |
| Toshiba | Japan | 20.7 | [18] | Co-evaporation (CIGSe) | Glass | - |
| Empa | CH | 20.8* | [19] | Co-evaporation (CIGSe) | PI | Flexible polyimide |
| AIST | Japan | 20.0 | [20] | Co-evaporation (CIGSe) | GaAs | Single-crystal absorber |
| IEC Delaware | USA | 19.9 | [21] | Co-evaporation (AgCIGSe) | HT Glass | Wide band gap (Ag,Cu)(In,Ga)Se2 |
| AGU | Japan | 19.7* | [22] | Sputtering, selenization & sulfurization (CIGSSe) | Glass | Zn(O,S) buffer layer, with Solar Frontier |
| | | 18.4 | [23] | Co-evaporation (CIGSe) | Glass | Zn(O,S) buffer layer |
| HZB | Germany | 19.4* | [24] | Co-evaporation (CIGSe) | Glass | High growth temperature (>600 °C) |
| | | 16.1* | [25] | Sputtering, selenization & sulfurization (CIGSSe) | | Zn(O,S) |
| Uppsala | Sweden | 18.6 | [26] | Co-evaporation (CIGSe) | Glass | In-line |
| IRDEP | France | 17.3* | [27] | Electrodeposition and selenisation (CIGSSe) | Glass | Solution-based precursor, with Nexcis |
| NREL | USA | 11.7* | [28] | Electrodeposition & selenization (CIGSe) | Glass | Solution-based precursor |
| IBM | USA | 15.2* | [29] | Hydrazine-based (CIGSSe) | Glass | Pure solution |

at narrow band-gap (1.0 eV) absorbers. The published record for a solar cell based on an absorber with band-gap of 1.00 eV was 15.0% efficiency at the start of this thesis, shown by AbuShama of NREL already in 2005 [30]. Since then, CIS has mostly been used as a model to investigate fundamental properties in the CIGS material system, for example to investigate the electronic structure [31], the defect distribution [32] or the doping [33].

### 1.3.3 Device structure

Figure 1.1 shows the typical structure of a CIGS solar cell, indicating some commonly used materials for the different layers. The most widespread substrate is rigid, 3-4mm thick soda-lime glass (SLG), as it is thermally stable, chemically inert and has a similar thermal expansion coefficient as the absorber. It also has a smooth surface, insulating properties suitable for monolithic interconnection and can supply alkali elements for high efficient cells (see Section1.3.5). However, a significant amount of work has also been done for CIGS on flexible substrates such as metal foils, ceramics and polymer films, as discussed in more details in a review by Reinhard et al. [34].

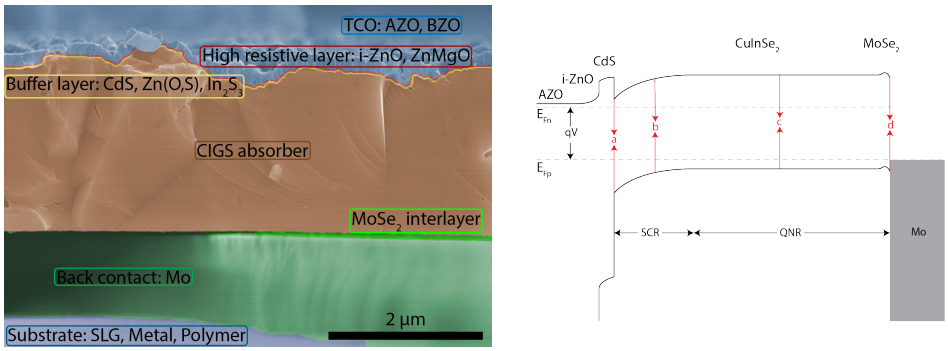


Figure 1.1: (left) Exemplary cross-section of a CIGS solar cell with the different layers marked an labeled. (right) Schematic band diagram of a CIS solar cell at forward bias. Different possible regions for non-radiative recombination are indicated: a) interface-, b) space charge region-, c) quasi-neutral region- and d) back interface recombination. Adapted from [35]

The preferred back contact consists of sputtered molybdenum, serving as a quasi-ohmic contact with the absorber thanks to the formation of a $MoSe_2$ intermediate layer during absorber growth. The p-type CIGS absorber can be grown by various methods:

co-evaporation, selenization (often followed by sulfurization) of precursors deposited by sputtering, electrodeposition, printing or even by sputtering from compound targets, possibly in a Se ambient. While co-evaporation led to the highest efficiencies for a long time [15,36,37], the largest commercial manufacturer and current world record holder Solar Frontier is using the method of a sputtered precursor with subsequent selenization and sulfurization, and reported a record efficiency of 23.35% [12]. Various CIGS compositions are used, mainly aiming at tuning the material band gap (In-Ga ratio, Se-S ratio), as well as its bulk and surface electronic properties. Among others, the introduction of a band gap grading and the presence of alkali elements are two key features that have fueled the development of higher efficiencies and are addressed in more details in the following sections.

Following the absorber deposition, heterojunction formation is ensured by the deposition of a thin n-type buffer layer. Historically, CdS has been used for best efficiency, but due to its relatively low band gap (2.4 eV) and potential upcoming regulations the search for alternative materials yielding similar junction quality has been given much attention. Most notably, the best alternative buffer so far is CBD grown Zn(S,O,OH), which is used by Solar Frontier for the current record cell. The buffer layer is followed by a resistive layer, often intrinsic zinc oxide, that is sometimes called a second buffer or high resistance window layer. The intrinsic layer helps preventing current leakage in case of local inhomogeneities or incomplete buffer coverage [38, 39] and also possibly to protect the buffer from ion damage during sputtering of the subsequent layers. Transparent conducting oxides (TCO) are applied as the front contact. Research cells and even some commercial module designs support the charge collection with an additional metallic grid. The typical TCO used for CIGS solar cells in research laboratories is aluminum-doped zinc oxide [40]. More recently, record cells tend to use more advanced window combinations, such as atomic layer deposited ZnMgO as intrinsic, and boron-doped zinc oxide as conducting layer. For record efficiency cells and modules an anti-reflecting coating is often applied.

### 1.3.4 Compositional grading and band gap

State-of-the-art CIGS thin film absorbers grown by co-evaporation generally show a varying indium to gallium ratio across their thickness. The relative amount of Ga determines the band gap energy of CIGS, which can range from 1.0 eV for pure $CuInSe_2$ to 1.7 eV for pure $CuGaSe_2$, mainly due to a shift in the position of the conduction band minimum (CBM) [41]. There is a bowing in the band gap function and Equation 1.1 as reported in [14] is used for calculations if needed. Optical absorption band gap energy values of 1.1-1.2 eV, and integrated compositions with a [Ga]/([Ga]+[In]) (GGI) ratio of around 0.3 are used in record efficiency devices.

$$E_g = 1.004(1 - \mathrm{GGI}) + 1.663\ \mathrm{GGI} - 0.033\ \mathrm{GGI}(1 - \mathrm{GGI}) \tag{1.1}$$

A Ga-grading profile was first introduced by Contreras et al. [42], and later extended as a consequence of the introduction of a three-stage deposition process by co-evaporation [43]. This process (see Figure 1.2) , which yields better crystallinity of the absorber layer, is based on the inter-diffusion of the different elements, and naturally results in the formation a double grading profile with a higher Ga contents towards the front and the back interfaces, and lower Ga contents in the central-front region. This can be explained by a more favorable reaction between Cu and In than between Cu and Ga [44] and by different potential barriers for the diffusion of In and Ga through Cu vacancy defects [45]. As a consequence, there is a strong interplay between the amount of excess Cu supplied in the 3-stage process, the final overall amount of Cu, and the shape of Ga-grading profile [46,47]. Szaniawski et al. [48] reported that interpreting the effects of variations in the Cu content is complicated by the resulting variations in the Ga grading, which could explain the scarcity of studies on the effects of the Cu content in Ga-graded CIGS absorbers.

The formation of the Ga grading is also influenced by other factors such as the presence and amount of alkalis during growth [49–51] and the deposition temperature [52]. The Ga grading resulting from a 3-stage process is typically further controlled by adjusting the In and Ga rates during CIGS growth [46, 53]. One of the advantages of a Ga grading in

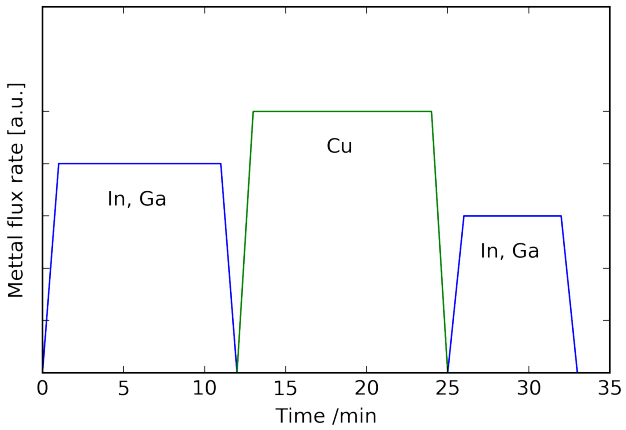


Figure 1.2: Schematic of a simple 3-stage process for the co-evaporation of CIGS. The main characteristic is the separation of Cu and Ga + In evaporation, leading to a re-crystallization phase at the end of the second stage where a Cu excess is reached. The Se pressure is typically constant and a multiple of the other metal fluxes.

CIGS absorbers is the change of chemical potential, resulting in an improved collection of charge carriers, especially for photon energies in the near infrared [54, 55]. Another advantage consists in the presence of a narrow band gap ("notch") region close to the front surface, enhancing the absorption of low-energy photons. Larger Ga content at the front interface of the absorber than in the notch ("front grading") is needed for improved junction quality. A small conduction band offset ($< 0.3$ eV) at the CdS/CIGS junction is reportedly beneficial for the interface quality, although larger values would result in a potential barrier for electrons and lead to increased interface recombination [56–58]. The ideal shape of the front and back gradings was investigated in depth by computer simulations, however without consensus being reached [45, 59, 60]. Experimental results reported in 2011 showed that an overly pronounced front grading can also result in a barrier for electrons, leading to enhanced recombination in the space-charged region [53]. To achieve a smoother front grading, the standard 3-stage process was modified into a multi-stage process, with the addition of several sub-stages in the evaporation rates of In and Ga [53]. Jackson et al. [37] reported on the other hand that an efficiency increase from 20.8% to 21.7% was partially achieved also thanks to a more pronounced front grading. The optimized Ga-grading profiles reported in [36] and [37] are similar in the front region

of the absorber, as shown in Figure 1.3.

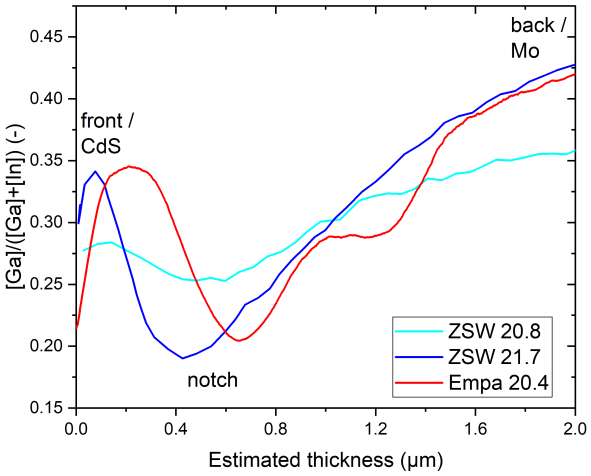


Figure 1.3: Comparison off different [Ga]/([Ga]+[In]) gradings in solar cells from different groups [36, 37]. All cells shown have efficiencies above 20%. The front, back and notch position ar marked for reference.

The technical complexity of a 3-stage process motivates investigations for simpler deposition methods. Salome [61] demonstrated in 2014 that, provided the implementation of a workable Ga-grading, a comparable absorber quality can be achieved on single-stage absorbers. The authors reported a small drop in efficiency from 17% of a 3-stage reference to 16.3% of the single-stage, which they attributed mainly to differences in the front surface grading. Mainz et al. [62] recently showed that recrystallization of the chalcopyrite phase during co-evaporation of CIS films might occur shortly before the segregation of Cu-Se on the surface. High-quality Cu-poor films could therefore be achieved without reaching a Cu-rich phase at all, opening up the possibility of a much simpler and controllable process if the composition and crystal structure during the co-evaporation process is carefully in situ monitored. However, the study was performed on Ga-free absorbers and the eventual effect on the Ga grading is therefore unknown. CIGS layers grown by selenization of precursors have generally Ga accumulation at the back, near the Mo interface but no Ga grading at the front. For the highest efficiency solar cells an additional step of $H_2S$ annealing is used to form a selenium rich CIGSSe layer in order to reach high $V_{OC}$ values [63–65]. $CuInS_2$

and $CuGaS_2$ have a band gap of 1.53 and 2.49 eV respectively, considerably extending the achievable range of band gaps. Contrary to Ga, the sulfur incorporation is mainly acting on the valence band maximum (VBM) [66]. Cells using partial sulfurization reach very high efficiencies, as for example the current efficiency record of Solar Frontier. However full-sulfur CIGS (without any selenium) is still limited and reached 15.5% recently [67].

### 1.3.5 Alkali post deposition treatment of CIGS layers

Addition of alkali elements, especially Na, has long been subject of studies in the chalcopyrite thin film community because of the beneficial impact on the electronic properties of the absorber and solar cells. Similar beneficial effect on the bulk electronic properties were observed when diffused directly from the glass substrate during the absorber deposition at elevated temperature [68], as when adding them in a controlled manner prior, during, or after CIGS growth [69]. The most striking improvements have been observed for Na, mainly based on an increase of doping [70–72]. Multiple explanations for this result exist. The formation of acceptor type defects (e.g. $Na_{In}$), the annihilation of compensating donors (e.g. $In_{Cu}$) [73], the passivation of donor type Se vacancies ($V_{Se}$), mainly at grain boundaries, by sodium induced oxygen chemisorption [74] and potentially the increase in Cu vacancy concentration due to sodium out diffusion during cooling and washing [75]. No final agreement on the dominating mechanism exists.

Whereas Na shows the most beneficial effect as a single alkali element [76], the controlled addition of KF in a post-deposition treatment (PDT) yieldes a significant improvement in efficiency up to a world record efficiency of 20.4% [36]. It was later shown that similar behavior is achieved for the other heavy alkali elements as well, leading to subsequent records with RbF and CsF PDT [15, 77]. Such a PDT treatment was originally found to be the most beneficial method to add Na onto CIGS grown at low-temperature on plastic substrate [71], because it allows separating the influence of Na on CIGS film growth from its beneficial effect on electronic properties. While it was found that Na PDT mainly modifies the bulk electronic properties of the CIGS layer, with no discernible surface modification, addition of KF in a similar PDT treatment leads to a significant alteration of

the CIGS surface composition, namely Cu and Ga depletion. Detailed ATP investigations have shown that Na is present within the grains (~150 ppm) as well as at the grain boundaries (in the range of 0.2 at.%) [78], while for heavy alkali elements little to no concentration is observed inside the grain [79, 80]. Furthermore, a decrease in Na content for samples treated with K or Rb is also systematically observed [15, 17, 36, 81–83], possibly based on an ion exchange mechanism. The modified CIGS surface has strong implications on the interface formation and growth of subsequent layers, especially when grown by chemical bath methods [36, 84], and the resulting thinner buffer layer is an important part of the efficiency improvements. A review of the impact of addition of KF after the growth of CIGS is presented in ref. [85]. Strengthened by several consecutive world records for the CIGS technology when applying a process based on alkali-addition after CIGS growth [37, 77, 86], this findings shed new light on the importance of considering the alkali addition process together with alkali type and their combination and the effects on both bulks as well as surface/interface properties of CIGS and solar cells. Whether the effect of heavy alkali PDT is a direct electronic effect because of the modified surface composition of the CIGS layer or whether it indirectly affects the junction quality by modifying the interface properties during buffer layer deposition is still under discussion. Recent calculations as well as in-depth investigations of treated samples indicate that the presence of an alkali indium selenide phase at the interface is probable [83, 87–89]. Influence on the bulk properties have also to be considered and cannot be excluded from the overall effects on solar cell efficiency. Investigations of the quasi-fermi level splitting in treated absorbers have indicated that the improvements are not only interface related [90].

## 1.4 The solar spectrum and limitations for single junction solar cells

The sun is the source of energy for solar cells operated on earth or on spacecraft in the solar system. While the available photon distribution roughly follows a black body spectrum at about 5800 K, it shows specific features due to absorption and scattering at particles in our atmosphere (Figure 1.4).

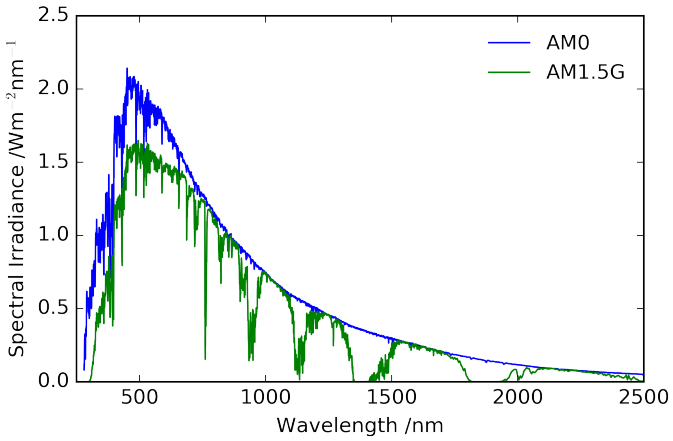


Figure 1.4: Solar spectrum at a position just outside earths atmosphere (AM0) and on earth under a zenith angle of 48.19° (AM1.5), representing an average spectrum as measured in the United States over a period of one year [91].

Not all energy contained in this spectrum will be usable for the generation of energy. In 1961 Shockley and Queisser calculated the detailed balance describing how optical, thermal and electrical losses limit the efficiency of regular single junction solar cells depending on the band gap of the absorber. The maximum power conversion efficiency is approximately 33 % for a band gap around 1.34 eV [92]. Figure 1.5 summarizes the main loss mechanisms. The main sources of loss are thermalization and incomplete absorption.

Any approach to overcome these limitations aims at circumventing one of the base assumption of the SQ model:

- A step like absorption function with no interaction with photons below the onset, and exactly one charge carrier generated for each photon absorbed.
- Direct thermalization of charge carriers to the band gap.
- Thermal equilibrium between cell and environment and isotropic emission without re-absorption.

Different options to circumvent these limits have been proposed, the most common being concentrator and multi-junction solar cells.

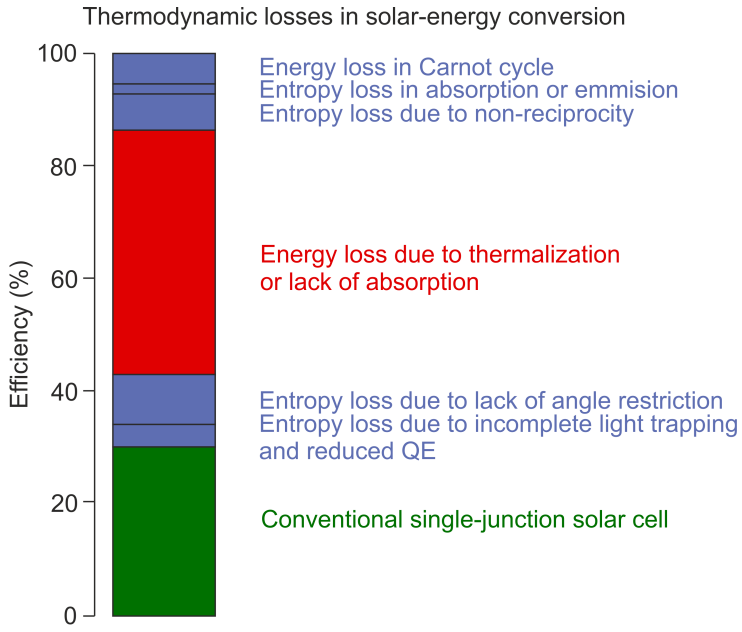


Figure 1.5: Estimation of the different loss mechanisms limiting the efficiency of a single junction solar cell (adapted from [93])

## 1.5 Multijunction solar cells

In order to reduce thermalization losses two or more solar cells with different band gap can be combined to reach higher photovoltaic conversion efficiency [94]. The concept has been investigated for many years and the highest photovoltaic conversion efficiency demonstrated so far, 46.0 %, was reached with a 4-junction cell at a concentration of 508 suns [95]. These kind of devices, tough very efficient, are all based on waver technologies, making the resulting cells very expensive. While they are suitable for applications at high concentrations or when cost is not an issue, more cost effective alternatives are needed for large scale deployment. All thin-film 2-junction (tandem) devices are such an alternative, promising improved efficiency over single junction solar cells at only moderately increased cost.

The cells in a tandem device can be connected independently (4-terminal configuration) or in series (2-terminal configuration) (Figure1.6).

The 2-terminal concept has the advantages of reduced material usage, lower parasitic losses due to the reduced number of TCO's and the use of a single electric circuit. The

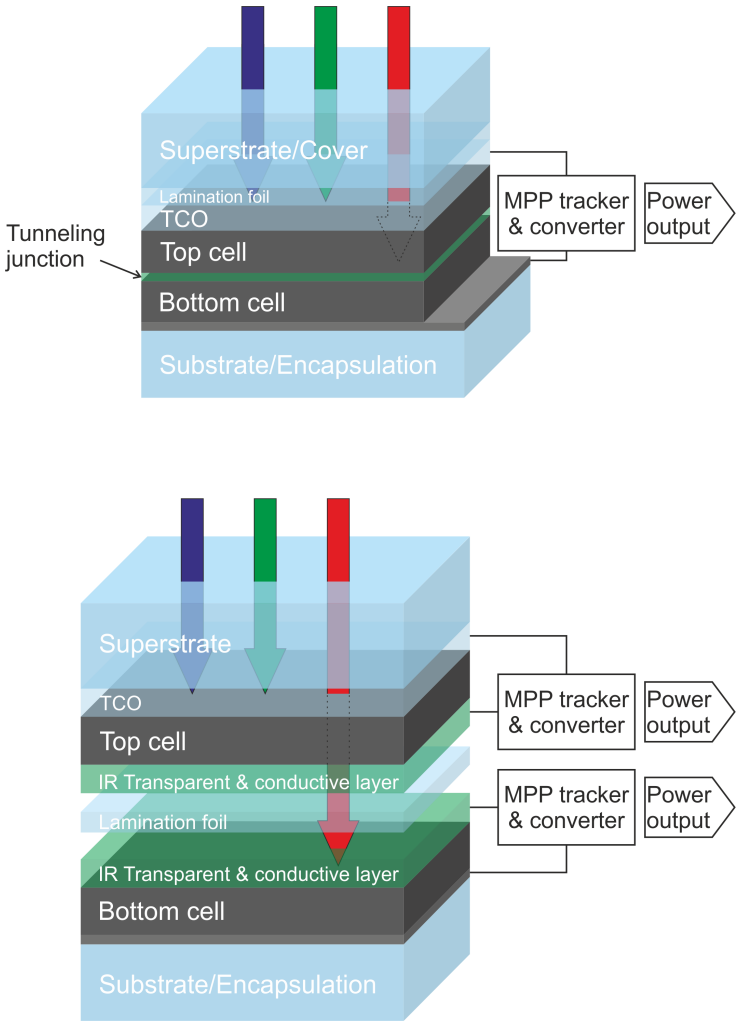


Figure 1.6: Schematic display of a tandem solar cell in 2- and 4- terminal configuration

primary disadvantage is the need of current matching between the sub cells. This can be achieved by choosing the right combination of band gaps, or by artificially reducing the absorption in the top cell (when using a band gap that is narrower than optimal) by limiting the absorber thickness [96]. While this approach has been investigated repeatedly, especially to circumvent the need for higher band gap top-cells in combination with silicon bottom cells, it inherently reduces the open circuit voltage and maximal potential of the device. 2-terminal devices can be realized by monolithic cell interconnection or by string wise interconnection. The first contains the requirement for a stable and efficient tunnel/recombination layer and the need for a bottom cell that is stable to the top cell deposition process. The later looses most of the advantages a 2-terminal devices provides as both cells need to be finished independently and therefore material cost and parasitic absorption is similar to the 4-terminal case. 4-terminal devices allow to manufacture the different cells independently, considerably simplifying the growth process and are inherently less dependent on the incoming spectrum or asymmetric degradation of the sub-cells. However, the increased material use and optical losses speak against them.

Figure 1.7 shows the efficiency limits for tandem devices depending on the sub cell band gaps.

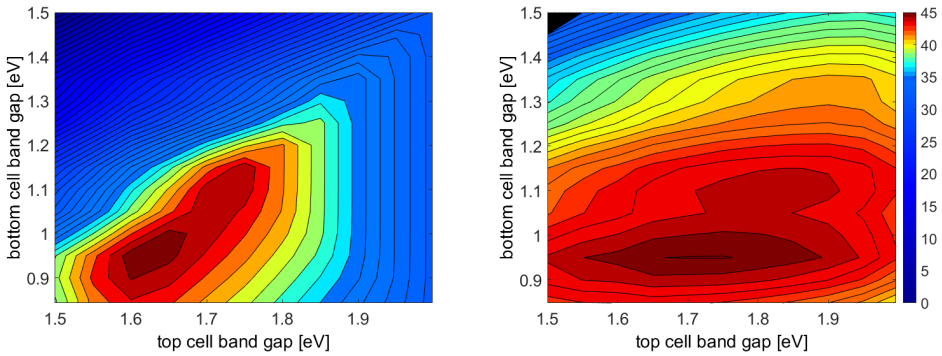


Figure 1.7: Detailed balance efficiencies for a two junction device in dependence of the sub-cell band gaps. (left) The calculation show a relative narrow region of highest efficiency for 2-terminal devices due to the current matching constrains described in the text. In 4-terminal configuration (right), the restrictions on suitable partners is much more relaxed. In both configurations a narrow band gap bottom cell is preferable as it enables high efficiency while allowing a reasonable range of top cells.

One can see that a narrow band gap around 1.0 eV is preferable for the bottom cell in both, 2- and 4-terminal configurations, and almost required to reach the best potential in a 2-Terminal configuration. This becomes even more critical, if optical losses such as parasitic absorption and reflection are taken into account.

The tunability in the band gap of the CIGS materials system from 1.0 eV to 1.7 eV therefore presents an attractive advantage for tandem devices. CIS or CIGS cells with a band gap of close to 1 eV are suitable as a bottom cell in combination with a top cell of band gap $>$ 1.6-1.7 eV. Unfortunately CIGS cells with wide band gap ($>$ 1.3 eV) suffer from poor electric properties and high absorption below the band gap. Therefore, alternative absorbers such as DSSC, CdTe or perovskites have been applied as top cells onto CIGS bottom cells to investigate their feasibility [97–101].

At the beginning of this thesis (2015) the best efficiencies published for monolithic tandems with CIGS were 13.0% for a CIGS/DSSC [100] and 10.9% for a CIGS/Perovskite [99] device, but have since then been hugely improved, up to 22.4 % [102]. For 4-terminal configuration, improvements relative to the sub-cell efficiencies had been shown to prove the validity of the concept (20.5 % tandem with 18.5 % bottom cell) [98, 103, 104] but no efficiencies beyond the single junction record (21.7 % for CIGS and 20.1 % for perovskite at the time) were published.

## 1.6 Perovskite solar cells

The rapid development of perovskite solar cells in the last years have made them one of the most promising options for the top-cell in thin film tandem devices. The name refers to the crystal structure of $CaTiO_3$, a cubic structure with one cation at the corner positions, one at the body center and the 3 anions at the face centered positions. Interesting for solar cells are the compounds with the general formula $ABX_3$ with halogen atoms as the anions (X) and different organic or inorganic cations (A and B). Perovskite solar cells share many of the advantages of CIGS, with good efficiency, direct band gap with high absorption coefficient, low fabrication costs and tunability of the band gap. Using different anions and cations, the band gap range covered by this material system reaches from

approximately 1.17 to 2.24 eV [105–107], and therefore perfectly complements the CIGS as top-cell for tandem devices. While the initial compositions for perovskite solar cells (mainly methyl-ammonium lead iodine $MAPbI_3$) already reached quite good efficiencies, those cells often suffered from hysteresis and low stability [108, 109]. Recent advances with different organic and inorganic cations as well as new charge-selective contacts have strongly reduced these issues [110, 111]. The current record efficiency is 24.2 % for opaque and 18.1 % for semitransparent perovskite solar cells [112, 113]. For further information on this technology the reviews of Petrus and Wang are recommend [114, 115].

## 1.7 Aim of this thesis

The aim of this thesis is the development of high efficiency CIGS solar cells with a band gap of 1.0 eV, for the implementation into tandem devices with perovskite top cells. To do so, it is important to identify the factors that limit efficiencies of narrow band gap CIGS cells and implement measures to circumvent them.

In particular, this thesis takes the following approaches based on the hypotheses given below:

- Investigation of the influence and possibilities of different Ga to In gradings in the absorber layers to process solar cells with the lowest possible optical band gap (1.00 eV, necessary for tandem devices) and achieve the best photovoltaic performance by reducing recombination losses.

  *Hypothesis:* Non-radiative recombination within the absorber and at the interfaces is, at least partly, governed by the concentration of minority charge carriers. A band gap grading may be used to influence the thermal population of charge carriers at a specific point (e.g. interfaces or space-charge-region) in the absorber, allowing to passivate/reduce regions of high recombination.

- Post deposition alkali treatment of CIS absorber layers to improve absorber doping and increase cell efficiency.

*Hypothesis:* Treatment with Na as well as heavy alkali elements has been an important part of the performance increase seen for CIGS in recent years. The effects include an increase in absorber doping and a decrease in recombination. Similar improvements may be observed with proper implementation in narrow band gap CIS based cells.

- Reduction of the defect density in the absorber by increasing the Cu concentration towards stoichiometric compositions to further improve the photovoltaic performance.

  *Hypothesis:* Typical compositions (high CU deficiency) for CIGS solar cells contain a high concentration of intrinsic defects which may be detrimental. Previous work has indicated that stoichiometric cells are limited by recombination at the front interface. Heavy alkali treatment is reported to lead to a modification of said interface, most likely due to the presence of an alkali-indium-selenide phase. This may be able to effectively reduce recombination at this interface, allowing for less Cu deficient absorber compositions.

The final goal is the realization of CIGS/Perovskite tandem devices surpassing the records achieved by the respective sub-cells. This will display the potential of this technology to exceed the single-junction Shockley-Queisser efficiency limit. The results of this work will provide a base for further development of affordable all thin film tandem solar cells with efficiencies well beyond single junction devices.

# 2 Device fabrication and characterization

This chapter describes the methodologies for the fabrication and analysis of absorber layers and solar cells. In the first section, the absorber growth and solar cell fabrication is detailed on the basis of a "baseline" process. The second part describes the concept and equipment for the characterization of specific layers and finished cells.

This chapter is partly based on the following publications:

[1] T. Feurer, P. Reinhard, E. Avancini, B. Bissig, J. Löckinger, P. Fuchs, R. Carron, T. P. Weiss, J. Perrenoud, S. Stutterheim, S. Buecheler, and A. N. Tiwari, *Progress in thin film CIGS photovoltaics - Research and development, manufacturing, and applications*, Progress in Photovoltaics: Research and Applications, Volume 25, 2017, Pages 645-667

[116] Thomas Feurer, Benjamin Bissig, Thomas Paul Weiss, Romain Carron, Enrico Avancini, Johannes Löckinger, Stephan Buecheler, Ayodhya N. Tiwari, *Single-graded CIGS with narrow bandgap for tandem solar cells*, Science and Technology of Advanced Materials, Volume 19, No.1, 2018, Pages 263-270

[117] Thomas Feurer, Fan Fu, Thomas Paul Weiss, Enrico Avancini, Johannes Löckinger, Stephan Buecheler, Ayodhya N. Tiwari, *RbF post deposition treatment for narrow bandgap Cu(In,Ga)$Se_2$ solar cells*, Thin Solid Films, Volume 670, 2019, Pages 34-40

## 2.1 Device fabrication

### 2.1.1 Substrate

For all solar cells in this work, the substrate of choice is soda lime glass (ThermoFischer object slide grade) of 1mm thickness. The approximate composition of this type is given in Table 2.1.

To produce the necessary back electrical contact, a triple layer of molybdenum is sputtered onto the substrate by pulsed direct current sputtering. The total thickness of the Mo back contact is approximately 0.5 $\mu$m.

### 2.1.2 Absorber growth

CIGS absorber layers are deposited by multistage co-evaporation from pure metal sources in an Octoplus type vacuum chamber from MBE-Komponenten GmbH (Figure 2.1).

The Source materials were supplied by Alfa Aesar with following purities: Cu, In and Ga 99.9999 %, Se 99.999 %, NaF 99.99 %, RbF 99.975 %. Evaporation rates are controlled by the source temperature and calibrated by reference runs for all sources except Se, which is valved and equipped with an optical absorption spectroscopy flux monitor.

During the first stage, substrate temperature is approximately 390 °C, followed by second and third stage with a maximal substrate temperature of 500 °C. For regular absorbers, Ga is supplied at all stages with different rates, while In is only added in the first and third stage. For the back-graded samples, Ga is only added with a steep downwards ramp

Table 2.1: Approximate composition of the substrate SLG

| | | |
|---|---|---|
| Silicon Dioxide | $SiO_2$ | 72.2 % |
| Sodium Oxide | $Na_2O$ | 14.3 % |
| Calcium Oxide | CaO | 6.4 % |
| Magnesium Oxide | MgO | 4.3 % |
| Potassium Oxide | $K_2O$ | 1.2 % |
| Aluminum Oxide | $Al_2O_3$ | 1.2 % |
| Sulfur Trioxide | $SO_3$ | 0.3 % |

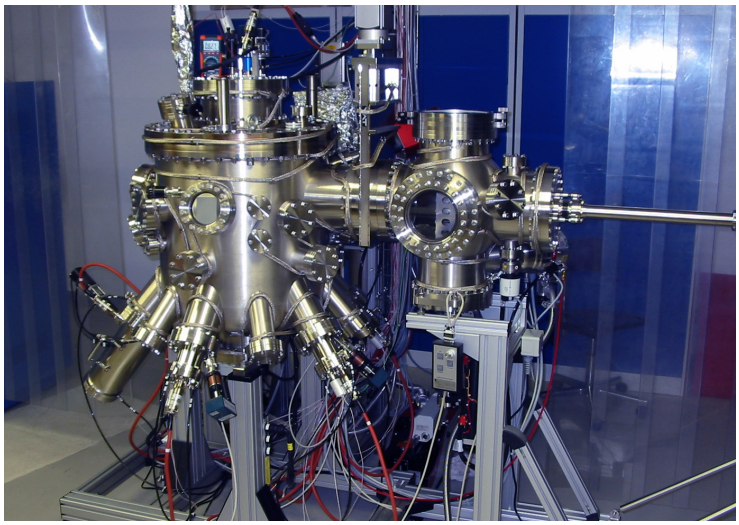

Figure 2.1: Deposition chamber with load-lock on the right and main chamber to the left. A potential total of 9 sources can be connected to the bottom part while the substrate is mounted face down on a rotated and heated holder on the top. Each deposition run produces 4 samples of 5x5 $cm^2$ for further processing.

within the first 6 minutes of the first stage, followed by a normal CIS process. The final Cu concentration within the sample is controlled by the amount of Cu excess deposited in the second stage. Deposition is finished by evaporation of a short In capping layer at a substrate temperature of 380 °C, immediately followed by in-situ post deposition treatment (PDT) without any break of vacuum. The absorbers are treated with NaF at a substrate temperature of 380 °C, followed by post annealing or RbF PDT at different substrate temperatures (see Chapter 4) of 20 minutes each under a reduced Se flow. A detailed schematic of the metal fluxes and temperatures during growth can be found in Figure 2.2.

### 2.1.3 Buffer layer

All absorbers in this work are based upon a p-n hetero-junction with a n-type CdS buffer layer ($E_g$ ~2.4 eV). The CdS is deposited by chemical bath deposition from aqueous solutions of ammonium hydroxide (2 M), thiourea (22 mM) and cadmium acetate (2.1 mM) at ~ 70 °C as described in [118]. Thickness of the layer is approximately 60 nm for cells with NaF PDT and ~ 35 nm for samples with additional RbF PDT (see [83]).

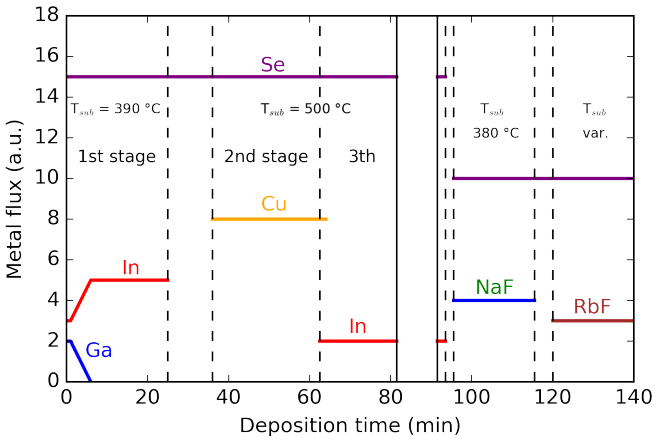


Figure 2.2: Exemplary deposition profile for the growth of narrow gap CIGS with NaF and RbF post deposition treatments.

### 2.1.4 Front electrical contact

Window layers consisting of a high restive "second buffer" of non-intentionally doped zinc oxide (~ 70 nm) and a TCO contact layer are deposited by radio frequency magnetron sputtering. For most cells in this work aluminum doped zinc oxide ($ZnO:Al_2O_3$, 98:2 wt%) was deposited as TCO (~ 200 nm), although some samples in Chapter 5 use indium zinc oxide ($In_2O_3$:ZnO, 89.3:10.7 wt%) (~ 110 nm).

Ni/Al grids and $MgF_2$ anti reflection coatings are deposited by electron beam evaporation. The cell size is defined by mechanical scribing and is approximately 0.57 $cm^2$. The actual cell size is characterized with a flat bed scanner.

## 2.2 Compositional and structural measurements

### 2.2.1 X-ray fluorescence (XRF)

Matrix element composition and absorber thickness is measured with an in-house build XRF setup. It uses a 45 keV X-ray source (Oxford Instruments, XTF-5011) and a Si-PIN detector (Amptek, XR-100CR). XRF measurements deliver spectra with specific peaks

for each element as shown in Figure 2.3. For quantification, the K$\alpha$ emission lines of the constituent elements are fitted with the software PyMca and then correlated to a reference sample with known composition from ICP-MS measurements. As there can be re-absorption of the emitted radiation it is important to use a reference with similar thickness and grading.

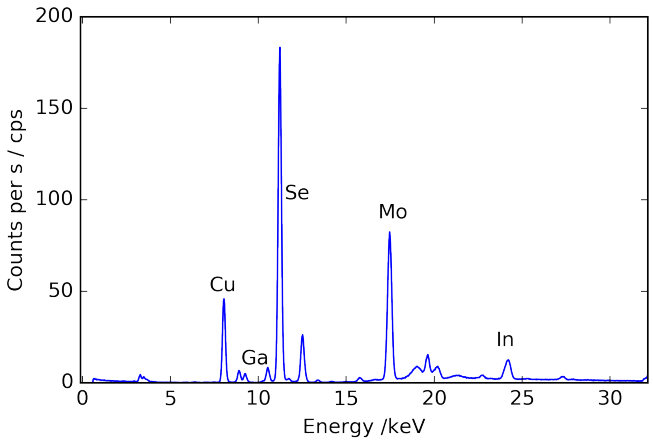


Figure 2.3: XRF spectrum with the K$\alpha$ peaks of Cu, In, Ga, Se and Mo labeled.

With this method, the repeatability error for compositional ratios (CGI, GGI) is below 3.0 % ($2\sigma$), based on a large number of measurements of given samples.

### 2.2.2 Secondary ion mass spectrometry (SIMS)

Identification of the depth dependent composition of the absorber was realized by time of flight secondary ion mass spectrometry (TOF-SIMS) on a tool from ION-TOF. A primary measurement beam of $Bi^+$ with 25 keV acceleration and a total current of 1 pA was used on a raster size of 100x100 $\mu m^2$. To achieve sufficient measurement speed the sputtering trough the sample was facilitated by a 2 keV, 400 nA $O_2^+$ sputtering beam on a sample area of 300x300 $\mu m^2$. The different matrix element rates were calibrated by the integral composition as determined by XRF.

### 2.2.3 Inductively coupled plasma spectrometry (ICP-MS/ICP-OES

ICP mass spectrometry (ICP-MS) and ICP optical emission spectrometry (ICP-OES) are used on reference samples to calibrate the XRF measurements. To do so, approximately 1 $cm^2$ of absorber is scratched off the Mo back contact into a 50 mL trace-metal free polyethylene flask. It is then dissolved in 4.5 mL $H_2O_2$ (30 %, Merck Suprapur) and 5 mL of $HNO_3$ (65%, Merck Suprapur) for about 10 min. The samples are further diluted with deionized water to reach suitable concentrations for analysis. Cu, Ga and In matrix element determinations are performed by ICP-OES, and trace metals are quantified using an Agilent 8800 triple quadrupole ICP-MS in He and $O_2$ mode. For all samples, certified standard reference materials are used for calibration and for spikes.

### 2.2.4 Scanning electron microscopy (SEM)

Absorber morphology and the thickness of some of the constituent layers of the solar cells were determined by scanning electron microscopy (SEM). A Hitachi S-4800 electron microscope with acceleration voltages between 5 to 20 keV was used. The samples were cleaved shortly before measurement and coated with approximately 1 nm of Pt if needed to prevent charging.

## 2.3 Device characterization

### 2.3.1 Current-Voltage measurements (I-V)

Basic photovoltaic parameters of the solar cells were identified using current-voltage measurements using a Keithley 2400 source-meter in 4-terminal mode. Illumination was provided by a LOT ABA class solar simulator with a Xe arc lamp. Irradiation intensity was adjusted to a power density of 1000 $Wm^{-2}$ using a certified Si reference cell. Based on the spectral mismatch between the lamp and solar spectrum and on the difference in EQE

between the reference cell and the low band gap solar cells, this calibration method generally underestimates the current of a CIS cell. As the necessary tools to monitor the lamp spectrum were not available, this so named "mismatch factor" can not reliably be calculated in house, and was not used in this work outside the certified cells. As a example, for the 18 % cell in Chapter 4 Fraunhofer ISE certified a current density 0.5 mAcm$^{-2}$ higher than measured in-house (See Appendix C). A solar cell temperature of 25 °C is ensured by a Peltier- and water-cooled stage. To calculate the current density (J), the solar cell area is measured by a high resolution scan (4800 dpi) of the finished cells. This area includes the front contact (grid) but not the back contact (Mo), therefore all efficiencies given in this work are considered designated illumination area efficiency (da).

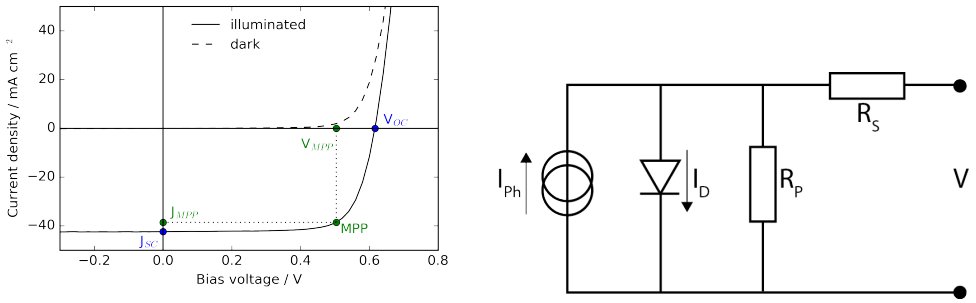


Figure 2.4: (left) Example of a current density-voltage plot in the dark and illuminated. The open circuit voltage ($V_{OC}$), short circuit current($J_{SC}$) and the maximum power point (MPP) are marked. (right) Schematic of a single diode model describing a solar cell in the illuminated state.

From the J-V curve (see example in Figure 2.4, left), important parameters can be extracted, prominently: open circuit voltage ($V_{OC}$) and short circuit current ($J_{SC}$). As the power generated by the device is the product of current and voltage $P = V \times J$, the maximum power point MPP (with current at MPP ($J_{MPP}$) and voltage at MPP ($V_{MPP}$)) can be defined. This allows to define the cell efficiency $\eta$:

$$\eta = \frac{P_{MPP}}{P_{Illumination}} \tag{2.1}$$

With $P_{Illumination}$ under standard illumination (AM1.5G) defined as 1000 Wm$^{-2}$. Another derived metric is the fill factor ($FF = \frac{J_{MPP}V_{MPP}}{J_{SC}V_{OC}}$), a measurement for the squareness

of the curve and therefore of the utilization of the maximal potential spanned from the $V_{OC}$ and the $J_{SC}$.

For further analysis, the J-V characteristics of a well-behaved solar cell can be represented by a relatively small number of parameters of the solution of a one diode equivalent circuit with two resistors (Figure 2.4, right). The representing diode equation can be written as:

$$J = J_0\left[exp\left(\frac{q(V - JR_S)}{Ak_BT}\right) - 1\right] + \frac{V - JR_S}{R_P} - J_{Ph}(V) \tag{2.2}$$

where $q$ is the unit charge, $k_B$ the Boltzmann constant and $T$ the temperature. $J_0$ is the diode saturation current density and $A$ the diode quality factor. $R_S$ and $R_P$ are parasitic resistances called series and parallel resistance. $R_P$ can be estimated by fitting the J-V curve in reverse bias close to 0 V while $R_S$ limits the slope of the curve in sufficient forward bias above the $V_{OC}$. While the photo current $J_{Ph}$ is influenced by the collection of photo generated carriers and therefore voltage dependent, for a simple analysis it is often assumed constant and almost corresponds to the $J_{SC}$.

### 2.3.2 I-V characterization in tandem configuration

I-V measurements of 2-terminal tandem devices do not differ from the respective single junction measurement. However for 4-terminal devices an adjustment of procedure is necessary. For the work here, the top cells have been measured as described above, independently from the bottom cell. While this deprives the top cell from potential reflection at the bottom cell, this method allows the use of top-cells in substrate and superstate configuration and likely better represents the situation in a laminated device (where reflection will be greatly reduced).

The bottom cell in 4-terminal configuration is measured with a shadow mask placed on top, to allow for top-cells with reduced area and to facilitate contacting with needles. The top-cell is then placed onto the mask (including grid) and a J-V scan is carried out as before (using the mask area). The photo current is reduced by the top cell shading and

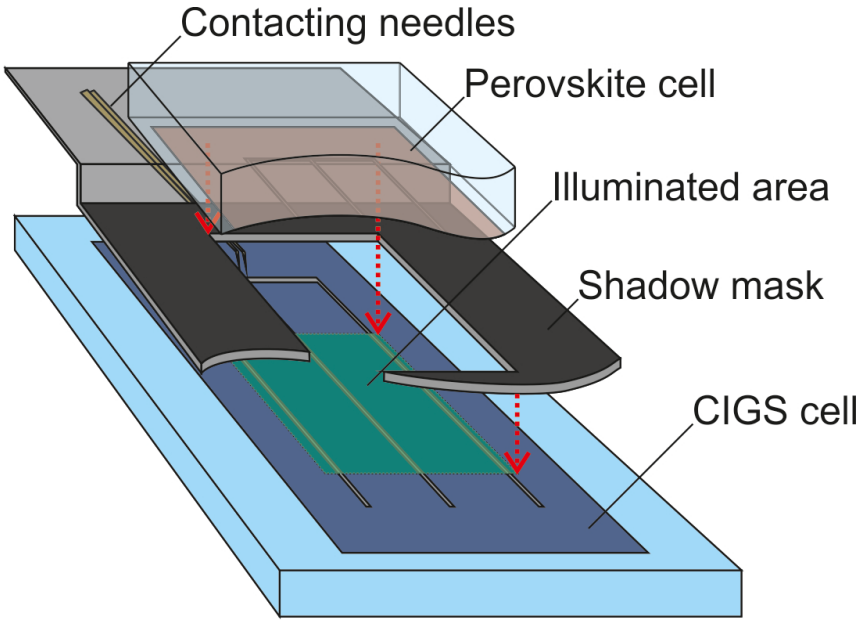


Figure 2.5: Configuration of both cells and the shadow mask in order to measure the bottom cell response in 4-terminal tandem device structure

by the mask, and the dark saturation current remains unchanged.In this configuration the loss in $V_{OC}$ is again higher than in a full laminated device and should give a safe estimate for the 4-terminal tandem potential of the complete device.

Perovskite top cells are provided by other members of the group and semitransparent top cells of good quality could not always be provided. To estimate the tandem performance without a perovskite available, the transmittance of a good top cell was characterized by UV-VIS spectroscopy. The expected $J_{SC}$ in the bottom cell was then estimated by integrating the external quantum efficiency of the bottom cell multiplied by the transmission of the top cell and the solar spectrum. Illumination of the bottom cell was then adjusted on the J-V setup, using a combination of long-pass and neutral density filters to obtain this current. The results measured with this method is in very good agreement with the direct measurements with the actual top cell.

### 2.3.3 External quantum efficiency (EQE)

The external quantum efficiency (EQE) of solar cells is measured on a custom setup designed at Empa. A monochromatic light beam is obtained using a LOT MSH300 monochromator from a halogen lamp source chopped with a mechanical wheel. Constant halogen light bias of around 0.2 sun intensity was applied to the cell during measurement. The EQE response was measured using a Stanford Research SR830 DSP lock-in amplifier and calibrated against certified Si and Ge cells.

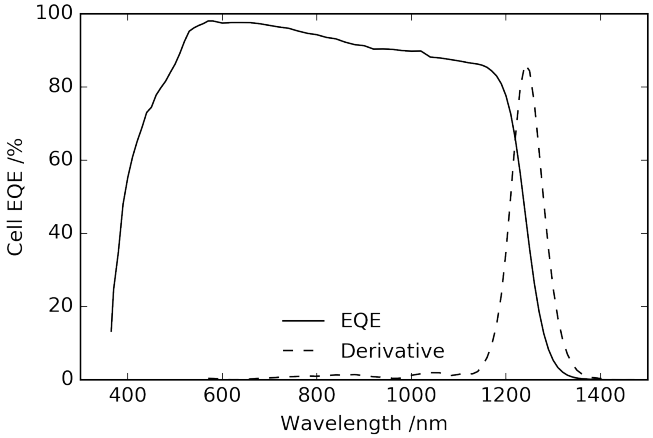


Figure 2.6: The EQE of a typical CIS solar cell. The band gap $E_g$ of the absorber layer is determined by the inflection point (peak in the derivative) in the near infrared decay of the curve.

The EQE curve (Figure 2.6) describes the ratio of extracted charge carriers to incoming photons in dependence of the illumination wavelength. As such, it not only represents the ability of the absorber to capture the light but also gives information on the parasitic absorption in the buffer and window layers, the collection of charge carriers in the absorbers as well as losses due to reflection at the front interface. The inflection point in the near infra-red decay of the curve ($\frac{d^2(EQE)}{d\lambda^2} = 0$) gives a good measure for the absorber band gap for samples with good collection and little interference in the layer [119].

By integrating the product of EQE and the solar photon flux density over all relevant wavelengths, the solar cell current at measurement voltage can be calculated (typically short circuit conditions) (equation 2.3).

$$J_{PH}|_{V=0} = J_{SC} = \int_0^\infty \Phi_{AM1.5G}(\lambda) \cdot EQE(\lambda) \mathrm{d}\lambda \tag{2.3}$$

The grid shading during EQE (measurement spot ~0.1 $cm^2$) and J-V (cell area ~0.57 $cm^2$) measurement is different, leading to a certain mismatch between this value and the $J_{SC}$ from J-V. The mismatch due to the illumination spectrum of the solar simulator has already been discussed above and is generally well reproducible. Larger differences between EQE and J-V currents may indicate a barrier for the photo current in the device.

### 2.3.4 Temperature and illumination dependent I-V (T-IV)

A temperature controlled stage placed in a cryostat implementing liquid nitrogen cooling and resistive heating allows the measurement of IV curves at different temperatures. Measurements are done in 4-terminal sensing, using a Keithley 2400 source meter. The illumination for those measurements is provided by a halogen light source equipped with a neutral density filter wheel. These measurements allow to collect information about potential barriers within the solar cells, as well as a determination of the diode saturation current density $J_0$, the temperature dependence of the diode ideality factor $A$ and the activation energy of the primary recombination pathway $E_A$ [120].

### 2.3.5 Admittance spectroscopy (AS)

Admittance measurements in capacitance vs. frequency (Cf) and capacitance vs. voltage (CV) mode are carried out on the same temperature controlled stage as the T-IV measurements, using an Agilent E4980A LCR meter with 4-terminal sensing. Test signal oscillation level is 30 mV. Before measurement all cells are relaxed at 50 °C in the dark for 1 hour. For some capacitance steps in the Cf measurements an activation energy is extracted by the method described by Walter [121]. For CV measurements, the frequency is chosen in a region of flat capacity-frequency behavior over all temperatures investigated, unless otherwise notified at 1kHz. The voltage sweep typically covers the range from -1.5 V to 0.5 V. From this data the apparent doping is extracted using the Mott-Schottky

representation [122].

### 2.3.6 Time resolved photoluminescence (TRPL)

Time resolved photoluminescence (TRPL) measurements are aquired with a Fluo Time 300 from PicoQuant, using a 639 nm diode laser with pulse duration of ~100 ps as excitation source. An Hamamatsu H10330A-45 InGaAs photomultiplier is used in combination with time correlated single photon counting electronics for signal acquisition. Pulse repetition rate is approximately 1 MHz and the spot size in the 50 $\mu$m range as determined with a beam profiler. The typical photon density per pulse is around 7*$10^{11}$ $cm^{-2}$ as estimated from total laser power measurements. The front of the absorber is typically passivated with a thin layer of CdS, unless otherwise specified. As discussed in Chapter 3 and [123], the effective lifetime is fitted after 20 ns to circumvent issues resulting from charge separation and injection intensity. The effective lifetime is a result of the different recombination processes within the cell as given in equation 2.4 and therefore gives a lower limit for Shockley-Reed-Hall lifetime in the absorber in absence of trapping. Additional information on surface recombination as well as charge carrier mobility can be extracted using more elaborate experiments [124].

$$\frac{1}{\tau_{eff}} = \frac{1}{\tau_{rad}} + \frac{1}{\tau_{SRH}} + \frac{1}{\tau_{surf}} \tag{2.4}$$

For some experiments in Chapter 3 the absorber is delaminated from the back contact. To do so, a slide of 1 mm SLG is glued on top of the absorber after a thin CdS deposition (5 min, regular CBD conditions) using DP100 epoxy. Polyimide spacers of 32 $\mu$m thickness are used to achieve a homogeneous glue layer. The glued spot has a diameter of approximately 1 cm. The epoxy is hardened for 24 h at room temperature and an additional hour at 60 °C. After hardening, the absorber is delaminated using a swift kinking motion.

### 2.3.7 UV-Vis Spectroscopy

Reflectance and transmittance measurements have been carried out on a Shimadzu UV-3600 UV-Vis spectrometer equipped with an integrating sphere. Calibration is done using a Spectralon (SRS-99-010, AS-01160-060) and a silver mirror reference, and the measurement curves are corrected for the instrumental response. If necessary, the absorbtance has been calculated from these data using equation 2.5.

$$A = 1 - R - T \tag{2.5}$$

# 3 Compositional grading in CIGS

As discussed in Chapter 1, the band gap of the bottom cell is an important parameter for tandem devices, especially for 2-terminal, but also in 4-terminal configuration. In CIGS the band gap is given by the elemental composition of the absorber. The spectral response as well as the performance of the resulting solar cells can be changed substantially by adjusting this composition throughout the absorber.
In this section the possible ways to modify the group III element grading are investigated. Different front-, back- and double gradings are produced to judge their suitability for solar cells with the narrowest possible optical band gap for CIGS absorbers (1.00 eV). The most promising approach based on the electrical cell performance is identified and further investigated to improve the efficiency of the resulting solar cells.

This chapter is partly based on the following publication:

[116] Thomas Feurer, Benjamin Bissig, Thomas Paul Weiss, Romain Carron, Enrico Avancini, Johannes Löckinger, Stephan Buecheler, Ayodhya N. Tiwari, *Single-graded CIGS with narrow bandgap for tandem solar cells*, Science and Technology of Advanced Materials , Volume 19, No.1, 2018, Pages 263-270

*TOF-SIMS measurements are provided by Dr. Enrico Avancini, optical simulations by Dr. Romain Carron. TRPL measurements were carried out in collaboration with Dr. Benjamin Bissig.*

## 3.1 CIS based solar cells

A comparison of photovoltaic parameters of record efficiency devices (Table 3.1) highlights that a large discrepancy exists between theoretically achievable and practically achieved values for CIS, especially in the $V_{OC}$. By comparison, the CIGS record solar cell is considerably closer to the theoretical maximum. As already mentioned in Chapter 1, this difference is attributed to the double-grading structure in the CIGS, which is not present in these CIS devices. There is a large body of simulations regarding the effectiveness of each part of the grading, and the outcome varies largely depending on the choice of parameters. While there is agreement that the graded structure improves efficiency by reducing recombination, the respective effectiveness of front- and back-grading varies [45, 59, 125–128].

Table 3.1: Comparison of first level solar cell parameters for previous world record (WR) CIS and CIGS solar cells [15,30,129] with theoretically calculated values (SQ) [130], derived from detailed balance calculations for AM1.5G irradiation [92]. Band gaps for the record solar cells are estimated based on the published EQE data. The values in brackets represent the percentage of the theoretical limits

| | Eg | $V_{OC}$ (mV) | $J_{SC}$ ($mAcm^{-2}$) | FF (%) | Efficiency (%) | $V_{OC}$-deficit (mV) |
|---|---|---|---|---|---|---|
| CIS WR [2005] | ~1.00 | 491 (66 %) | 40.6 (84 %) | 75.2 (88 %) | 15.0 (49 %) | ~510 |
| CIS SQ | 1.00 | 749 | 48.2 | 85.4 | 30.8 | |
| CIGS WR [2016] | ~1.14 | 741 (84 %) | 37.8 (88 %) | 80.6 (93 %) | 22.6 (69 %) | ~400 |
| CIGS SQ | 1.14 | 879 | 42.9 | 87.1 | 32.8 | |

In this section, the influence of three different grading approaches are investigated:

- Double grading with reduced band gap.

  Reducing the band gap of double graded cells from approximately 1.15 eV to 1.00 eV

- Front grading with CIS bulk.

  Reducing recombination at the front interface and in the space charge region by increasing the band gap locally.

- Back grading with CIS bulk.

  Reducing recombination at the back contact and improving collection by gradually increasing the band gap towards the back of the absorber.

## 3.2 1.0 eV solar cells with double-grading

As previously described, CIGS solar cells typically employ a so-called double grading, in which the band gap is increased at the front and the back of the absorber (see the reference DG1 in Figure 3.1). In Chapter 1 it was shown that a bottom-cell band gap of 1.0 eV is preferred for tandem application. The most direct approach to reduce the optical band gap of the absorber is keeping the grading structure in place and reduce the Ga content in the notch area as much as possible (Figure 3.1). To do so, the amount of Ga within the deposition process was reduced. First, any Ga deposited during the second stage was removed (DG2) and the Ga rates were halved subsequently (DG3). Samples with no Ga in the third stage (SG) and without any Ga (CIS) were added for comparison.

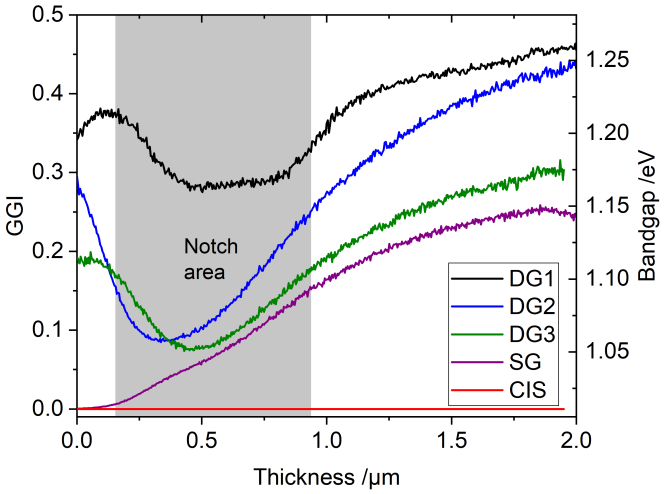


Figure 3.1: SIMS depth profile of the GGI in double-graded cells grown with different levels of total Ga amount. Absorption is dominated by the band gap in the region of minimal Ga content, called notch area in double graded absorbers.

The final GGI profile is a result of the Ga rates during growth and Ga diffusion, which

is significantly influenced by substrate temperature and alkali content [52, 131]. Using a substrate temperature of only 500 °C and with sodium present during the growth, both promoting steeper gradings, the Ga concentration in the notch still remains close to 10 %.

As the notch band gap is responsible for the optical absorption onset, the NIR response of these cells is improved (Figure 3.2). While the better long wavelength EQE leads to an improved current density the $V_{OC}$ deficit, defined as

$$V_{OC} \text{ deficit} = \text{band gap} - V_{OC} \tag{3.1}$$

is increased considerably for the cells with lower band gap (see Figure 3.2).

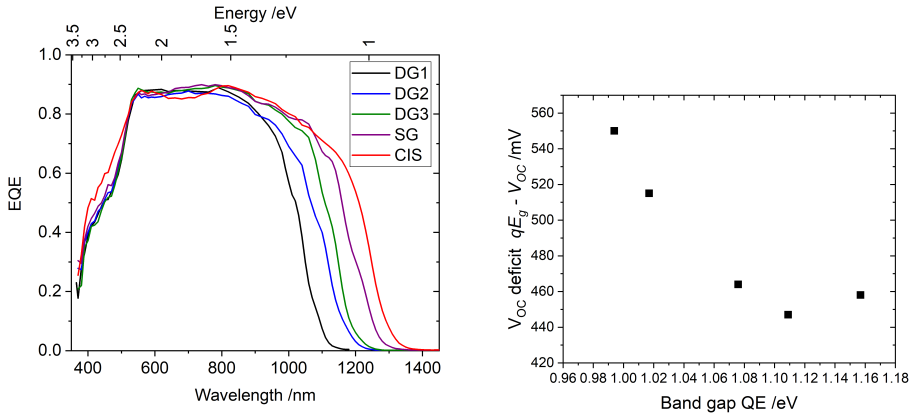


Figure 3.2: (left) Quantum efficiency curves for cells with different Ga grading profiles. The onset in the NIR, representing the band gap, is governed by the Ga content in the notch region of the absorber (see Figure 3.1) (right) The $V_{OC}$-deficit for the different cells in dependence of the QE band gap.

Table 3.2: Parameters of solar cells with double grading structure and different amounts of Ga in the notch, leading to a change in band gap.

| | Band gap (EQE) (eV) | $V_{OC}$ (mV) | $J_{SC}$ (mAcm$^{-2}$) | FF (%) | Eff (%) |
|---|---|---|---|---|---|
| DG1 | 1.16 | 699 | 31.6 | 75.0 | 16.6 |
| DG2 | 1.11 | 662 | 33.2 | 76.0 | 16.8 |
| DG3 | 1.08 | 612 | 34.0 | 75.3 | 15.6 |
| SG | 1.02 | 502 | 35.8 | 66.5 | 12.0 |
| CIS | 0.99 | 444 | 37.0 | 67.2 | 11.0 |

The resulting solar cells parameters (Table 3.2) show the positive effect of the double grading. A different approach is still necessary, as all double-graded samples here have a band gap clearly above the targeted 1.00 eV.

## 3.3 Front-graded CIS solar cells

To reach the goal of a solar cell with a band gap of 1.00 eV and high efficiency, the different parts of the grading are investigated separately. Recombination at the front interface and in the space charge region is reported to be dominating in CIGS and CIS at $V_{OC}$ [132]. By increasing the band gap, the intrinsic carrier concentration can be decreased, and recombination at this point can be reduced. Simulations show significant improvements with a single front grading [126, 133].

Cells with a localized front band gap grading with different steepness (Figure 3.3) are grown by adding Ga only in the 3th stage of the growth process.

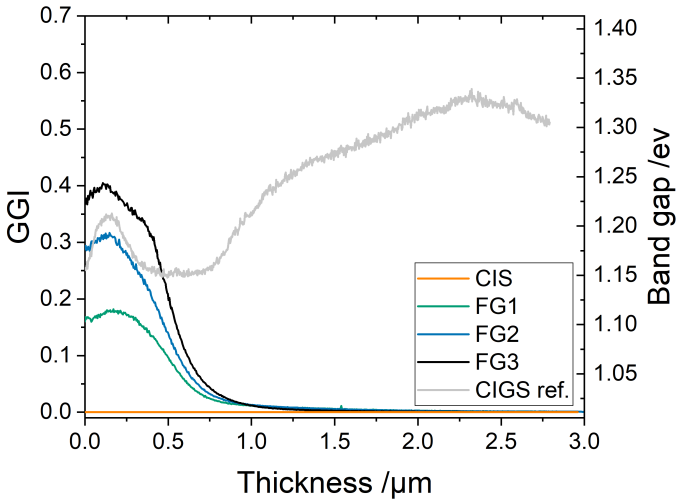


Figure 3.3: TOF-SIMS measured [Ga]/([Ga]+[In]) (GGI) profile and the corresponding band gap through the absorber. For comparison the GGI profile of a double graded CIGS sample is also included.

The evaporation rates for Ga have been increased for 19 minutes in a linear ramp starting after Cu stoichiometry up to the completion of absorber deposition for all samples. The

steepness of the ramp as well as the total amount of Ga increases from FG1 to FG3. The resulting grading shows a preferential diffusion towards the front interface as described in literature [134]. Therefore a pronounced grading is present even in the sample with the smallest amount of Ga added (FG1). The increase in band gap in the front of the absorber is similar to the relative increase (notch to front) in a high efficiency double-graded CIGS for FG1, while FG2 and FG3 show larger increases. The interface band gap has been tuned to be comparable (FG2), lower (FG1) and higher (FG2) than a regular high efficiency CIGS. For all samples the position of minimal band gap is shifted considerably deeper into the absorber compared to the notch position in a double-graded sample.

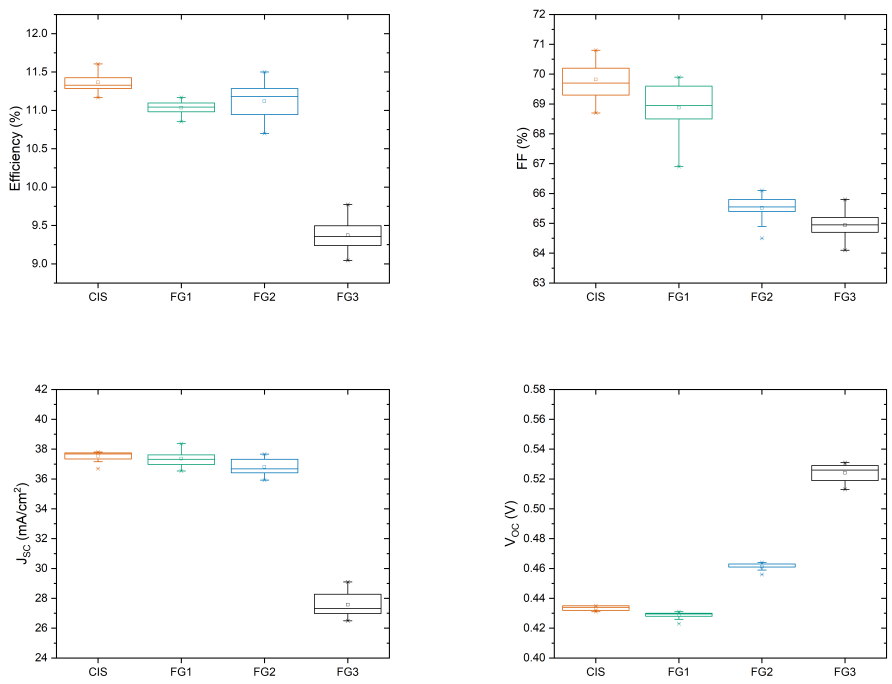


Figure 3.4: J-V performance of CIS solar cells with different GGI front gradings.

The photovoltaic parameters (Figure 3.4) show that the $V_{OC}$ indeed increases with higher front grading, although only for the comparatively strong gradings FG2 and FG3. At the same time, the front grading leads to a strong decrease in FF and $J_{SC}$, especially in the case of FG3.

The EQE curves of the devices change considerably with the implementation of the

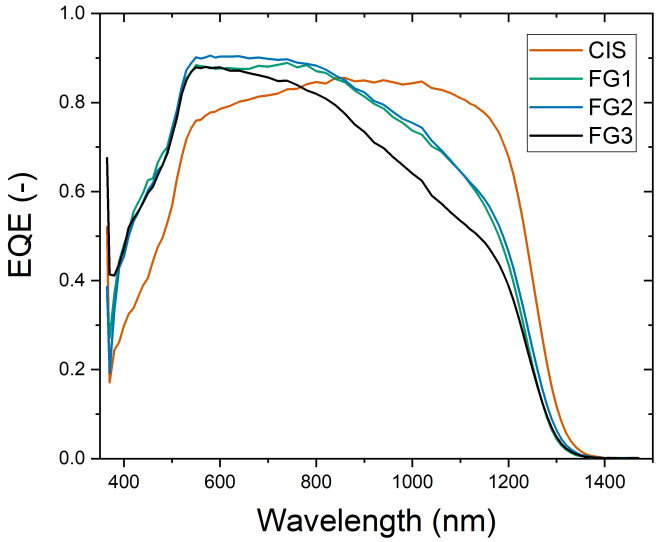


Figure 3.5: Quantum efficiency curves of CIS based solar cells with different front Ga gradings towards the buffer interface.

front grading (Figure 3.5). The general change in shape is probably related to the doping of the CIS absorber being insufficient. The resulting extended SCR leads to recombination of holes generated close to the front interface and therefore reduced EQE at short wavelengths (see section "Sodium in CIS solar cells" in Chapter 4). For the front graded cells, substantially reduced collection of charge carriers generated deeper in the absorber (NIR) is seen, especially for sample FG3.

The absence of improvement with front grading alone indicates that the solar cells presented here are not limited by recombination in the front. Therefore the effect of a back grading is investigated as described in the following.

## 3.4 Back-graded CIS solar cells

The implementation of a back grading is aimed at the suppression of recombination at the back contact and to aid the collection of minority carriers generated outside of the space charge region. Solar cells with a wide front region of Ga free CIS and different band gap gradings with Ga towards the Mo back contact were prepared by a modified three stage

co-evaporation process.

The grading profile achieved in a 3-stage process strongly differs from the evaporation profile for the different components due to re-crystallization and diffusion. As a result, a simple Ga ramp in the process will lead to a stretched grading reaching well into the front of the absorber as shown by sample SG in Figure 3.1. To reach an appropriate grading with sufficient Ga free front, strong Ga ramping is introduced in the first 6 minutes of process (Figure 2.2). The different compositional gradings produced here are named BG1, BG2 and BG3 in the order of increasing Ga content. The depth dependent composition profiles of such layers are shown in Figure 3.6. For all cells (except the double-graded reference) the integrated GGI is below 0.1 as determined by X-ray fluorescence (XRF).

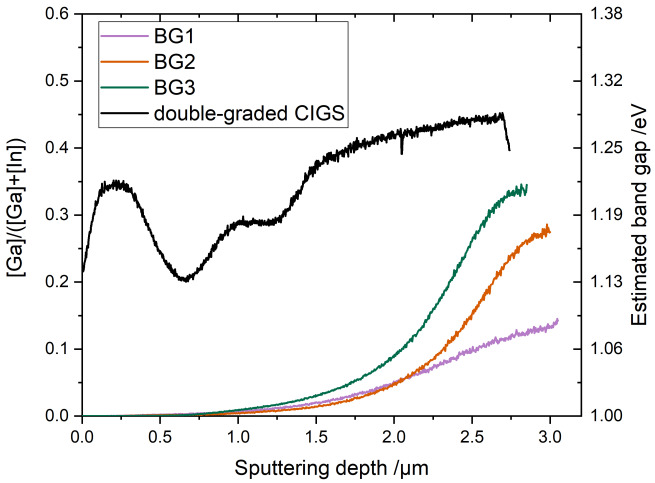


Figure 3.6: [Ga]/([Ga]+[In]) profile measured by TOF-SIMS and the corresponding band gap through the absorber. For comparison the GGI profile for a high efficiency double graded CIGS sample is also included, while more details on this sample can be found in [36].

All BG samples have Ga content towards the back that is lower than a regular multi stage CIGS cell (Figure 3.6, reference taken from [36]). The band gap increase between the point of lowest corresponding band gap and the back interface is smaller (BG1), equal (BG2) or larger (BG3) compared to the reference CIGS. The microstructure of the absorbers, as observed in SEM micrographs shown in Figure 3.7, changes from large-grained for pure

CIS to considerably smaller grains in the case of the strongly graded absorbers. The thickness of the different absorber layers has been extracted from the SEM micrographs as 2.9 $\mu m$ (CIS), 3.1 $\mu m$ (BG1), 3.0 $\mu m$ (BG2) and 2.9 $\mu m$ (BG3) with a roughness of around 0.3 $\mu m$ over multiple grains for all absorbers.

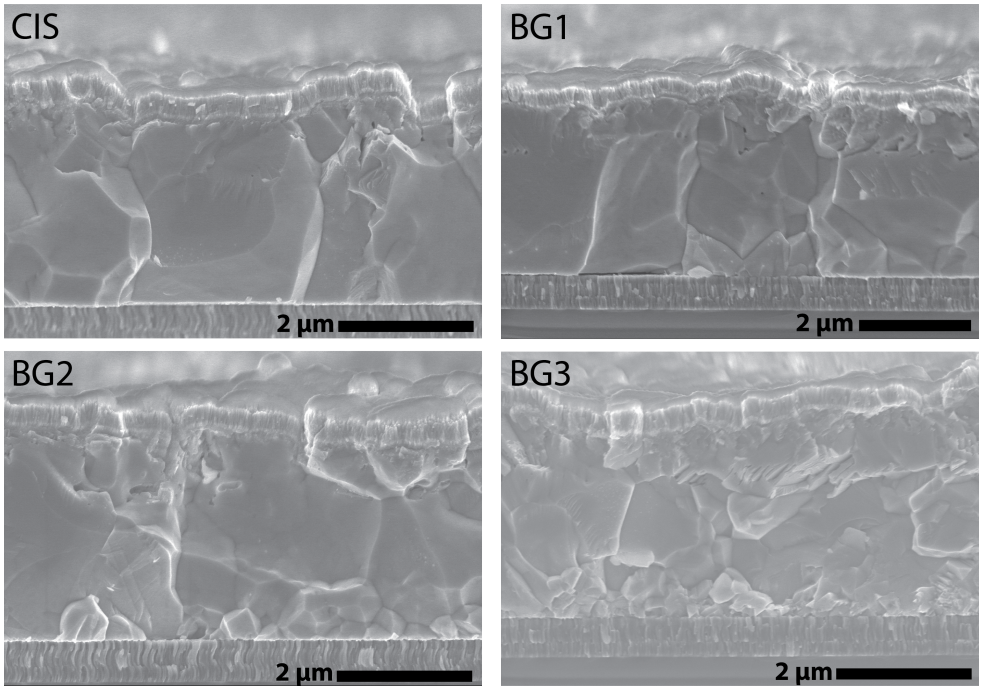


Figure 3.7: SEM micrographs of solar cell devices with different Ga back gradings. Increasing Ga content (CIS to BG3) leads to reduced grain size towards the back of the absorber.

For all compositions there are distortions visible in the area where the 3rd stage of absorber layer deposition starts (voids, crevices). Additionally, in the case of graded cells a region of smaller CIGS grains is visible near the back contact. This is in line with previous reports describing a decrease in grain size with increasing Ga content [135].

### 3.4.1 Cell performance

The addition of a back surface grading considerably improves cell performance, especially the open circuit voltage of the cells (Figure 3.8 and Table 3.3) compared to the Ga free CIS reference.

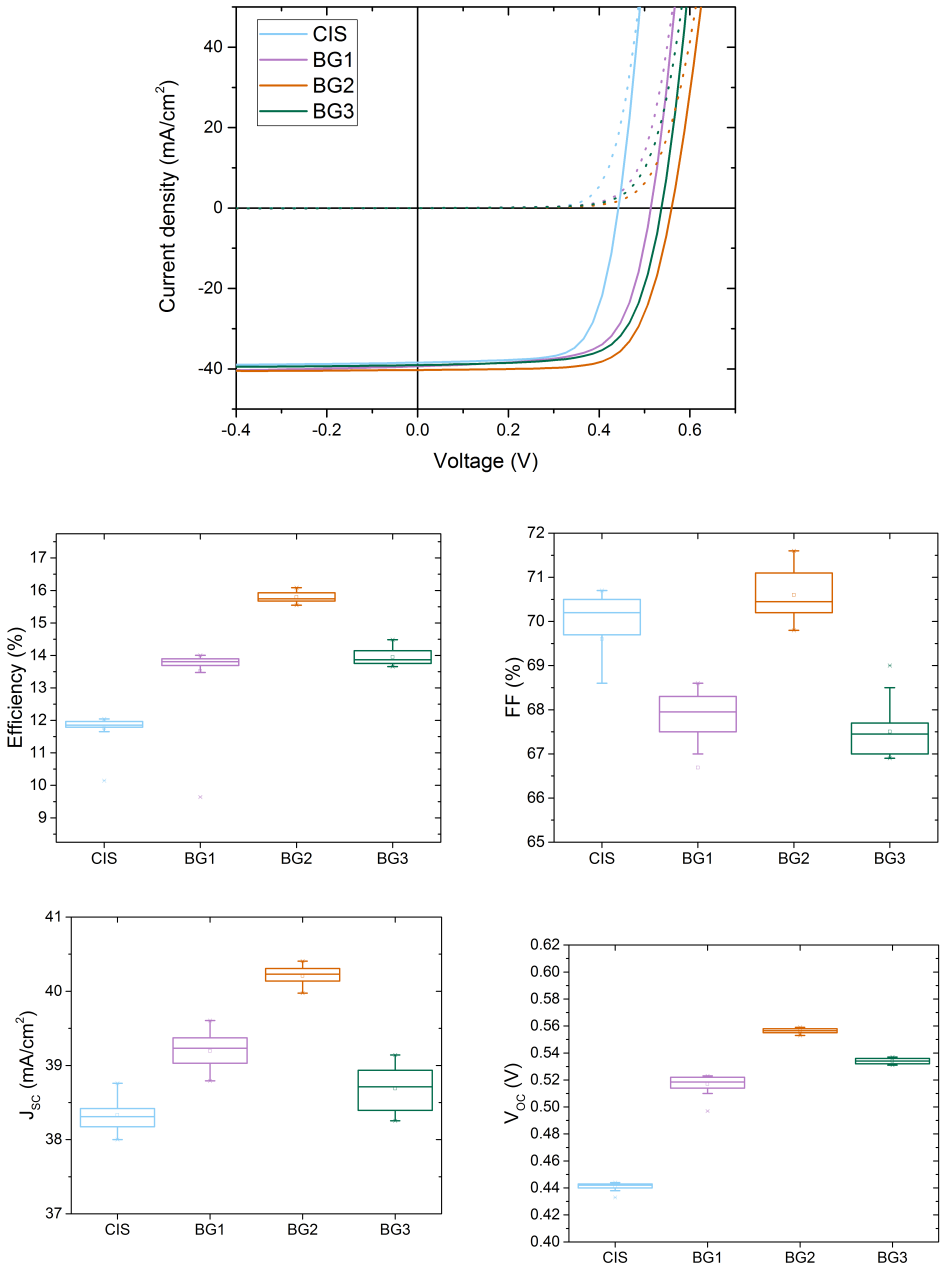


Figure 3.8: (top)Dark (dotted) and illuminated (solid) JV curves of CIS solar cells with different back gradings. (bottom) Statistical distribution of the JV parameters over 18 cells.

Table 3.3: Basic photovoltaic parameters of the highest efficiency cell for each back graded sample. Series and parallel resistances as well as diode parameters $J_0$ and A are obtained from fitting of the JV curves presented in Figure 3.8 using a one-diode model. $Rs_{illu}$ and $Rp_{illu}$ is fitted on the illuminated curve and averaged over 16 or more cells while $Rp_{dark}$, $J_0$ and A are fitted on the dark JV curve

| | $V_{OC}$ (mV) | $J_{SC}$ ($mAcm^{-2}$) | FF (%) | Eff (%) | $Rs_{illu}$ ($\Omega cm^2$) | $Rp_{illu}$ ($\Omega cm^2$) | $Rp_{dark}$ ($\Omega cm^2$) | $J_0$ ($mAcm^{-2}$) | A |
|---|---|---|---|---|---|---|---|---|---|
| CIS | 444 | 38.4 | 70.4 | 12.0 | 0.33 | 510 | 4600 | 2.05E-5 | 1.24 |
| BG1 | 519 | 39.6 | 68.2 | 14.0 | 0.23 | 460 | 1600 | 4.71E-5 | 1.54 |
| BG2 | 558 | 40.4 | 71.2 | 16.1 | 0.35 | 1240 | 2800 | 5.42E-5 | 1.66 |
| BG3 | 537 | 39.1 | 69.0 | 14.5 | 0.23 | 530 | 2500 | 1.19E-4 | 1.71 |

In addition, a notable increase in photo current ($J_{SC}$) is observed for all cells with Ga grading resulting in a high value of 40.4 $mAcm^{-2}$(designated illumination area) and a photovoltaic conversion efficiency of 16.1 % for BG2. The fill factor is low for all cells with no clear trend to link to band gap grading profile. Fitting of the JV curves using a one diode model was used to extract second level PV parameters. The cells show pronounced differences in diode quality factor and low shunt resistance (Rp) under illumination, which can lead to the observed differences in fill factor. In the following, the observed gains in $J_{SC}$ and $V_{OC}$ are discussed in more detail.

The external quantum efficiency (EQE) curves of different cells are shown in Figure 3.9. The close-up shows that the increased current for the back graded cells results from an improved EQE response in the near infrared (NIR) region. This can be explained by an improved collection efficiency for photo generated carriers deeper in the absorber compared to the pure CIS. The addition of Ga leads mainly to an increase of the conduction band [136] and a gradient in chemical potential [55]. This leads to a effective field within the quasi neutral region, extending the depth where the electrons can be extracted and contribute to the $J_{SC}$ [135]. In addition, this results in a reduced carrier concentration at the back, reducing recombination at the back contact as seen below. The cells have a different ratio between cell area and grid shading, resulting in the observed offsets of the respective EQE curves. The difference lies below 2 % and does not alter the conclusions in this work.

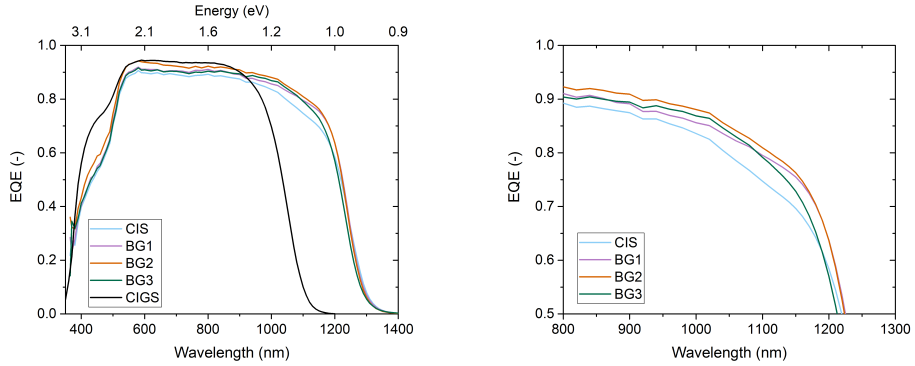


Figure 3.9: (left) External quantum efficiency of the back-graded devices. The black curve shows a typical CIGS reference [36]. (right) The close-up of the near infrared response shows a increase in collection for the cells with back grading relative to the pure CIS.

A Tauc fit of the EQE results in band gaps of 0.99 eV for the pure CIS, 1.00 eV for BG1 and BG2 and 1.01 eV for BG3 (Figure 3.10). The different slope between the graded cells and the CIS sample can be attributed to the differences in collection already seen in the EQE measurements. As a result the extraction of band gap from EQE data may be questionable, especially for the non graded case. However, very similar results were obtained from optical transmission measurements on the delaminated absorber, showing a band gap difference of about 0.02 eV between CIS and the back graded samples.

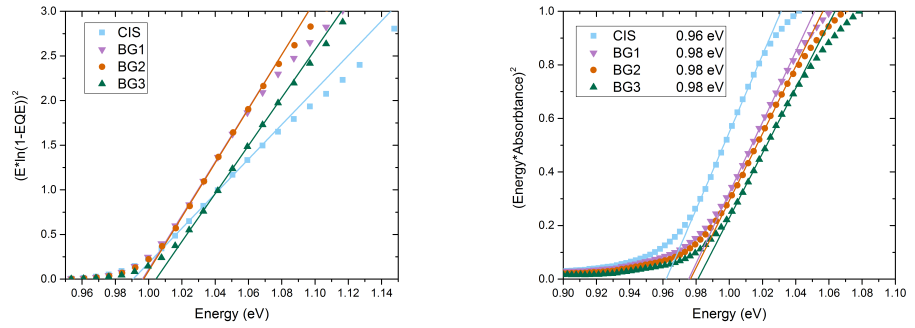


Figure 3.10: Band gap extraction by Tauc fit to the external quantum efficiency (left) and absorption data of delaminated absorbers (right). All absorbers show a band gap around 1.00 eV, with a small offset between QE and absorbtance measurements.

In order to discriminate the influence of back surface recombination from other competing processes, time resolved photoluminescence (TRPL) was measured for the pure

CIS and the BG2 sample (Figure 3.11). Both absorbers were measured as grown (on molybdenum) and after delamination of the back contact using the method developed by Bissig [123].

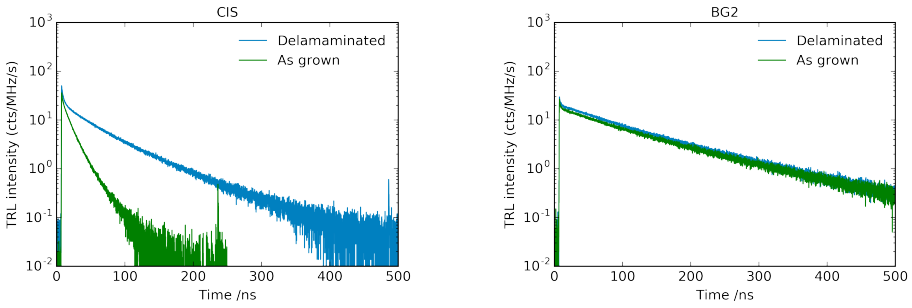


Figure 3.11: TRPL transients of absorbers without (left) and with (right) back grading. The CIGS layers are measured on the Mo back contact and after delamination.

All decay curves show a fast initial decay, followed by a single exponential decay starting after approximately 20 ns. The fast initial decay likely results from non linear radiative recombination at high injection levels and from initial carrier homogenization as described in [123], and therefore is not relevant to the discussion here. The ungraded CIS displays considerably higher apparent lifetimes after delamination from the Mo back contact (~50 ns delaminated vs. ~20 ns as grown), indicating a reduction in back surface recombination. On the other hand the same procedure has almost no influence on decay times of the back graded samples (~100 ns for both) and both samples show slower decays than even the lifted CIS sample. These results indicate that the improvements seen are a combination of reduced back surface recombination and improved bulk absorber quality. A detailed discussion of the TRPL behavior of these samples together with a model to estimate for the relative recombination rates at the back contact compared to the bulk recombination has been carried out by Bissig and Weiss and is shown elsewhere [123, 124].

Temperature dependent $J_{SC}$ -$V_{OC}$ measurements were performed at different illumination intensities to investigate the recombination characteristics [137].

The curves in Figure 3.12 show that the samples with non- or only weak back grading (CIS, BG1) display a reduced $V_{OC}$ at low temperatures for illumination close to 1 sun or above. This kind of behavior has been attributed in literature to a non-ohmic back

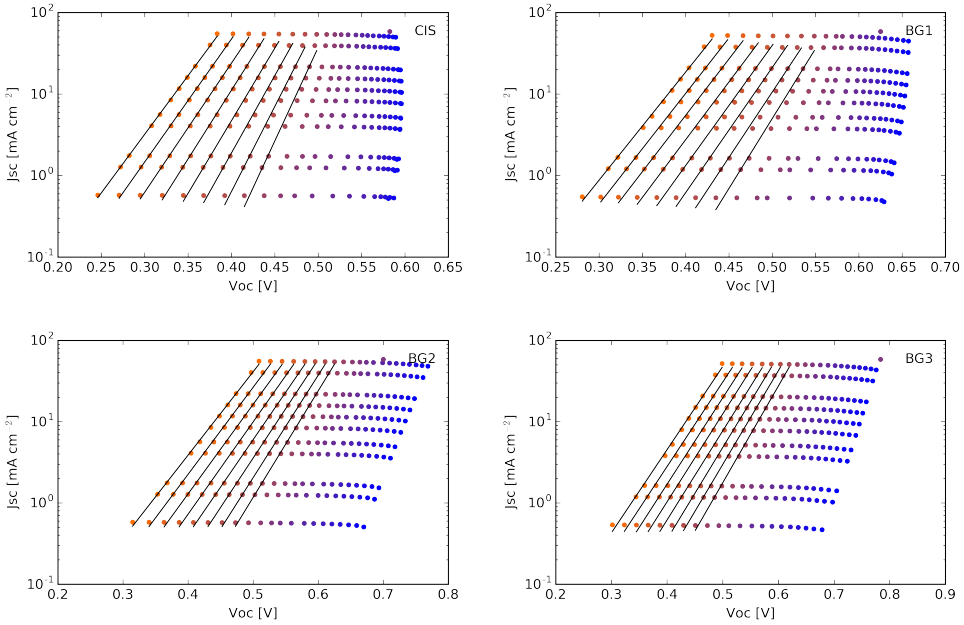


Figure 3.12: $J_{SC}$-$V_{OC}$ measurements at different temperatures and light intensities. The investigated temperatures range from 123 K (blue) to 323 K (orange). The lines show the linear fit for temperatures above 250 K.

contact or high back contact recombination [138]. Additional artefacts can be caused by heating of the sample during the measurement due to the increasing light intensity. In order to reduce the influence of these $V_{OC}$ reductions on the analysis only the data points above 250 K are taken into account for further parameter extraction.

As shown in Figure 3.13, the pure CIS cell as well as the cell with a flat grading (BG1) show diode quality factors (A) close to 1 while for the cells with stronger grading it increases towards 1.5. In the temperature range of interest, the diode quality factor is mostly independent of the temperature. The activation energy for the dominant recombination path has been extracted from $V_{OC}$-T measurements and the data are summarized in Table 3.4.

The increasing ideality factor with stronger back surface grading indicates a shift of the dominating recombination path from the quasi neutral region or potentially the interfaces towards the space charge region [139].

As described by Hölscher *et al.*, the energy extracted from $V_{OC}$-T plots exceeds the

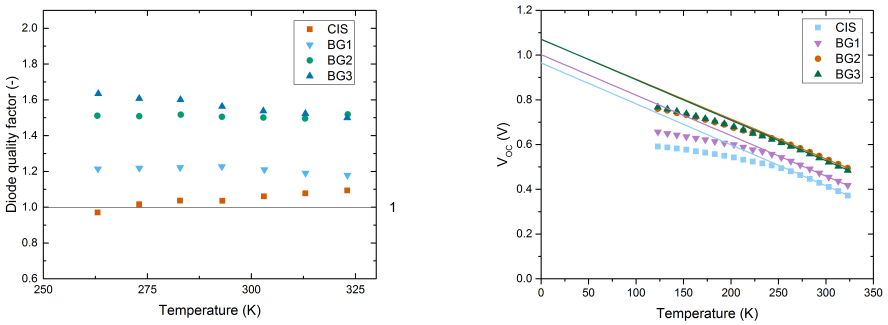


Figure 3.13: (left)Diode quality factor dependence on temperature, extracted from $J_{SC}$-$V_{OC}$ measurements. (right) $V_{OC}$-T plot for the cells investigated in this experiment. The extrapolation of the linear region yield activation energies below band gap for the non- or only weakly graded cells.

Table 3.4: Diode parameters extracted from $V_{OC}$-$J_{SC}$ and $V_{OC}$-T measurements. A is given at 293K.

| | A (-) | $E_{A,VocT}$ (eV) |
|---|---|---|
| CIS | 1.01 | 0.97 |
| BG1 | 1.14 | 1.00 |
| BG2 | 1.43 | 1.07 |
| BG3 | 1.50 | 1.07 |

activation energy of recombination by about 75 mV due to changes in the temperature-dependent thermal velocity $v_{th}$ and effective density of states $N_{c,v}$ [140]. The results here therefore indicate recombination in the narrow band gap region for the strongly graded cells (BG2 + BG3). The reduced activation energy for the cells without or only weak back grading could be attributed to the influence of back interface recombination.

In order to identify the remaining current losses in the back graded cells it is helpful to compare the measured quantum efficiency with a simulated EQE based on optical measurements (Figure 3.14). To do so, the light propagation in a multi-layer solar cell was modeled by using the transfer matrix method (TMM) formalism following the approach of Ref [14], which notably takes into account reflectance and parasitic absorption in window layers. The compositional gradings of Figure 3.6 were discretized in 25 nm thick slices and the EQE was computed as the cumulated absorption in each of the CIGS slices, i.e.

assuming perfect collection of the charge carriers. The validity of the CIGS absorption spectrum was separately assessed by the very good agreement between simulated and experimental absorption spectra for the corresponding delaminated absorbers (not shown here). In the case of the CIS sample the measured EQE is largely below the simulated values at long wavelengths (~1000-1250 nm). This can be attributed to the charge carrier collection losses in the device that also negatively impact the $V_{OC}$.

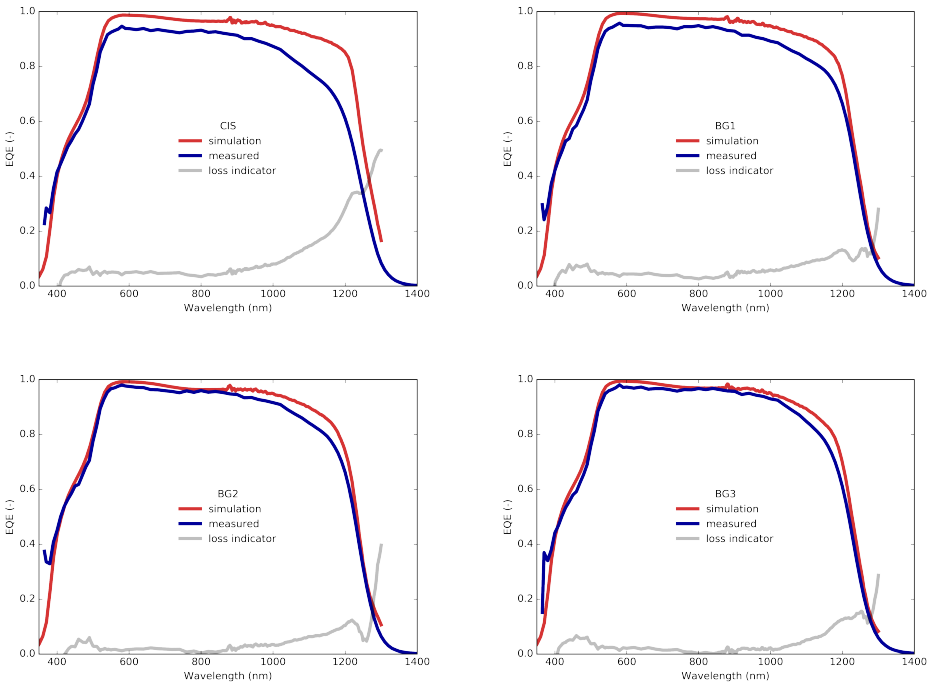


Figure 3.14: Measured (blue) and simulated (red) EQE for cells with and without back grading. The grey lines represent the loss indicator (1 - EQE/simulation), an inverse measure for the collection efficiency.

The improvement in collection of carriers in the long wavelength region is clearly visible and already significant for the weakest grading (BG1). A non-negligible collection loss in the NIR remains even for the stronger gradings, but the EQE shape becomes primarily determined by optical absorption losses, without significantly effecting the cells electric properties. A drop in EQE maximum is also seen for the cells with no or little grading, which could indicate a transport barrier in those cells. For further improvements in $J_{SC}$, a reduction of parasitic absorption and reflection losses is necessary.

### 3.4.2 Suitability for tandem devices

As discussed earlier, one major motivation for the development of 1.00 eV cells is their use in tandem devices with a perovskite top cell. To evaluate the suitability of the BG2 cell presented in this chapter, its current density in a 4-terminal tandem configuration is calculated. The semitransparent perovskite top-cell used here has a band gap of 1.61 eV and is described in [141].

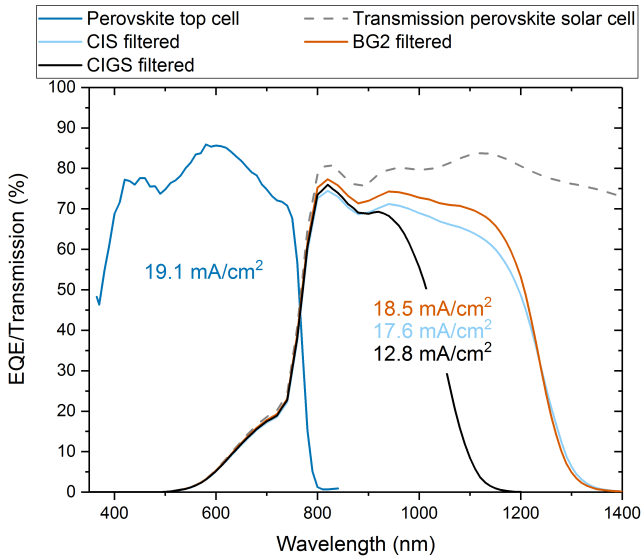


Figure 3.15: Calculated external quantum efficiency of the BG2 cell in a 4-terminal tandem device. The values within the figure give the integrated sub-cell current resulting from this EQE. The improved collection seen in Figure 3.9 leads to a considerable improvement in bottom cell current density compared to the pure CIS. Perovskite EQE and transmission data are taken from [141].

Figure 3.15 shows the calculated EQE of the CIS based cells in tandem configuration. Comparing the indicated integrated values, the cells developed here almost produce a matching current to the perovskite top cell. This is a considerable improvement over the reference CIGS and notably higher than the pure CIS, thanks to the improved spectral response in the NIR. In monolithic 2-terminal configuration at least one transparent contact can be avoided, reducing parasitic absorption between the cells. Such cells are expected to be even closer in generated current for each sub-cell.

## 3.5 Conclusion

In this chapter the possibilities of adjusting the band gap of CIS based solar cells trough group III element composition are used to improve narrow band gap (1.0 eV) solar cells. While the lower substrate temperatures (~500 °C) in the process here allows for steeper gradings than the commonly used high temperature (>550 °C) process [52, 53], it is shown here that the target of a Ga free notch composition is hard to achieve by a regular 3-stage process.

CIS based absorbers with a front grading only show no improved cell performance, as any gain in open circuit voltage is compensated by losses in fill factor and current. The front grading achieved in the experiments extended deep into the absorber (approximately 1 $\mu$m), likely exceeding the depletion region. Better results might be expected for a front grading with reduced width, possibly by depositing Ga only as a capping layer at lower substrate temperature. A front-grading by sulfurization would also be an option, as the Se/S exchange acts on the valence band instead of the conduction band, leading to an additional hole-barrier at the front interface.

The band gap grading towards the back, on the other hand, increases the efficiency of low band gap CIS solar cells considerably. The resulting cells show an improved collection of charge carriers in the near infrared region while the EQE band gap remains unchanged with an absorption onset at 1.0 eV. This result is especially relevant for bottom cells in current matched 2-terminal tandem devices. By selectively modifying the back interface it was shown that back surface recombination is a mayor issue in the ungraded cells, and that the implementation of the grading can mitigate this issue. The combination of improved bulk and reduced back surface recombination leads to a high $V_{OC}$ of almost 560 mV for the cells with band gap grading towards the back. The highest efficiency of 16.1 % demonstrated here represents a significant improvement from the previose 15.0 % for solar cells with optical band gap of 1.0 eV. Such cells are a highly promising partner for monolithic and 4-terminal thin film tandem devices and the PV performance shown here highlights the suitability of this approach.

# 4 Alkali doping in CIS based solar cells

As discussed in Chapter 1 the implementation of alkali fluorides has been an important milestone in the development of high efficiency CIGS solar cells. Especially for cells grown on alkali free substrate (e.g. polyimide or stainless steel), additional supply of alkali fluorides by post treatment has been crucial to reach high performance. While the samples in this work are grown on soda lime glass, the substrate temperature during deposition is comparatively low, making it necessary to supply not only the heavy alkali elements, but also Na by post deposition treatment [36, 51, 76]. This chapter discusses the effects and peculiarities of alkali fluoride post treatment for CIS based solar cells.
The incorporation of sodium is studied on ungraded CIS absorbers, while the experiments with rubidium fluoride are conducted on absorbers with a Ga back-grading as described in Chapter 3.

This chapter is partly based on the following publication:

[117] Thomas Feurer, Fan Fu, Thomas Paul Weiss, Enrico Avancini, Johannes Löckinger, Stephan Buecheler, Ayodhya N. Tiwari, *RbF post deposition treatment for narrow bandgap Cu(In,Ga)$Se_2$ solar cells*, Thin Solid Films, Volume 670, 2019, Pages 34-40

*TOF-SIMS measurements are provided by Dr. Enrico Avancini.*

## 4.1 Sodium in CIS solar cells

Sodium incorporation is essential for the doping of CIGS type solar cells, increasing the acceptor density in the absorber by a reduction of compensation [142, 143]. Different methods of Na incorporation have been established over time, notably the traditional in-diffusion from the soda-lime-glass substrate, precursor layers, co-evaporation and post deposition treatment approaches [50,69]. For the CIS cells used here, the highest apparent doping density, as well as the best solar cell parameters were realized using a combination of supply from the substrate glass and post deposition treatment (PDT) (Figure 4.1 and Table 4.1).

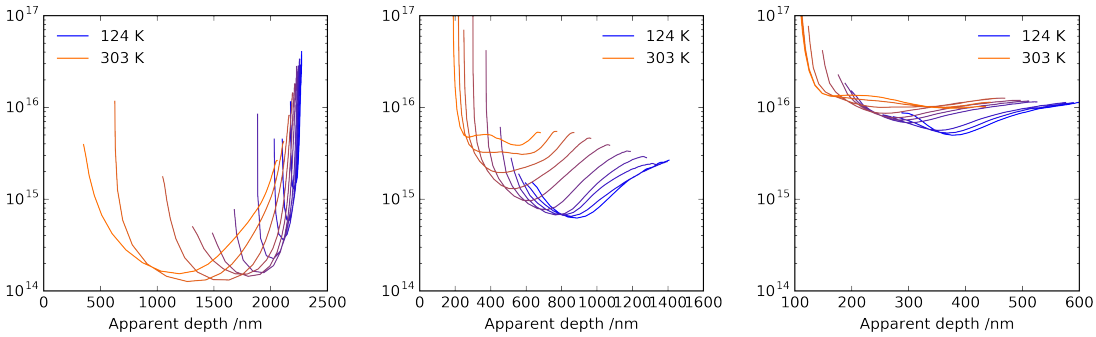


Figure 4.1: Apparent doping levels from capacitance-voltage measurements for CIS solar cells with: a) no sodium from the glass and no PDT, b) no sodium from the glass and with PDT and c) with sodium from the glass and with PDT.

While this combination improves the performance of CIS solar cells grown at reduced temperatures from 5.6 % to 10.9 %, this is still well below the 15.0 % of state of the art CIS devices grown at high temperatures [30].

For further efficiency improvement, an additional annealing step after the post deposition treatment was introduced. This in-situ annealing was carried out at the temperature of the PDT (~ 370 °C) and was carried out under Se atmosphere, without breaking vacuum between the two steps. Considerable improvement is observed with additional in-situ annealing over all photovoltaic parameters (Figure 4.2).

All parameters show an optimum at 20 minutes in-situ annealing, after witch the prop-

Table 4.1: Parameters of CIS solar cells with different sodium supply schemes (average of the top 10 cells). "Barrier" refers to a $SiO_2$ alkali diffusion barrier below the Mo. The product of $V_{OC}$ and FF is added as an additional figure of merit.

| | $V_{OC}$ (V) | $J_{SC}$ ($mAcm^{-2}$) | FF (%) | Eff (%) | $V_{OC}$*FF |
|---|---|---|---|---|---|
| CIS w/ barrier no PDT | 0.274 | 37.8 | 54.4 | 5.6 | 0.149 |
| CIS w/ barrier w/ PDT | 0.381 | 37.3 | 64.1 | 9.1 | 0.244 |
| CIS no barrier no PDT | 0.421 | 36.9 | 63.2 | 9.7 | 0.266 |
| CIS no barrier w/ PDT | 0.432 | 35.7 | 70.5 | 10.9 | 0.305 |

erties start to decay again. The improvement is also clearly visible in the shape of the EQE curves before and after the annealing (Figure 4.3). Absorbers without in-situ annealing lead to an EQE response that increases with wavelength. Such an increase in collection can be the result of a large depletion region. As a result, holes will be minority carriers for a considerable part of the absorber and can recombine while drifting towards the back contact [55]. Cells with annealed absorbers show the typical EQE decrease with increasing wavelength. A strong collection loss is seen in the near infrared region, which is related to the recombination at the back contact as described in Chapter 3.

These results are in line with an increase in the apparent doping (Appendix A.1) with in-situ annealing. It is further supported by an increase in sodium concentration in the absorber as measured by SIMS (Appendix A.2). The distribution also shows that the Na profile changes for 30 minutes of in-situ annealing, indicating a change in the surface layer. This may be the reason for the decreasing performance after 20 minutes of annealing. Using a 20 minutes annealing time, pure CIS solar cells with an open circuit voltage of 501 mV, a current density of 40.9 $mAcm^{-2}$ and a FF of 73 % were produced, resulting in an efficiency of 15.0 % (J-V curve in Figure 4.3).

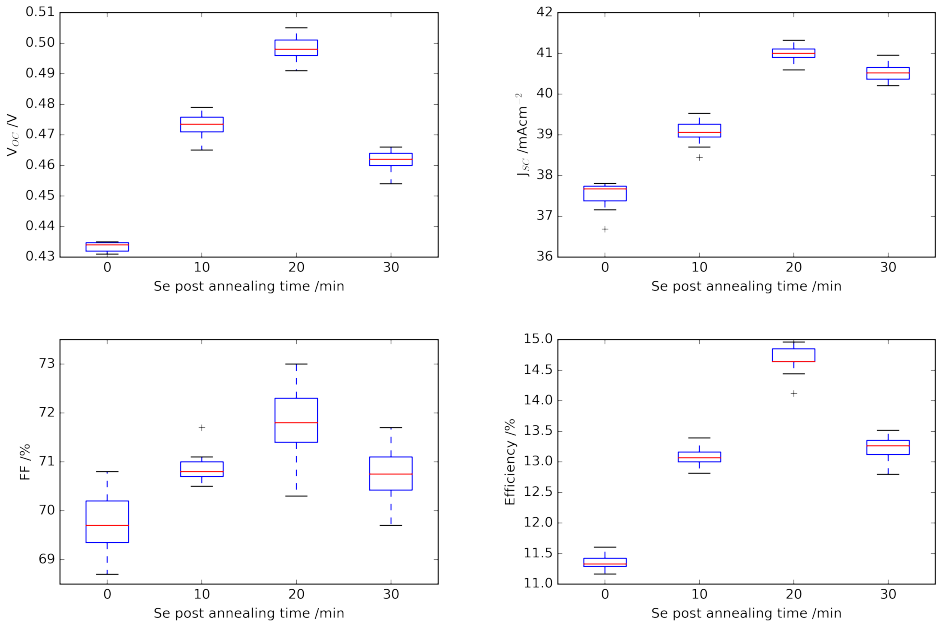


Figure 4.2: Photovoltaic parameters of CIS solar cells with different times of Se annealing after NaF PDT.

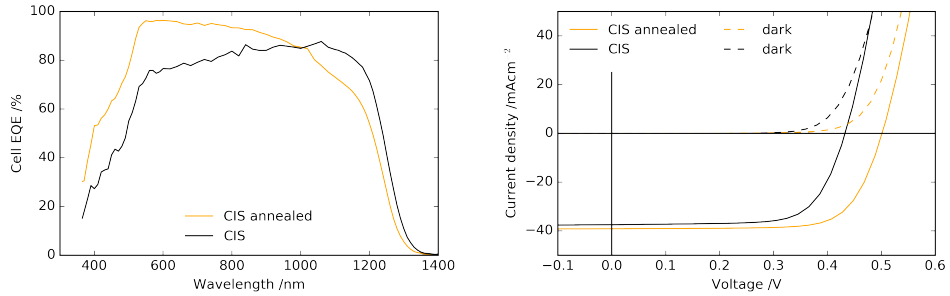


Figure 4.3: EQE and J-V curves of CIS solar cell without and with 20 min Se in-situ annealing after NaF PDT.

## 4.2 RbF in CIS based solar cells

For the rest of this chapter, the absorbers used are back-graded CIS of the type described as "BG2" in Chapter 3.

As already discussed in Chapter 1, the implementation of heavy alkali post treatments has lead to considerable improvements in CIGS technology, leading to several record efficiencies following the introduction 2013 [15, 36, 77].

Here, an implementation of RbF PDT similar to the one described in [19] was chosen. The RbF PDT is carried out directly after the NaF PDT and the duration is selected to be 20 min in order to replace the in-situ annealing described above. Initial experiments have resulted in reduced performance compared to the NaF only case, especially showing a substantial drop in $V_{OC}$ (Figure 4.4).

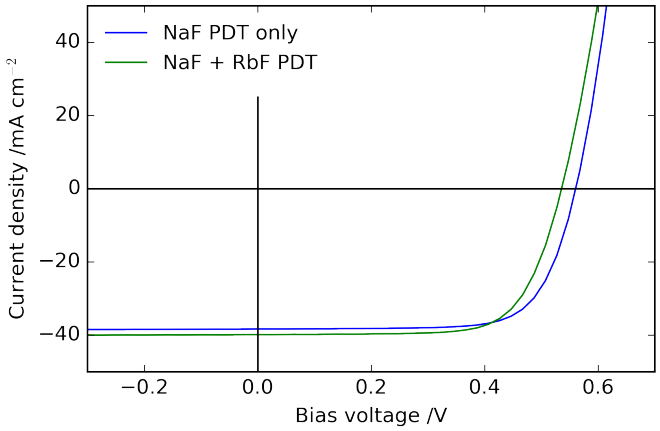


Figure 4.4: J-V curves of CIS based solar cells with only NaF and with NaF+RbF post treatment. Both cells measured shortly after growth without AR coating.

### 4.2.1 Aging behavior

During the investigation of RbF treated CIS, an improvement in cell properties is observed for all devices upon storage in dark (room temperature, in air) (Figure 4.5). This is in contrast to cells with a double Ga grading and wider band gap [83], as well as to the

samples without RbF treatment, where no increase of properties over time is observed.

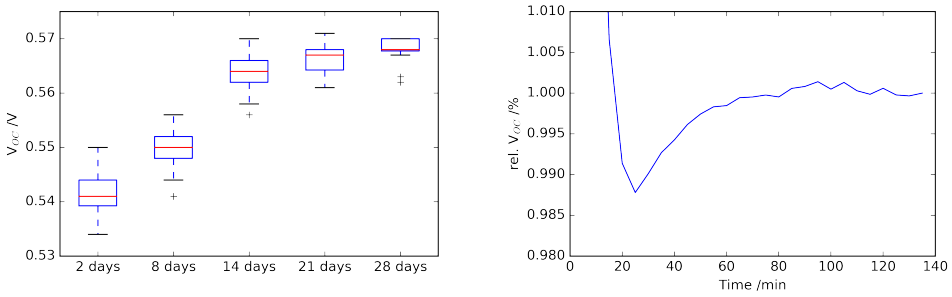


Figure 4.5: Evolution of $V_{OC}$ of RbF treated CIS over time. The box plot shows the behavior for cells stored at room temperature in air and in the dark (18 cells). The figure to the right represents the change in $V_{OC}$ (relative) during heat light soaking. The initial drop represents the heating up of the sample.

The improvements are mainly seen in $V_{OC}$ and lead to cell efficiency increase of about 5 % (relative) after 1 month. A similar effect is achieved by heat-light soaking (HLS) for about 2 hours at 80 °C, indicating the possibility of a kinetically hindered process. Comparing the apparent doping of the samples before and after aging we notice a flattening of the doping profile, but no change in net doping concentration that could explain the improvements in $V_{OC}$ (Figure 4.6).

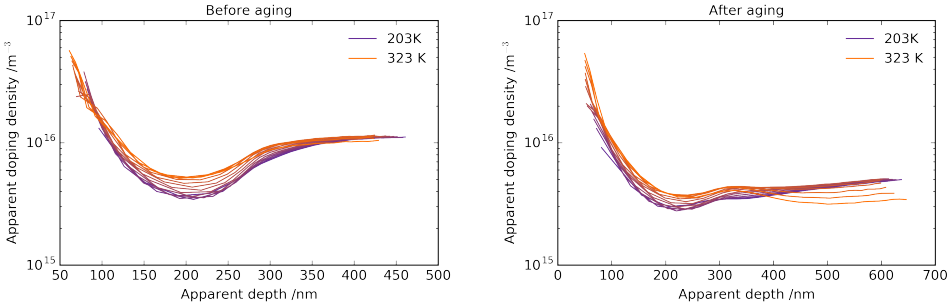


Figure 4.6: Apparent doping extracted from capacitance-voltage measurements for cells with RbF post treatment before and after aging.

Temperature depending $V_{OC}$ measurements indicate a change in recombination mechanism (Appendix A.3). Further TOF-SIMS investigations show no significant change in the alkali depth profile (Appendix A.4), although no information is obtained for the more local distribution. Based on this measurements, no mechanism for this gradual improvement

can be proposed. For a better understanding of this process, further investigations may include lifetime and quasi Fermi-level splitting measurements to separate between bulk and interface effects, localized compositional analysis to investigate potential element diffusion, and temperature dependent aging in order to investigate the activation energy of such process, but were not part of this work.

All data given in the next sections are stabilized values after aging to ensure comparability.

### 4.2.2 PDT conditions

RbF PDT was applied to back-graded CIS as described in Chapter 3 under different substrate temperature (Figure 4.7) and evaporation rate conditions (Figure 4.8).

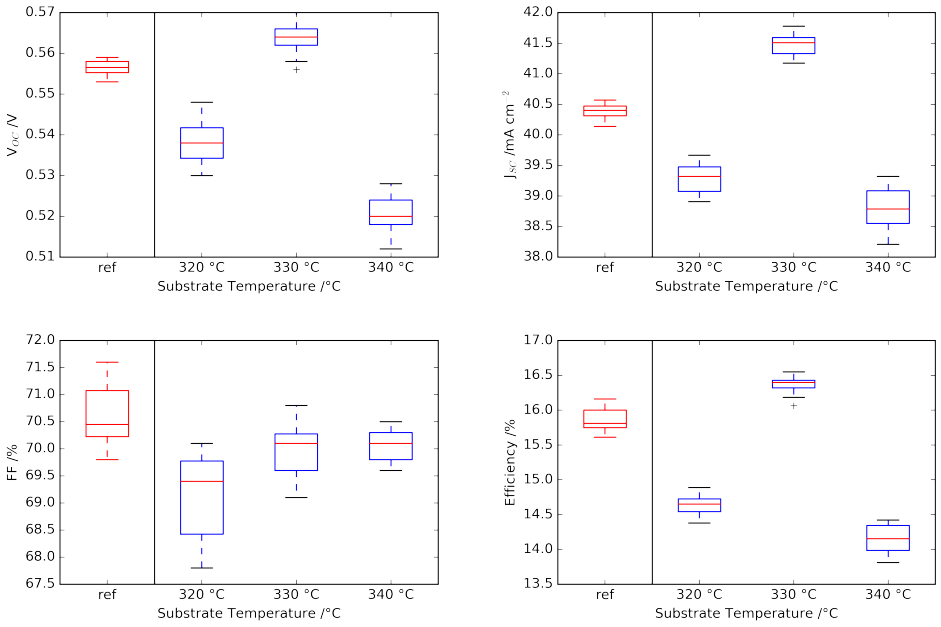


Figure 4.7: PV parameters for cells with RbF PDT at different substrate temperatures. All RbF depositions were made using evaporation source temperature of 500 °C. Each dataset contains 18 cells. An absorber without RbF PDT (BG2 in Chapter 3) is used as reference.

While the substrate temperature shows a clear optimum close to 330 °C, the sublimation rate of RbF seems more forgiving, showing a wide region with high performance between

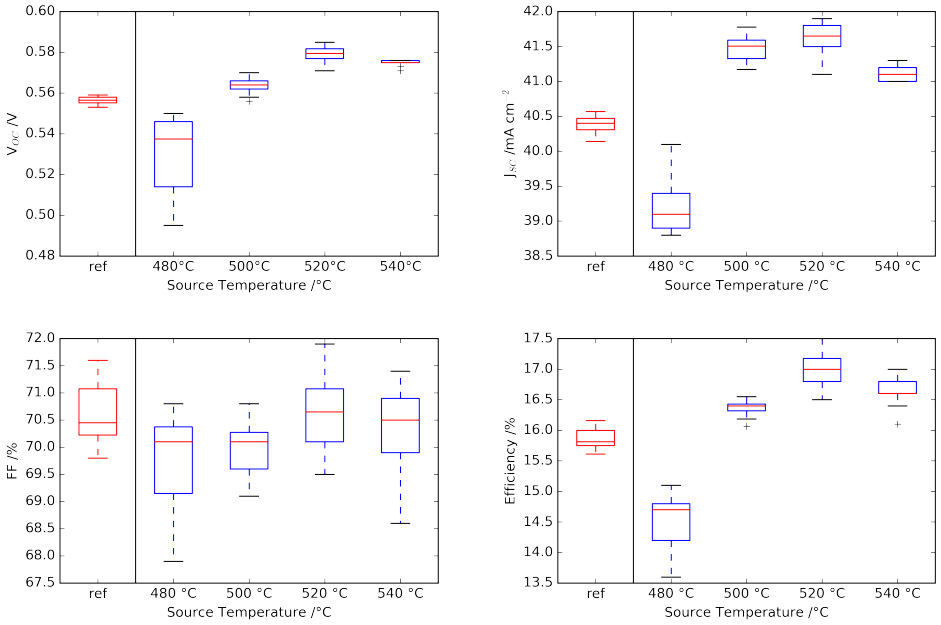


Figure 4.8: PV parameters for cells with RbF PDT at different source temperature, representing different RbF effusion rates. All depositions were carried out at a substrate temperature of 330 °C. Each dataset except the last contains 18 cells. For 540 °C only 9 cells are included, as half of that sample has been separated for additional measurements. An absorber without RbF PDT (BG2 in Chapter 3) is used as reference.

500 °C and 540 °C evaporation source temperature, corresponding roughly to half an order of magnitude in vapor pressure [144]. For all PDT conditions the main improvements can be seen in $V_{OC}$ and short circuit current ($J_{SC}$). The current gain is partly explained by the reduced CdS thickness necessary for RbF treated samples as described for CIGS in literature [36, 83], but also contains a component of overall improvement of quantum efficiency response (see Figure 4.9).

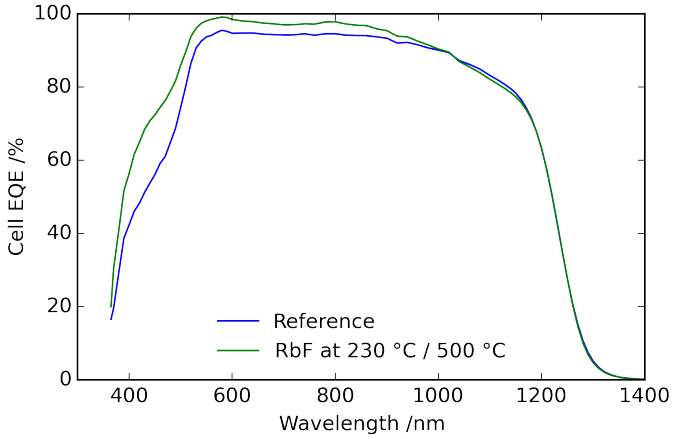


Figure 4.9: Comparison of the external quantum efficiency of solar cells produced from absorbers with and without RbF post deposition treatment.

For high amounts of RbF (at ~540 °C), the efficiency of the solar cells is decreasing with a reduction in fill factor and current density. Additional temperature dependent current-voltage measurements show a blocking of the photocurrent (Figure 4.10).

### 4.2.3 Effects of RbF post treatment

The alkali distribution within the absorbers has been measured by SIMS. A substitution of Na and K by Rb has been observed within the front part of the absorber layer (Figure 4.11). Similar behavior was reported for state of the art CIGS absorbers [15, 82] where a replacement throughout the absorber was observed. It has been shown that Rb tends to segregate at grain boundaries, replacing the lighter alkali elements [80]. We assume the difference between front and back stems from the particular morphology of the single

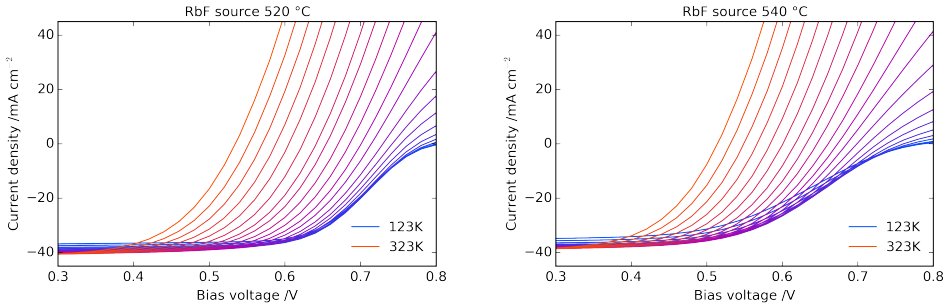


Figure 4.10: Temperature depending J-V measurements for cells with a sufficient (left) and excessive (right) amount of RbF. An additional blocking of the photo-current starts to appear at lower temperatures for the cells with high RbF flux.

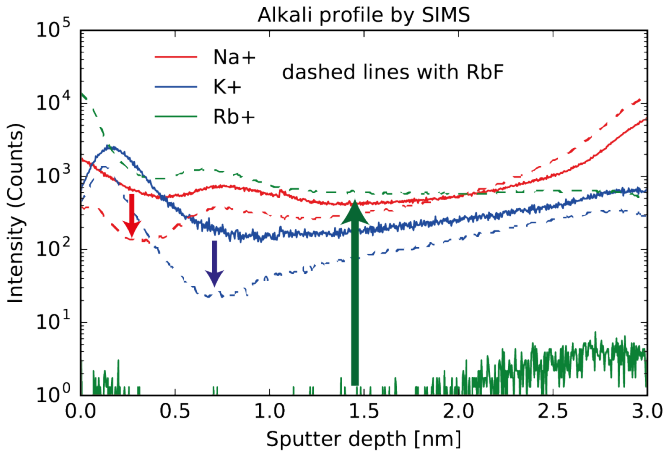


Figure 4.11: Alkali distribution for cells with and without RbF post deposition as measured by SIMS.

graded cells, where the absorber changes strongly from a large grained surface area to smaller grains in the Ga graded part towards the back contact (see chapter 3 for a comparison to ungraded samples). The supplied/diffused amount of RbF effectively replaces sodium in the front region, but it may not be enough to fully replace it at the back where a high concentration of random grain boundaries is found, leaving room for the sodium to accumulate.

TRPL measurements show a significant increase in effective lifetime from ~100 ns to over 400 ns for absorber layers treated with RbF (Figure 4.12). This suggests that a reduction of non-radiative recombination is responsible for the enhancements. The derivation

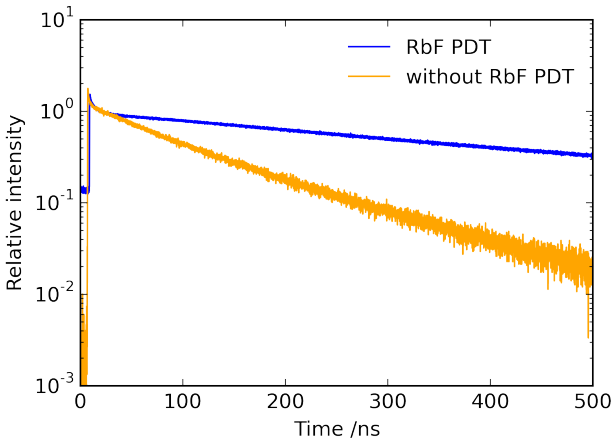


Figure 4.12: TRPL decays for back graded cells with and without RbF PDT. The intensity has been normalized for better comparison.

described in [145] can be used to estimate the resulting change in quasi Fermi-level splitting. Assuming low injection conditions and no change in doping (as roughly indicated by the CV measurements), the hole Fermi-level will remain unchanged by the PDT. The electron Fermi-level will be influenced by the density of excess charges $\Delta n$ which, using a unchanged generation function $G$ (same band gap and illumination) is proportional to the TRPL lifetime:

$$\Delta n = G * \tau_{TRPL} \tag{4.1}$$

The electron Fermi-level $E_{fn}$ will adjust to accommodate the excess carriers

$$\Delta n + n_0 = N_C * exp(-\frac{E_C - E_{fn}}{k_B T}) \tag{4.2}$$

With a identical band gap, and thus identical conduction band maximum $N_C$ and intrinsic charges $n_0$, a change in lifetime by a factor of 4 will change the quasi Fermi-level spiting by $ln(4) * k_B T \approx 36\ meV$. While it is not straight forward that the charge carrier dynamics in the pulsed measurement is similar to the continuous illumination during operation, the good mach of the estimated quasi Fermi-level splitting and the change in $V_{OC}$ of 37 meV indicates the validity of this approach.

Admittance measurements show suppression of the high temperature capacitance dispersion at low frequencies for cells with RbF treatment compared to the reference (Figure 4.13).

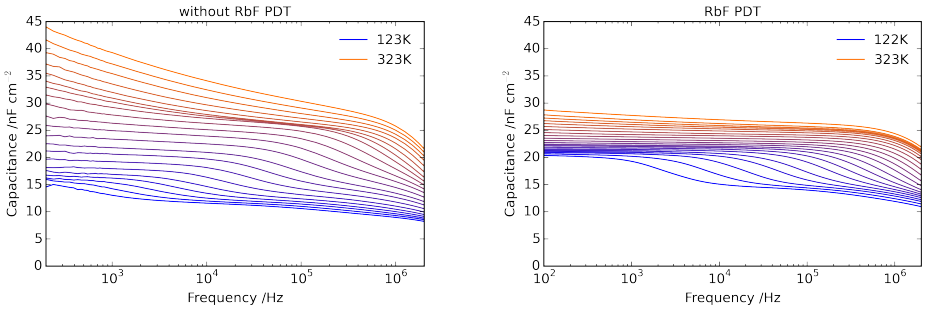


Figure 4.13: Capacitance-Frequency plots of cells without (left) and with (right) RbF post treatments.

This could be caused by a defect outside our measurement range or a reduction of tail states and inhomogeneities [146]. A broad capacitance transition is generally attributed to the bulk (space charge region) of the absorber rather than to the interface [121], which hints to an improvement in the bulk of the absorber. For the main step, an activation energy around 125 meV is extracted (using the method described in [121]) for both cases, suggesting that the underlying defect or barrier does not change with the RbF PDT.

In summary these measurements show that post treatment with RbF is improving CIS solar cells in the bulk and at the buffer interface by effectively reducing the non-radiative recombination and the necessary amount of CdS buffer. Extensive RbF PDT leads to a blocking of the photo-current, limiting the maximum amount RbF that can be deposited before cell parameters decrease.

### 4.2.4 Certified cell performance

Figure 4.14 shows the JV and EQE curves for a cell fabricated with single Ga back grading and with RbF PDT at ~330 °C substrate temperature and RbF source temperature of 500 °C as certified by Fraunhofer ISE. The respective photovoltaic properties are $V_{OC}$ = 595 mV, $J_{SC}$ = 42.0 mAcm$^{-2}$, FF = 71.9 % and an efficiency of 18.0 % (certification in

Appendix C), a record for solar cells with a bandgap of 1.0 eV. Comparison of the $V_{OC}$ with the EQE band gap and the SQ limits shows a very low $V_{OC}$ deficiency of around 405 meV and SQ-$V_{OC}$ difference of 155 meV, comparable to state of the art solar cells with wider band gap [147, 148].

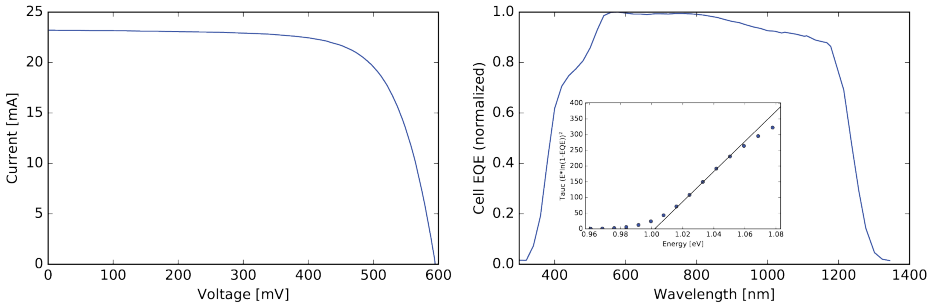


Figure 4.14: J-V and EQE of a RbF treated CIS solar cell with a band gap of 1.00 eV, certified at Fraunhofer ISE. The inset shows band gap extraction by Tauc fit of the EQE measured in house.

## 4.3 Implementation in tandem devices

To investigate the potential of the alkali treated low band gap cells for tandem application with perovskite top cells, a separated 4-terminal test has been carried out. To calculate the EQE and current density of the CIS cell in a 4-terminal configuration tandem device, the transmission data measured from a full perovskite top cell similar to the one published in [141] was multiplied with the EQE response measured for the CIS bottom cell. I-V measurements were carried out using a combination of long-pass and neutral density filters to reproduce the illumination level below the perovskite cell, and to prevent excitation in the CdS layer. Bottom- and top-cells were then measured independently. The results are shown in Figure 4.15 and Table 4.2. Even in a 4-terminal design without index matched coupling between the cells, the current density of 18.4 $mAcm^{-2}$ for the filtered CIS cell approaches the 19.2 $mAcm^{-2}$ of the perovskite top cell, promising a good current matching for potential future monolithic devices.

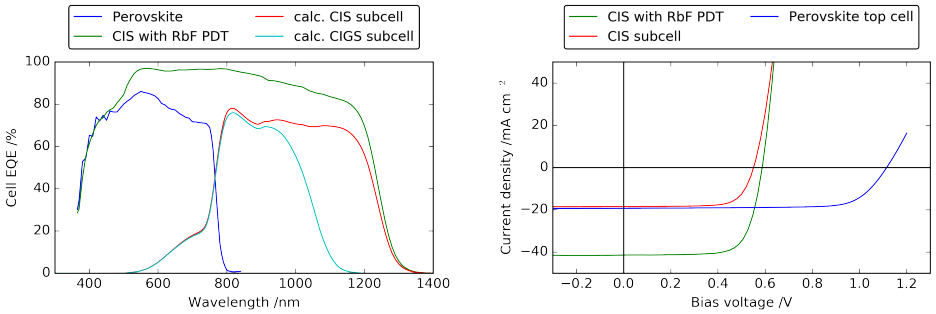


Figure 4.15: (left) Measured EQE of the CIS and perovskite top cells. The calculated EQE's for the CIS as well as a regular band gap CIGS solar cell [36] in 4-terminal configuration based on perovskite transmission are included. (right) J-V curves of the sub cells in 4-terminal tandem configuration. The CIS bottom cell is measured using long pass- and neutral density filters to replace the perovskite top cell.

Table 4.2: Solar cell performance of the 4-terminal CIS/perovskite tandem device

| | $V_{OC}$ (mV) | $J_{SC}$ (mAcm$^{-2}$) | FF (%) | Eff. (%) |
|---|---|---|---|---|
| CIS standalone | 587 | 41.4 | 73.2 | 17.8 |
| Perovskite top cell | 1'115 | 19.2 | 75.2 | 16.1 |
| CIS sub cell | 550 | 18.4 | 73.0 | 7.4 |
| Efficiency in 4-terminal tandem configuration | | | | 23.5 |

## 4.4 Conclusion

In this chapter, similarities and differences between the post deposition treatment of CIS baseed solar cells and traditional double-graded CIGS are investigated. It is shown that for a growth process at low temperature (~500 °C) considerable changes in the post treatment procedure are necessary to achieve sufficient doping levels in CIS absorbers. Specifically, Na supply from the substrate as well as from a post treatment with NaF and an additional annealing step after the PDT is applied. This can be related to the higher migration energies for alkali metals in CIS compared to CGS [149] and the larger grain size for the bulk of CIS based absorbers compared to CIGS grown under similar conditions.

For RbF treated solar cells, improvement in the PV parameters after completion of the cells is observed over time scales of days at room temperature storage. The process can reliably be accelerated by heat-light soaking at 80 °C, but further investigations are necessary to identify the underlying mechanism. Beside this aging, the substrate temperature has been shown to be the most crucial parameter for the effectiveness of the RbF post treatment. At optimized conditions, an increase in $V_{OC}$ and $J_{SC}$ is observed for treated cells, stemming from a reduction in non-radiative recombination and a thinner CdS buffer layer. These effects are similar to the ones described for double-graded absorbers [15, 83, 90]. Using the optimized PDT procedure, a certified record efficiency of 18.0 % is achieved for a cell with an optoelectronic band gap of 1.00 eV. In combination with a 16.1 % perovskite top cell, a 4-terminal efficiency of 23.5 %, with almost matching current densities for both sub-cells, is shown.

# 5 Cu content in CIS based solar cells

High efficiency CIGS solar cells are grown with significant sub-stoichiometric Cu compositions, resulting in a high density of defects. Potential for cell efficiency improvements through increasing the Cu concentration closer to stoichiometry have been discussed in the field for many years, but were never realized: prior to this work cells with high Cu concentrations showed decreased photovoltaic parameters.
In this chapter it is shown that RbF post deposition treatment of CIS solar cells allows to capture the benefits from the improved absorber quality with increasing Cu content close to stoichiometry.

This chapter is partly based on the following publication:

[150] Thomas Feurer, Romain Carron, Galo Torres Sevilla, Fan Fu, Stefano Pisoni, Yaruslav E. Romanyuk, Stephan Buecheler, Ayodhya N. Tiwari, *Efficiency Improvement of Near-Stoichiometric $CuInSe_2$ Solar Cells for Application in Tandem Devices*, Advanced Energy Materials, 2019

## 5.1 State of the art

Structural defects play an important role in semiconductor materials and devices. Point defects especially, such as vacancies, impurities, anti-sites, and interstitials, as well as the defect pairs of those, are known to influence the electronic properties of the materials. The effects can be beneficial, as for the doping of the semiconductor, or detrimental by providing centers of recombination and trapping [151, 152]. For highly efficient CIGS solar cells, semi-empirical optimization of the elemental composition lead to an optimum Cu to group-III element ratio (CGI) in the range of 0.80 to 0.90 [36, 55, 153, 154]. As a result of this off-stoichiometric, Cu deficient composition, a high density of native defects exist within the absorber layer [155, 156]. The remarkably low formation energies of some of these defects results in the formation of defect complexes and possibly even phases of ordered defect compounds [157, 158]. Increasing the Cu content towards stoichiometry can considerably reduce the presence of such defects and defect complexes. It has been shown that stoichiometric Cu concentrations can be beneficial for absorber crystallinity [159], defect density [155, 159], mobility [160, 161] and doping density [160–162]. Despite this, solar cells based on Cu stoichiometric $CuInSe_2$ have never reached efficiencies above 13.5 % [155, 163–165]. CIS cells with high CGI are mainly limited by a low open circuit voltage ($V_{OC}$), and to a lesser extent, by a reduced fill factor (FF) and current density (Figure 5.1).

The cells show a decrease in maximum EQE value as well as a reduction in the activation energy extracted from temperature dependent $V_{OC}$ measurements (Figure 5.2).

Both results indicate the presence of recombination at the front interface, as already described in the literature [163]. In this comparison, the Cu poor sample shows an activation energy above the optical band gap of the absorber, an effect previously observed for CIGS solar cells and is attributed in literature [140, 146] to the temperature-dependent thermal velocity and effective density of states . The implementation of a Cu deficient surface layer has shown to recover the $V_{OC}$ loss in those high CGI cells, while a decrease in current density remains and is attributed to tunneling recombination [163, 166]. Similar improvements of the absorber surface have been achieved with alkali treatments after

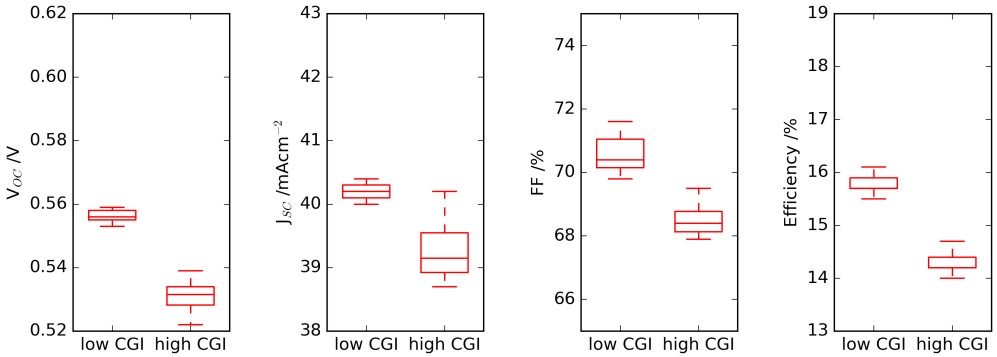


Figure 5.1: J-V parameters of CIS based solar cells with low (0.87) and high (0.93) Cu concentrations in the absorber. A degradation over all parameters is observed when going to more stoichiometric compositions. Each data-set contains 18 individual cells.

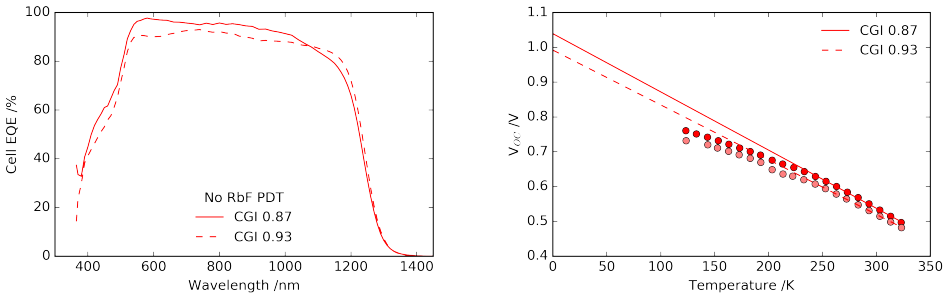


Figure 5.2: EQE (left) and temperature dependent $V_{OC}$ (right) of CIS based solar cells with low and high Cu concentrations in the absorber. Both cells show comparable band gap, but the activation energy extracted by fitting the linear part of the $V_{OC}$-T plot is considerably lower for the high Cu sample.

etching of the secondary phases in Cu rich samples [167, 168], although most recent results indicate this treatment may passivates defects that were, at least partly, generated by the etching in the first place [169].

## 5.2 High Cu for cells with RbF post deposition treatment

The post treatment with heavy alkali elements has been reported to reduce recombination in the absorber bulk and at the interface (e.g. [83, 90] and Chapter 4). Therefore the influence of RbF post deposition treatment on CIS based absorbers with increased Cu con-

centrations is investigated (Figure 5.3). The Cu content is adjusted by varying the amount of Cu excess deposited between second and third stage of the deposition (Chapter 2).

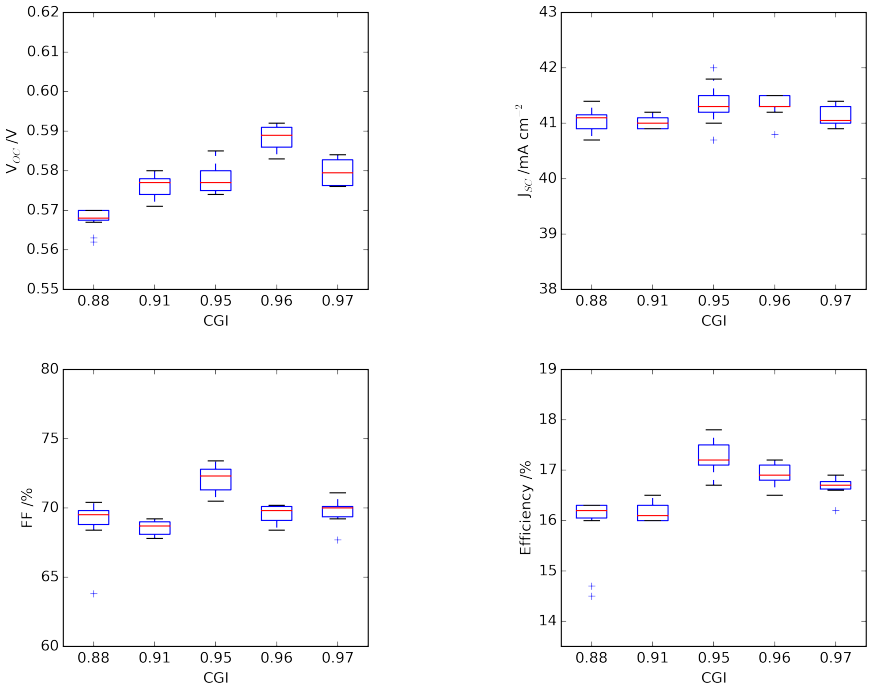


Figure 5.3: J-V parameters of CIS based solar cells with variing CGI and RbF post deposition treatment at 500 °C source temperature. A improvement of overall performance is observed, with a maximum in efficiency at a CGI of 0.95 and the highest $V_{OC}$ at 0.96. Each data-set contains 9 individual cells.

While the samples without RbF have shown a pronounced decrease in photovoltaic parameters, most notably a drop in $V_{OC}$ of approximately 20 mV, the rubidium-treated samples improve with increasing copper concentration. A maximum in efficiency is observed at a CGI of 0.95, while the highest $V_{OC}$ is measured at 0.96. Higher concentrations show a decrease in properties again. Please note that the copper concentrations given here are measured by XRF and therefore contain an experimental error ($2\sigma$) of $\pm 0.03$. Some selected samples from this chapter have been re-measured by ICP-MS, but the results do not derivate significantly from the values shown here (see Appendix B.1).

Based on the results in Chapter 4, the RbF source temperature is increased to 530 °C, corresponding to roughly a doubling of the amount of evaporated RbF (Figure 5.4). No photo-current blocking (as compared to Figure 4.10) is observed for the high Cu absorbers

(Appendix A.5). For low CGI samples, a gain of about 25 mV is achieved with RbF

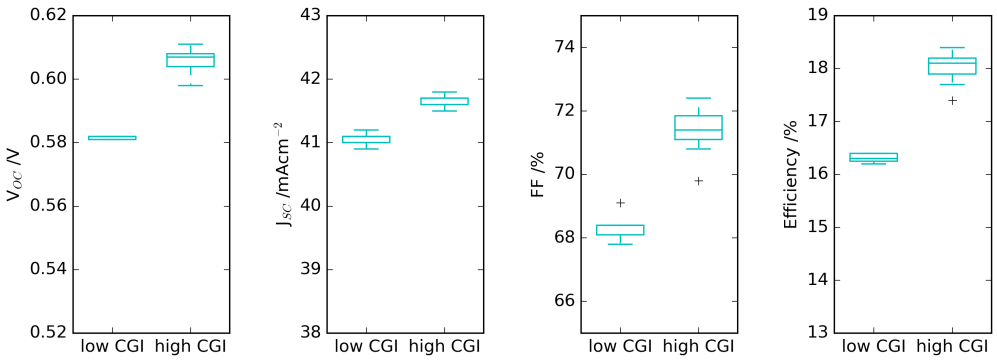


Figure 5.4: J-V parameters of CIS based solar cells with low (0.87) and high (0.96) Cu concentrations in the absorber and RbF post deposition treatment at 530 °C source temperature. A considerable improvement over all parameters is observed when going to a more stoichiometric composition. Each data-set contains 18 individual cells.

PDT, similar to the samples in Chapter 4 or the increase observed for double-graded absorbers [15, 83]. The high Cu content samples on the other hand show a remarkably higher improvement of ~ 80 mV with RbF treatment, yielding a $V_{OC}$ of 611 mV (best cell value, 606±4 mV on 18 cells).

Figure 5.5 shows the apparent doping density extracted from capacitance-voltage measurements on samples with a high amount of RbF during PDT. The apparent doping increases by about half an order of magnitude. The same trend, although slightly less pronounced, is observed for the samples with no- and a low amount of RbF (Appendix A.6).

As a result of this increase in doping density, the width of the space charge region (SCR) is reduced from approximately 225 nm to 170 nm (estimated from C-V at zero bias), which could lead to a reduced collection of charge carriers generated deep within the absorber. This appears to be not the case for the cells investigated here. In agreement with the current gain observed in J-V, EQE measurements even show a small increase in the near infrared region (Figure 5.6).

This is believed to be caused by increased absorption for high CGI, similar to what has been previously shown [14]. Improved mobility of charge carriers, as reported for

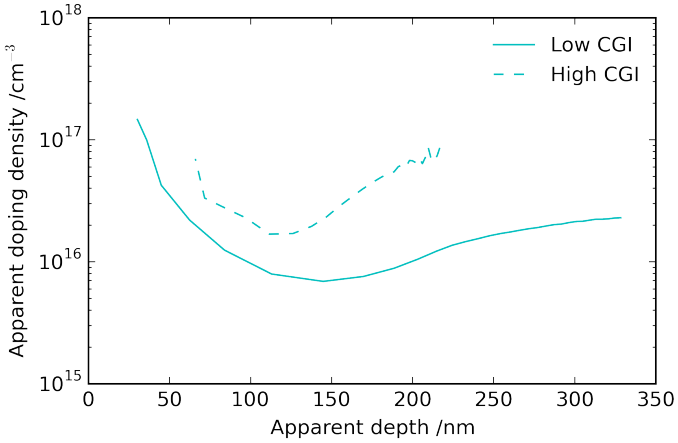


Figure 5.5: Apparent doping extracted from capacintance-voltage measurements for a cell with low (0.87) and high (0.96) Cu concentration and high RbF post treatment. An increase in apparent doping of approximately half an order of magnitude is observed.

stoichiometric absorbers in literature [160, 161], could also contribute to their efficient collection.

The Urbach energy is extracted from exponential decay fits to the EQE below the band gap. The Urbach energy is reduced from approximately 20 meV to 16 meV upon increase in Cu concentration, as shown in Figure 5.7. Above a CGI of approximately 0.95 no further reduction in the value of the Urbach energy is obtained. For the samples without RbF post treatment and with post treatment at 530 °C, as similar behavior is observed (Appendix A.7). The Urbach energy is a measurement for potential fluctuations due to potential non-uniformities and fluctuating charges at defects in the absorber. Hence this results indicate a significant reduction in defect concentration with increased Cu concentration, again independent of the RbF treatment. A similar result is observed for double-graded absorbers in our laboratory [19].

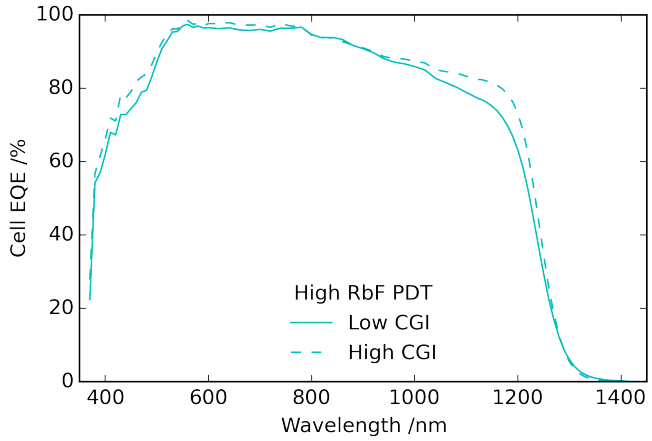


Figure 5.6: External quantum efficiency for a cell with low (0.87) and high (0.96) Cu concentration and high amount of RbF post treatment. An increased response in the near infrared region is responsible for the higher current observed in J-V measurements.

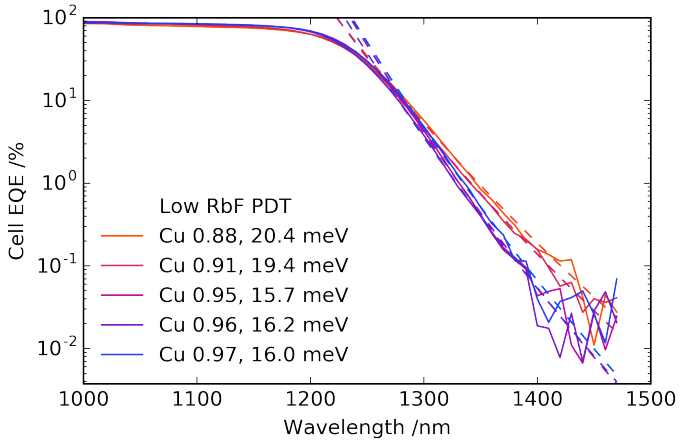


Figure 5.7: Urbach energy extracted from EQE measurements for cells with different CGI compositions and RbF treatment at 500 °C source temperature. The Urbach energy decreases for CGI up to 0.95, after which no further decrease is observed.

## 5.3 InZnO front electrical contact for improved near infrared response

Due to their extended near infrared response, narrow band gap CIS cells are more sensitive to free carrier absorption in the transparent conductive oxide front contact than CIGS. By replacing aluminum doped zinc oxide (AZO) with indium zinc oxide (IZO), the absorption losses in the near infrared region can be significantly reduced while maintaining comparable sheet resistance in the TCO (Figure 5.8).

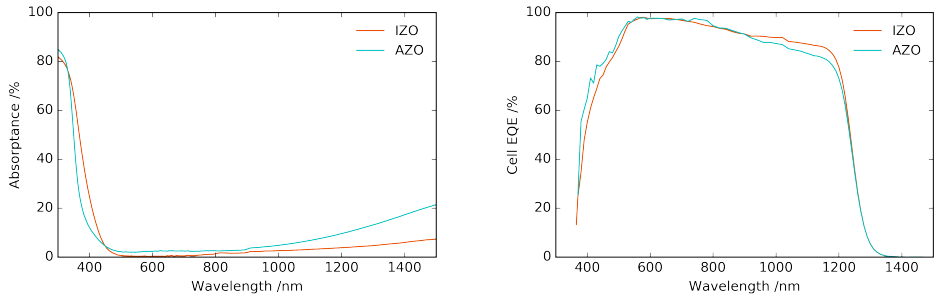


Figure 5.8: (left)Absorbtance of AZO and IZO layers on soda lime glass, both with a sheet resistance of approximately 60 Ohm/square. (right) EQE curves of the resulting solar cells. Clear gains in the near infrared are partly compensated by losses in the blue region.

IZO sputtering conditions are optimized to reach comparable sheet resistance at maximal transmission. These layers show similar majority carrier concentration (IZO 3.6*$10^{20}$ $cm^{-3}$, AZO 4.0*$10^{20}$ $cm^{-3}$), but the increased mobility (IZO 47.3 $cm^2V^{-1}s^{-1}$, AZO 14.7 $cm^2V^{-1}s^{-1}$) enables a reduction of the TCO thickness and thus absorption while maintaining the same sheet resistance. The gains in the NIR response are partially compensated by losses below 400 nm due to the reduced band gap of the IZO, resulting in a total increase of about 0.5 $mAcm^{-2}$ in current density. Besides the gain in current, cells with an IZO front contact also show a increased fill factor (Table 5.1 and Figure 5.9).

Temperature dependent J-V measurements are indicating an decrease in the blocking of injection current when changing from AZO to IZO (Figure 5.9). This is possibly based on a difference in work function between AZO and IZO and the resulting band alignment

Table 5.1: Comparison of solar cell parameters of cells with absorbers from the same deposition run with high Cu concentration (CGI 0.96) with a front contact made from AZO and IZO.

| Front contact | $V_{OC}$ (mV) | $J_{SC}$ (mAcm$^{-2}$) | FF (%) | Eff. (%) |
|---|---|---|---|---|
| AZO | 611 | 41.8 | 72.1 | 18.4 |
| IZO | 609 | 42.3 | 74.6 | 19.2 |

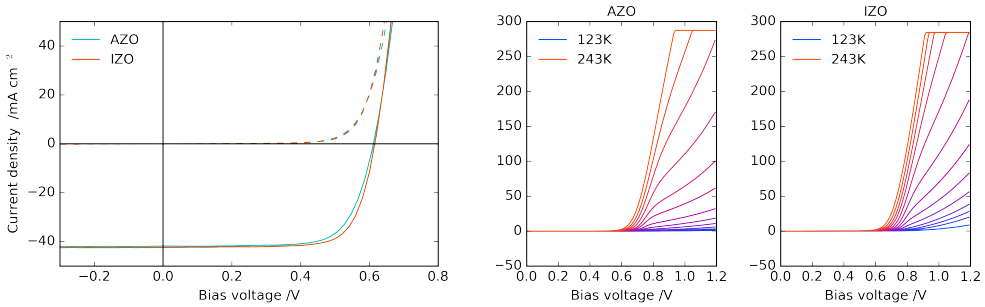


Figure 5.9: (left)J-V curves of the same absorber with AZO and IZO front contact. A increase in current and fill factor is observed. (right) Temperature dependent J-V measurements of the same cells indicate a decrease in injection barrier for the sample with IZO.

with buffer and absorber layers, but additional investigations are needed to support this assumption. Using the IZO front contact, a CGI of 0.96 and RbF post deposition treatment at 530 °C a solar cell efficiency of 19.2 % is achieved.

## 5.4 Implementation in tandem devices

As before, the suitability for tandem application is investigated by integrating those cells in 4-terminal tandem devices with a semi-transparent perovskite top-cell similar to the one described in [141]. Under the illumination transmitted through the top cell, the CIS cell delivers a current of 18.6 mAcm$^{-2}$ and a bottom-cell efficiency of 8.0% (Figure 5.10 and Table 5.2). Thus, a tandem efficiency of 24.1% is achieved in 4-terminal configuration. This is well above the efficiency of both sub-cells (+4.9% vs. CIS, +8.0% vs. perovskite).

Even better performance is reached when combining those cells with a semitranspar-

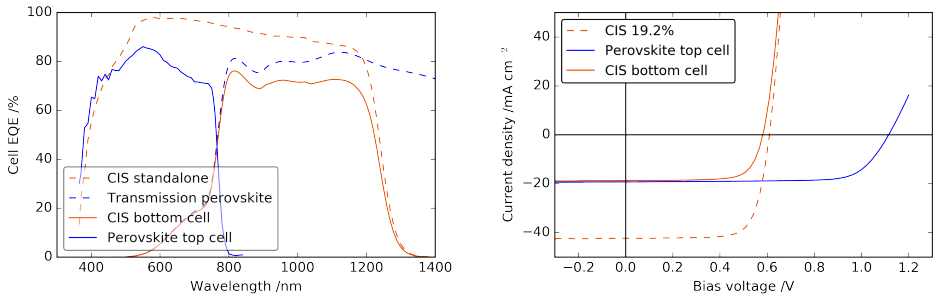


Figure 5.10: (left) EQE curves of CIS and perovskite as well as the calculated EQE of the CIS as bottom cell in 4-terminal configuration. (right) J-V curves for CIS and perovskite standalone and under illumination representing a 4-terminal configuration. For CIS bottom-cell measurements in the tandem device, illumination was realized using a combination of neutral density and long-pass filters, matching the calculated current expected from the EQE.

Table 5.2: J-V parameters of the best cell with 1.00 eV CIS absorber in standalone and 4-terminal tandem configuration with a NIR transparent perovskite top cell. For CIS bottom-cell measurements in the tandem device, illumination was realized using a combination of neutral density and long-pass filters.

| | $V_{OC}$ (mV) | $J_{SC}$ (mAcm$^{-2}$) | FF (%) | Eff. (%) |
|---|---|---|---|---|
| CIS standalone | 609 | 42.3 | 74.6 | 19.2 |
| Perovskite top-cell | 1'115 | 19.2 | 75.2 | 16.1 |
| CIS bottom-cell | 581 | 18.6 | 74.2 | 8.0 |
| Efficiency in 4-terminal tandem configuration | | | | 24.1 |

ent top-cell provided by Solliance ($V_{OC}$ 1,034 V; $J_{SC}$ 20.79 mAcm$^{-2}$; FF 79.8 %; MPP Efficiency 16.9 %). The bottom cell performance under illumination filtered by the full perovskite cell stack adds 8.1 % ($V_{OC}$ 0.565 V; $J_{SC}$ 19.4 mAcm$^{-2}$; FF 74.2 %), leading to a tandem efficiency of 25.0 %.

## 5.5 Conclusion

In this chapter it is shown that heavy alkali (RbF) PDT is effective to overcome the recombination issues in CIS based solar cells with Cu concentration close to stoichiometry. Combining almost stoichiometric Cu compositions with RbF PDT leads to enhancements

in PV-parameters well beyond the increase seen for RbF PDT alone in Chapter 4. The quality of absorber is improved with high CGI compositions, as assessed by an increase in apparent doping concentration as well as a reduction of defect density evidenced by decreases in Urbach energy. While these improvements are also present for absorbers without RbF PDT, they do not result in improved solar cell performance due to high recombination, likely at the front interface. This recombination is suppressed with the application of RbF PDT and a substantial gain in open circuit voltage is realized.

Especially the front interface recombination, previously identified as the main recombination path in absorbers with near stoichiometric composition, may be reduced by the presence of an alkali-indium-selenide phase between buffer and absorber layer. The presence of such a layer has been reported by multiple laboratories [83, 87–89]. The deposition conditions for the experiments shown here, with an In capping layer before the PDT, have been specifically designed to promote the formation of a Cu depleted surface.

Replacing the AZO front TCO with high mobility IZO further improves the PV-performance, leading to a solar cell with a $V_{OC}$ of 609 mV and a power conversion efficiency of 19.2 % for an EQE band gap of 1.00 eV. The increased spectral response of those cells in the near infrared is notably relevant for tandem applications. In combination with a 16.1 % semi-transparent perovskite top cell realized in our laboratory this enables a 4-terminal tandem device with an efficiency of 24.1 % and 25.0 % in combination with a 16.9 % top cell from Solliance.

# 6 Closing remarks and outlook

In this thesis, different methods to improve the performance of narrow band gap CIGS solar cells were investigated.

In a first step, group III element grading was used to reduce recombination throughout the absorber without increasing the optical band gap above 1.00 eV (Chapter 3). Such a narrow band gap could not be achieved with a double grading, while a single front grading led to reduced charge carrier collection, compensating any gain in voltage and resulting in no efficiency improvements. A single back grading on the other hand was exceptionally successful in increasing device performance. It is shown that this gain is a result of improved carrier collection and reduced recombination at the back contact. As a result the photovoltaic conversion efficiency for cells with a band gap of 1.00 eV increased from 15.0 % to 16.1 %.

Additional improvements for narrow gap cells may be expected with further changes in grading. The increase in $V_{OC}$ seen in the front grading experiments indicate that there is non negligible carrier recombination at the front. One possibility to avoid the blocking and collection issues shown here is to implement a front grading acting on the valence band maximum instead of the conduction band minimum (such as a S/Se grading). It should be mentioned that band gap grading may become unnecessary if passivated charge selective contacts can be found. Given the high absorption coefficient of CIS, negligible absorption takes place after approximately 1 $\mu$m of absorber. In the present devices, the rear part of the absorber layer can be seen as part of the back contact, and hence could be replaced. However, not only is no such contact known, it would also require process

compatibility with the deposition of absorber layers of high structural quality with a low density of defects and good electronic properties in terms of a large charge carrier lifetime.

The second part of this work, Chapter 4, is focused on the alkali treatment of CIS based solar cells to improve the electronic properties of the absorber layer. It is shown that Na doping in CIS is insufficient when supplied by a PDT process developed for CIGS. The implementation of an additional annealing step solved this problem and allowed to produce cells with enhanced efficiency up to 15.0 % for a CIS without band gap grading. The application of RbF post treatment to CIS, subsequently to the NaF-PDT, leads to comparable improvements as in CIGS, mainly an increase in $V_{OC}$ due to increased carrier lifetime and an improved current due to a reduced buffer layer thickness. Using the developed treatments, the efficiency of narrow band gap cells with back grading was further increased to a certified 18.0 %.

Some issues regarding the alkali treatment of CIS solar cells remain for further investigations. In the case of RbF PDT of CIS, the cells show a slow increase of performance for about a month after production, a process that can be expedited by heat-light soaking (HLS) at 80 °C. This is not observed for CIGS cells or CIS devices without RbF treatment. Additional work would be necessary to understand the mechanism and source of this effect, which may help to produce samples without the need for HLS or even further improved performance.

Another issue is the Na doping of CIS at lower temperatures. For the deposition on flexible PI a reduction of substrate temperature to 450 °C would be necessary. CIS layers grown at such low temperatures show very low doping levels (close to $10^{14}$ $cm^{-3}$), even with additional annealing after PDT. One possible way to circumvent this would be to increase the availability of sodium during the growth (i.e. by providing Na in the Mo or as precursor). However, the increased presence of alkali during the growth will influence the growth kinetics and may be detrimental [170]. Another option could be the replacement of Na with Li. Recent calculations have shown that Li may be able to act similar to Na, but the high solubility due to the low formation energy of Li based defects could allow for higher concentrations within the grains [88].

Finally the Cu to group III composition has been increased towards a more stoichiometric composition in order to reduce the defect concentration in the absorber as described in Chapter 5. The application of RbF post deposition treatment allows to circumvent the decrease in $V_{OC}$ typically observed for CIS cells with high or stoichiometric Cu concentrations. As a result, pronounced efficiency improvements are observed for cells with a higher CGI. The carrier density is increased by about half an order of magnitude when increasing the Cu/(In+Ga) ratio from 0.87 to 0.96. At the same time, the Urbach energy (as a measure for the defect concentration) reduces from 20 to 16 meV. The resulting cells show a very high $V_{OC}$ of 609 mV and, when combined with a high mobility TCO, reach a cell performance of 19.2 % while still retaining the band gap at 1.00 eV.

The continuation of this work could include characterization of the passivated defects, concentration and type (vacancy, antisite, defect complex), to better understand the source of the improvements. This could be done by low temperature photo-luminescence or positron annihilation spectroscopy. A closer look at the front interface could help to identify ways to process absorbers even closer to stoichiometry. While this is expected to further improve the absorber quality, such devices still suffer from a decreased in $V_{OC}$ and shunting due to the presence of $Cu_xSe$ phases, even with RbF PDT.

## 6.1 Tandem devices

As described in the introduction, one of the main drivers for the interest in narrow band gap CIS is their application as bottom cell in tandem devices. Throughout this work, many such devices have been produced with perovskite top cells from our own lab and sometimes in collaboration with other labs. This effort has led to a steady increase in record CIGS/perovskite tandem efficiencies, many of which were achieved with our involvement (Figure 6.1). The early efficiency increase is mainly driven by improvements in the perovskite top cell, with readily available CIGS bottom cells optimized for single cell performance. Looking at some of the recent records however, it becomes clear that adjustment of the bottom cell band gap is important even in 4-terminal configuration.

The 24.6 % and the 25.0 % tandems were both achieved using perovskite top cells with identical process but different bottom cells. While the 24.6 % uses a regular high efficiency CIGS from ZSW (~1.15 eV band gap, $\eta$ well above 21 %), the 25.0 % record was achieved with a 18.7 % narrow band gab cell out of this work, highlighting the advantage gained with using a reduced band gap (1.0 eV).

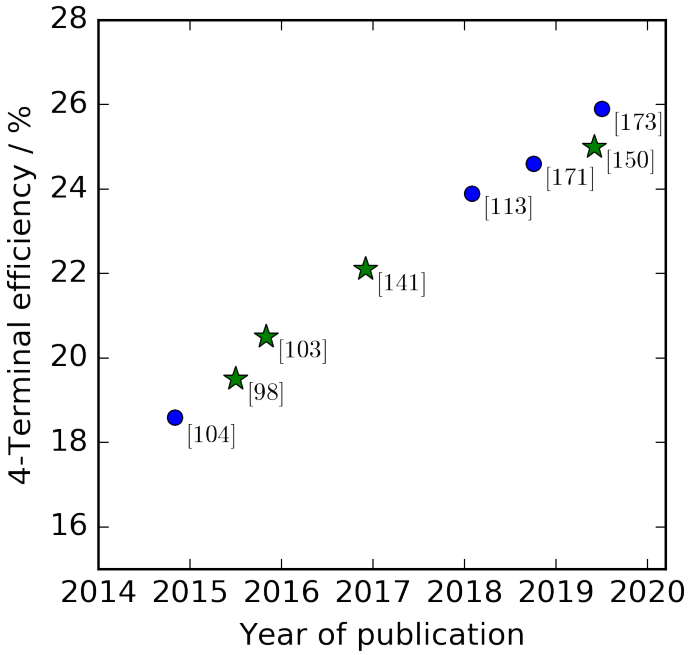


Figure 6.1: Record efficiency for 4-terminal CIGS/Perovskite tandem devices as a function of time. The devices with contribution from our lab are marked with a star. Sources for the performance data are given in references [98, 103, 104, 113, 141, 150, 171, 172]. Adapted from [150]

An important topic for the continuation of this work will be to evaluate the advantages and disadvantages of 2- and 4-terminal tandem devices. 2-terminal, monolithic devices have the advantage of reduced material use and parasitic absorption. For Perovskite/c-Si tandem devices this has already lead to an efficiency advantage above the 4-terminal devices, with current records being at 28.0 % for 2-terminal and 27.1 % for 4-terminal devices [173, 174]. Due to the better band gap fit even higher gains could be expected for CIS. Opposed to these gains stands the increased dependence on current matching. While a certain amount of mismatch may be tolerable by the device, it will lead to sub-

optimal use of the spectrum. A device that is current matched at AM1.5G will not be matched at a different spectrum, leading to losses based on the location of operation an to a certain extend even time of the year or day. Recent energy yield and levelized cost of electricity (LCOE) calculations have shown that under real conditions 4-terminal devices could outperform the monolithic option based on the changing spectrum [175,176]. This becomes even more important when taking different temperature coefficients and degradation behavior into account. Another important issue for 2-terminal devices is the roughness of the CIGS bottom cell. While 2-terminal devices with perovskite on top of structured Si have been shown successfully, the surface of CIGS devices contains steep ledges and crevices, leading to shunting in the thin perovskite top cell. To circumvent these issues, a flattening of the CIGS surface or an adaptation of the perovskite deposition process will be necessary.

Because of this reasons it is the opinion of the author that, at the current state, the 4-terminal approach is more promising to deliver highly efficient, all thin-film tandem devices.

Independent of the chosen path, tandem cells provide a way to outperform the single junction devices reaching their thermodynamic limits. The work presented in this thesis lays a foundation to do so using all thin-film technology with the potential for low production cost and highest sustainability!

# 7 Acknowledgments

My first thanks go to Prof. Ayodhya N. Tiwari, head of the Laboratories for Thin Films and Photovoltaics, for giving me the chance to conduct this work and for his support and advice during my thesis. I am very grateful to Dr. Stephan Bücheler for his supportive and encouraging supervision of my work. I would especially thank them for, together with Dr. Yaroslav Romanyuk and lately Dr. Romain Carron, building up the wonderful team of researchers in our lab that does not only allow to achieve first class results, but also makes working here a rewarding and fun experience.

I am much obliged to Prof. Dr. Susanne Siebentritt from the PV Lab at the University of Luxembourg and Prof. Dr. Jürg Leuthold from d-ITET at ETH Zürich for agreeing to be examiners of this thesis.

Of course I would like to thank all members of the Thin Film and Photovoltaics group at Empa, former and present, for a great time and superb collaborations. Special thanks go to Dr. Timo Jäger, who introduced me to the group and the field of high vacuum processing, Dr. Patrick Reinhard who helped me getting started with CIGS and Dr. Shiro Nishiwaki, who not only trained me on the growth process but also taught me not to needlessly over-complicate an experiment. Thanks to the CIGS team for many insightful discussions and collaborations. Thanks to Dr. Enrico Avancini for all the SIMS measurements, and to the characterization team, Dr. Benjamin Bissig, Dr. Thomas Weiss and Dr. Mario Ochoa for all their support and teaching. I'd like to thank Dr. Johannes Löckinger and Dr. Stefan Haas for hours of scientific and non-scientific discussions. Thanks also go to my colleagues from the perovskite group, without the cells of Dr. Fan Fu and Dr. Stefano Pisoni the tandem devices would never have been realized.

Thank you to Till Coester and David Stalder for the technical support and for letting me use the workshop whenever necessary. And a big thanks all other members of our group for a great time, be it at work or of work at group activities and game nights.

Last but not least I would like to thank my family for their support, without which none of this would ever have been possible.

# Curriculum Vitae

**Thomas Feurer**

| | |
|---|---|
| Date of birth: | 11.11.1983 |
| Place of birth: | Chur, Switzerland |
| Nationality: | Swiss |


## Experience

| | |
|---|---|
| 09/2014 - 10/2019 | PhD student, Laboratory for Thin Films and Photovoltaics at Empa - Swiss Federal Laboratories for Materials Science and Technology, Dübendorf, Switzerland. |
| 08/2008 - 08/2009 | Procurement manager R&D, EMS-Chemie AG, Domat/Ems, Switzerland |
| 01/2007 - 08/2008 | R&D project manager, EMS-Chemie AG, Domat/Ems, Switzerland |
| 08/2002 - 12/2006 | Laboratory Assistant, EMS-Chemie AG, Domat/Ems, Switzerland |

## Education

| | |
|---|---|
| 2009 - 2014 | Studies of physics at ETH Zurich, Switzerland; graduated as MSc ETH Physics. |
| 2002 - 2006 | Studies of chemistry at HTW Chur, Switzerland; graduated as Dipl. Ing. FH, PuA Chemie. |

# 8 List of publications

Feurer Thomas, Fan Fu, Romain Carron, Galo Torres Sevilla, Fan Fu, Stefano Pisoni, Yaroslav E. Romanyuk, Stephan Buecheler, and Ayodhya N. Tiwari. 2019. "Efficiency Improvement of Near-Stoichiometric CuInSe2 Solar Cells for Application in Tandem Devices". Advanced Energy Materials accepted
https://doi.org/10.1002/aenm.201901428

Feurer Thomas, Fan Fu, Thomas Paul Weiss, Enrico Avancini, Johannes Löckinger, Stephan Buecheler, and Ayodhya N. Tiwari. 2019. "RbF post deposition treatment for narrow bandgap Cu(In,Ga)Se2 solar cells". Thin Solid Films 670 (January): 34-40.
https://doi.org/10.1016/j.tsf.2018.12.003

Feurer Thomas, Patrick Reinhard, Enrico Avancini, Benjamin Bissig, Johannes Löckinger, Peter Fuchs, Romain Carron, Thomas Paul Weiss, Julian Perrenoud, Stephan Stutterheim, Stephan Buecheler, and Ayodhya N. Tiwari. 2016. "Progress in thin film CIGS photovoltaics - Research and development, manufacturing, and applications". Progress in Photovoltaics: Research and Applications 25 (7): 645-67.
https://doi.org/10.1002/pip.2811

Feurer Thomas, Benjamin Bissig, Thomas P. Weiss, Romain Carron, Enrico Avancini, Johannes Löckinger, Stephan Buecheler, and Ayodhya N. Tiwari. 2018. "Single-graded CIGS with narrow bandgap for tandem solar cells". Science and Technology of Advanced Materials 19 (1): 263-70.
https://doi.org/10.1080/14686996.2018.1444317

Avancini, Enrico, Romain Carron, Benjamin Bissig, Patrick Reinhard, Roberto Menozzi, Giovanna Sozzi, Simone Di Napoli, Thomas Feurer, Shiro Nishiwaki, Stephan Buecheler, and Ayodhya N. Tiwari. 2017. "Impact of Compositional Grading and Overall Cu Deficiency on the Near-Infrared Response in Cu(In, Ga)Se2 Solar Cells". Progress in Photovoltaics: Research and Applications 25 (3): 233-41.
https://doi.org/10.1002/pip.2850

Bissig, Benjamin, Carlos Guerra-Nunez, Romain Carron, Shiro Nishiwaki, Fabio La Mattina, Fabian Pianezzi, Paolo A. Losio, Enrico Avancini, Patrick Reinhard, Stefan G. Haass, Martina Lingg, Thomas Feurer, Ivo Utke Stephan Buecheler and Ayodhya N. Tiwari. 2016. "Surface Passivation for Reliable Measurement of Bulk Electronic Properties of Heterojunction Devices". Small 12 (38): 5339-46.
https://doi.org/10.1002/smll.201601575

Bissig, Benjamin, Romain Carron, Lukas Greuter, Shiro Nishiwaki, Enrico Avancini, Christian Andres, Thomas Feurer, Stephan Buecheler, and Ayodhya N. Tiwari. 2018. "Novel Back Contact Reflector for High Efficiency and Double-Graded Cu(In,Ga)Se2 Thin-Film Solar Cells". Progress in Photovoltaics: Research and Applications 26 (11): 894-900.
https://doi.org/10.1002/pip.3029

Carron, Romain, Christian Andres, Enrico Avancini, Thomas Feurer, Shiro Nishiwaki, Stefano Pisoni, Fan Fu, Martina Lingg, Yaroslav E. Romanyuk, Stephan Buecheler, and Ayodhya N. Tiwari. 2019. "Bandgap of thin film solar cell absorbers: A comparison of various determination methods". Thin Solid Films 669 (January): 482-86.
https://doi.org/10.1016/j.tsf.2018.11.017

Carron, Romain, Enrico Avancini, Thomas Feurer, Benjamin Bissig, Paolo A. Losio, Renato Figi, Claudia Schreiner, Melanie BÃ¼rki, Emilie Bourgeois, Zdenek Remes, Milos Nesladek, Stephan Buecheler, and Ayodhya N. Tiwari. 2018. "Refractive indices of layers and optical simulations of Cu(In,Ga)Se2 solar cells". Science and Technology of Advanced

Materials 19 (1): 396-410.
https://doi.org/10.1080/14686996.2018.1458579

Carron, Romain, Shiro Nishiwaki, Thomas Feurer, Ramis Hertwig, Enrico Avancini, Johannes Löckinger, Shih-Chi Yang, Stephan Buecheler, and Ayodhya N. Tiwari. 2019. "Advanced Alkali Treatments for High-Efficiency Cu(In,Ga)Se2 Solar Cells on Flexible Substrates". Advanced Energy Materials 9 (24): 1900408.
https://doi.org/10.1002/aenm.201900408

Fu, Fan, Thomas Feurer, Thomas Paul Weiss, Stefano Pisoni, Enrico Avancini, Christian Andres, Stephan Buecheler, and Ayodhya N. Tiwari. 2016. "High-Efficiency Inverted Semi-Transparent Planar Perovskite Solar Cells in Substrate Configuration". Nature Energy 2 (December): 16190.
https://doi.org/10.1038/nenergy.2016.190

Fu, Fan, Lukas Kranz, Songhak Yoon, Johannes Löckinger, Timo JÃ¤ger, Julian Perrenoud, Thomas Feurer, Christina Gretener, Stephan Buecheler, and Ayodhya N. Tiwari. 2015. "Controlled Growth of PbI2 Nanoplates for Rapid Preparation of CH3NH3PbI3 in Planar Perovskite Solar Cells". Physica Status Solidi (a) 212 (12): 2708-2717.
https://doi.org/10.1002/pssa.201532442

Fu, Fan, Stefano Pisoni, Thomas P. Weiss, Thomas Feurer, Aneliia WÃ¤ckerlin, Peter Fuchs, Shiro Nishiwaki, Lukas Zortea, Ayodhya N. Tiwari, and Stephan Buecheler. 2018. "Compositionally Graded Absorber for Efficient and Stable Near-Infrared-Transparent Perovskite Solar Cells". Advanced Science 5 (3): 1700675.
https://doi.org/10.1002/advs.201700675

N. Filippin, Alejandro, Michael Rawlence, Aneliia WÃ¤ckerlin, Thomas Feurer, Tanja Zänd, Kostiantyn Kravchyk, Maksym V. Kovalenko, Yaroslav E. Romanyuk, Ayodhya N. Tiwari, and Stephan Buecheler. 2017. "Chromium Nitride as a Stable Cathode Current Collector for All-Solid-State Thin Film Li-Ion Batteries". RSC Advances 7 (43): 26960-67.

https://doi.org/10.1039/C7RA03580B

Kranz, Lukas, Antonio Abate, Thomas Feurer, Fan Fu, Enrico Avancini, Johannes Löckinger, Patrick Reinhard, Shaik M. Zakeeruddin, Michael Grätzel, Stephan Buecheler, and Ayodhya N. Tiwari. 2015. "High-Efficiency Polycrystalline Thin Film Tandem Solar Cells". The Journal of Physical Chemistry Letters 6 (14): 2676-81.
https://doi.org/10.1021/acs.jpclett.5b01108

Fu, Fan, Thomas Feurer, Timo JÃ¤ger, Enrico Avancini, Benjamin Bissig, Songhak Yoon, Stephan Buecheler, and Ayodhya N. Tiwari. 2015. "Low-Temperature-Processed Efficient Semi-Transparent Planar Perovskite Solar Cells for Bifacial and Tandem Applications". Nature Communications 6 (November): 8932.
https://doi.org/10.1038/ncomms9932

Mantilla-Perez, Paola, Thomas Feurer, Juan-Pablo Correa-Baena, Quan Liu, Silvia Colodrero, Johann Toudert, Michael Saliba, Stephan Buecheler, Anders Hagfeld, Ayodhya N. Tiwari, and Jordi Martorell. 2017. "Monolithic CIGS-Perovskite Tandem Cell for Optimal Light Harvesting without Current Matching". ACS Photonics 4 (4): 861-67.
https://doi.org/10.1021/acsphotonics.6b00929

Nishiwaki, Shiro, Thomas Feurer, Benjamin Bissig, Enrico Avancini, Romain Carron, Stephan Buecheler, and Ayodhya N. Tiwari. 2017. "Precise Se-flux control and its effect on Cu(In,Ga)Se2 absorber layer deposited at low substrate temperature by multi stage co-evaporation". Thin Solid Films, E-MRS 2016 Spring Meeting, Symposium V, Thin-Film Chalcogenide Photovoltaic Materials, 633 (July): 18-22.
https://doi.org/10.1016/j.tsf.2016.10.057

Pisoni, Stefano, Romain Carron, Thierry Moser, Thomas Feurer, Fan Fu, Shiro Nishiwaki, Ayodhya N. Tiwari, and Stephan Buecheler. 2018. "Tailored Lead Iodide Growth for Efficient Flexible Perovskite Solar Cells and Thin-Film Tandem Devices". NPG Asia Materials 10 (11): 1076.

https://doi.org/10.1038/s41427-018-0099-1

Pisoni, Stefano, Fan Fu, Thomas Feurer, Mohammed Makha, Benjamin Bissig, Shiro Nishiwaki, Ayodhya N. Tiwari, and Stephan Buecheler. 2017. "Flexible NIR-Transparent Perovskite Solar Cells for All-Thin-Film Tandem Photovoltaic Devices". Journal of Materials Chemistry A 5 (26): 13639-47.
https://doi.org/10.1039/C7TA04225F

Uhl, Alexander R., Adharsh Rajagopal, James A. Clark, Anna Murray, Thomas Feurer, Stephan Buecheler, Alex K.-Y. Jen, and Hugh W. Hillhouse. 2018. "Solution-Processed Low-Bandgap CuIn(S,Se)2 Absorbers for High-Efficiency Single-Junction and Monolithic Chalcopyrite-Perovskite Tandem Solar Cells". Advanced Energy Materials 8 (27): 1801254.
https://doi.org/10.1002/aenm.201801254

Weiss, Thomas P., Benjamin Bissig, Thomas Feurer, Romain Carron, Stephan Buecheler, and Ayodhya N. Tiwari. 2019. "Bulk and Surface Recombination Properties in Thin Film Semiconductors with Different Surface Treatments from Time-Resolved Photoluminescence Measurements". Scientific Reports 9 (1): 5385.
https://doi.org/10.1038/s41598-019-41716-x

Zortea, Lucas, Shiro Nishiwaki, Thomas Paul Weiss, Stefan Haass, Julian Perrenoud, Lukas Greuter, Thomas Feurer, Ganesan Palaniswamy, Stephan Buecheler, and Ayodhya N. Tiwari. 2018. "Cu(In,Ga)Se2 solar cells on low cost mild steel substrates". Solar Energy, Recent Progress in Photovoltaics, Part 1, 175 (November): 25-30.
https://doi.org/10.1016/j.solener.2017.12.057

## Conference contributions

| | | | |
|---|---|---|---|
| EU-PVSEC 2015 | Hamburg DE | Oral | Low bandgap Cu(In,Ga)$Se_2$ solar cells applied in tandem devices with perovskite top cells |
| E-MRS Spring Meeting 2016 | Strasbourg FR | Poster | Low band-gap Cu(In,$GaS)_2$ solar cells for all thin film tandem devices with perovskite top cells |
| MRS Spring Meeting 2017 | Phoenix,AZ US | Poster | Low Band Gap Cu(In,Ga)$Se_2$ Absorber Layers for Perovskite/CIGS Tandem Solar Cells |
| E-MRS Spring Meeting 2018 | Lille FR | Oral | Narrow bandgap Cu(In,Ga)$Se_2$ solar cells for CIGS/Perovskite tandem devices |
| EU-PVSEC 2018 | Brussels BE | Oral | Narrow bandgap Cu(In,Ga)$Se_2$ solar cells for CIGS/Perovskite tandem devices |
| CSPV 2018 | Xi'An CN | Invited | Narrow Bandgap Cu(In,Ga)$Se_2$ Solar Cells for Tandem Application |
| MRS Spring Meeting 2019 | Phoenix,AZ US | Oral | Narrow Bandgap Cu(In,Ga)$Se_2$ solar cells for Tandem Application |
| IW-CIGSTECH 2019 | Paris FR | Invited | CIGS for tandem solar cells |

## Awards

| | |
|---|---|
| E-MRS Spring Meeting 2016 | Best Poster Award |
| Empa PHD Student's Symposium 2017 | Poster Presentation Award |
| EU-PVSEC 2018 | EU PVSEC Student Award 2018 |

# Appendices

# A Figures

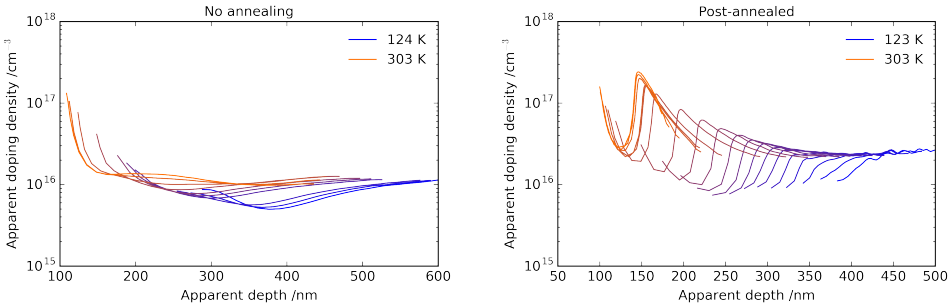


Figure A.1: Improvements in the apparent doping density of CIS solar cells by 20 minutes of additional in-situ annealing after PDT

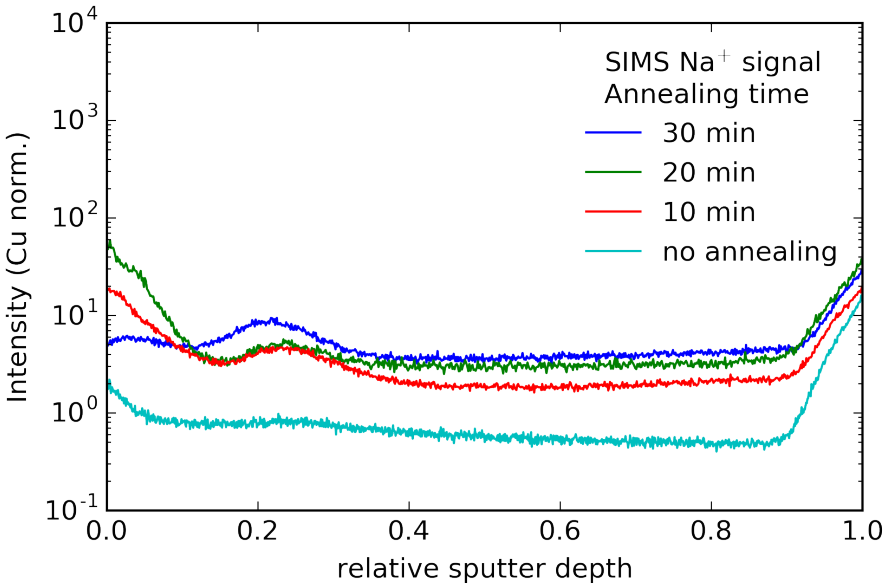


Figure A.2: Sodium distribution within the absorber for different in-situ annealing times. To compare samples, the signal has been normalized by Cu. This slightly exaggerates the increase in front of the absorber, as Cu is depleted on the surface of the absorber, but the general shape is representative for the original measurement.

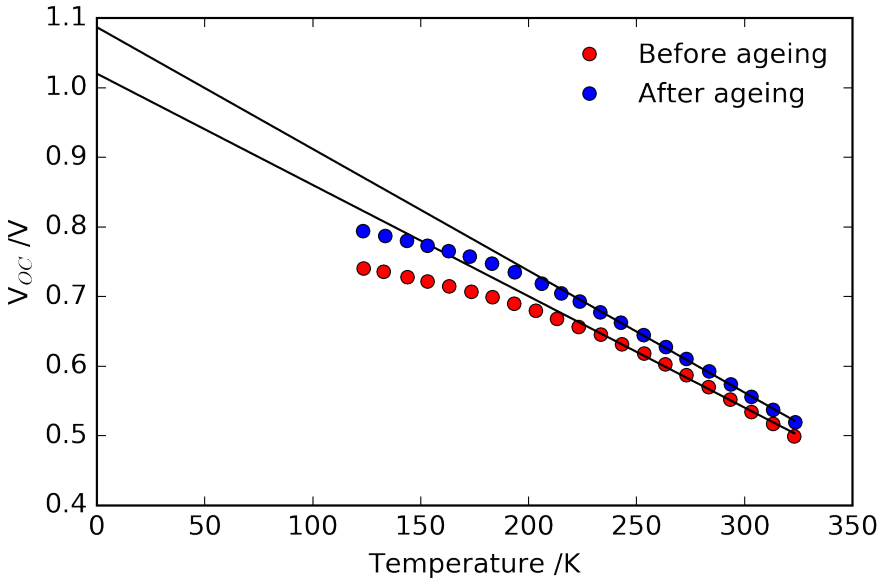


Figure A.3: Temperature dependence of the $V_{OC}$ for solar cells made from CIS based absorbers with RbF post treatment before and after aging as described in chapter 4. The difference in activation energy indicates a change in dominant recombination path. Please note that the higher activation energy for the aged sample lies above the band gap of the main CIS absorber. The difference may be explained by changes in the temperature-dependent thermal velocity $v_{th}$ and effective density of states $N_{c,v}$ as described in literature [140]

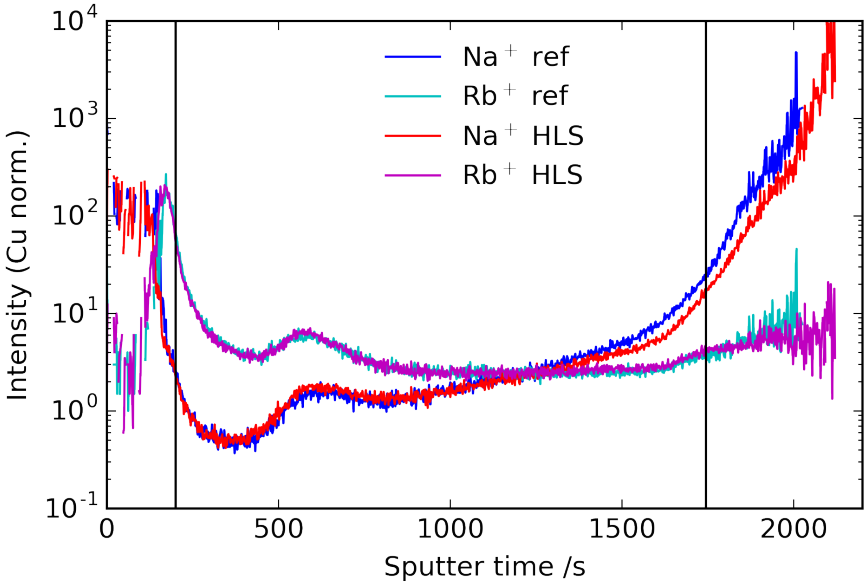


Figure A.4: Alkali profiles for a RbF treated cell before and after heat-light soaking. Both profiles are similar. Vertical lines indicate the boundaries of the absorber. Only a minor difference in the Na signal is observed, most likely within the original spread in the sample.

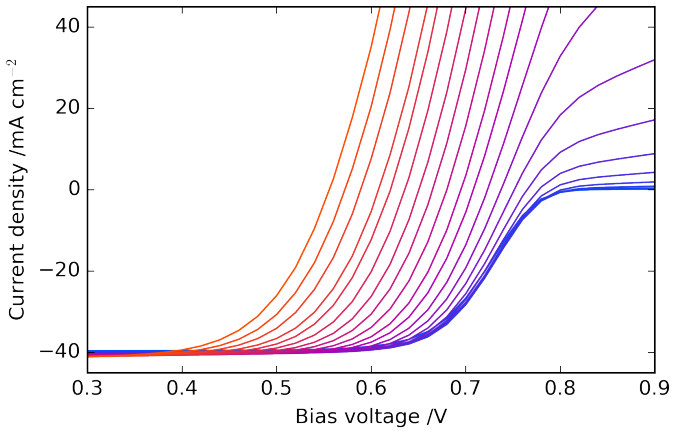


Figure A.5: Temperature dependent J-V curves for CIS absorbers with high CGI (0.96) and RbF PDT at high source temperature (530 °C). The blocking observed for samples with low Cu content (See Figure 4.10) and similar RbF rates does not appear yet.

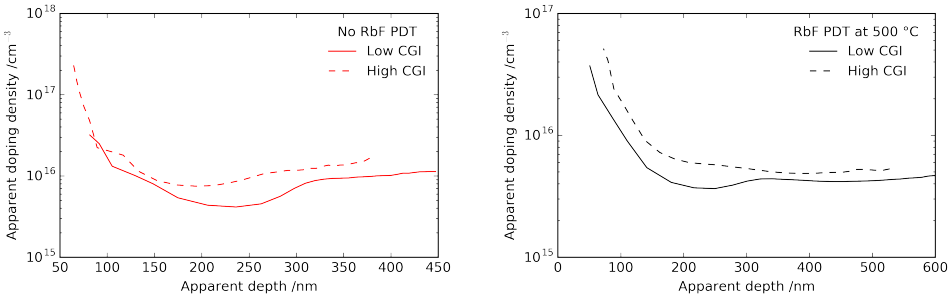


Figure A.6: Apparent doping density of CIS with increased Cu content for samples with no RbF PDT (left) and RbF PDT at 500 °C source temperature (right). The doping seems to increase with higher Cu content independent of the applied post treatment.

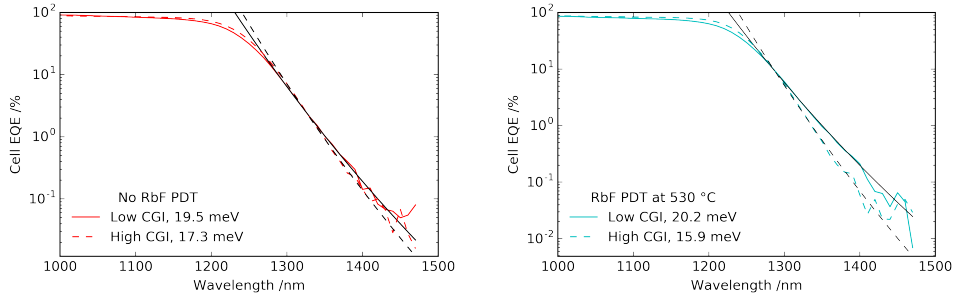


Figure A.7: Urbach energy extracted from EQE of CIS with increased Cu content for samples with no RbF PDT (left) and RbF PDT at 530 °C source temperature. In both cases the Urbach energy decreases with increasing Cu content.

# B Tables

Table B.1: [Cu]/([In]+[Ga]) ratio as measured by XRF compared to inductively coupled plasma optical emission spectrometry (ICP-OES) control measurements. The offset found is within ±0.01

| | Base series | High RbF | | |
|---|---|---|---|---|
| XRF | 0.88 | 0.95 | 0.96 | 0.96 |
| ICP-OES | 0.87 | 0.95 | 0.96 | 0.95 |

# C Certifications

**Fraunhofer ISE CalLab PV Cells**

**Heidenhofstr.2**

**79110 Freiburg**

Fraunhofer ISE

CalLab PV Cells

# Werkskalibrierschein

*Proprietary calibration report*

1003015EMP0118

| | |
|---|---|
| Gegenstand<br>*Object* | **Solar Cell** |
| Hersteller<br>*Manufacturer* | **EMPA** |
| Typ<br>*Type* | **CIS** |
| Fabrikat/Serien-Nr.<br>*Serial number* | **EMP003 / Oct1374_f3** |
| Auftraggeber<br>*Customer* | **Empa**<br>**Abt. für Dünnfilme und Photovoltaik (Abt 207)**<br>**Überlandstr. 129**<br>**CH-8600 Dübendorf, Switzerland** |
| Auftragsnummer<br>*Order No.* | **015EMP0118** |
| Anzahl der Seiten<br>*Number of pages* | **9** |
| Datum der Kalibrierung<br>*Date of calibration* | **24.01.2018** |

Kalibrierscheine ohne Unterschrift haben keine Gültigkeit. *Calibration certificates without signature are not valid.*

| Datum<br>*Date* | Leiter des Kalibrierlaboratoriums<br>*Head of the calibration laboratory* | Bearbeiter<br>*Person in charge* |
|---|---|---|
| 25.01.2018 | *Wilhelm Warta* | *Astrid Semeraro* |

## 1. Beschreibung des Kalibriergegenstandes

*Description of the calibrated object*

Das Messobjekt ist eine Solarzelle, Typ: CIS auf einem Glasssubstrat. Die Stabilität der Solarzelle wurde nicht untersucht.
*The device under test is a CIS solar cell on a glass subsstrate. The temporal stability of the solar cell performance was not controlled.*

## 2. Messverfahren

*Measurement procedure*

Die Kalibrierung des Kalibrierobjektes wird gemäß /1/ mit einem DC-Sonnensimulator Klasse A nach /6/ unter Standardtestbedingungen (STC) durchgeführt. Die Einstrahlung wird mit Hilfe einer Monitorzelle während der gesamten Messdauer aufgenommen und deren Schwankungen bezüglich der Messung korrigiert. Die Divergenz der Randstrahlen ist < 8°. Die Solarzelle wird auf einem Vakuumprobentisch thermisch stabilisiert.
*The calibration of the test sample was performed at Standard Testing Conditions (STC) in accordance with /1/ under irradiation with a steady-state class A solar simulator according to /6/. The irradiance is controlled with a monitor cell during the measurement in order to correct fluctuations. The divergence of the peripheral beams is < 8°. The solar cell is kept at a constant temperature on a vacuum chuck.*

Rückführung der Referenzsolarzelle/*Traceability of the reference solar cell*:

| Identitäts-Nr. / *Identity-Nr.* : | Kalibrierschein-Nr./ *Certificate-Nr.* : | Rückführung/ *Traceability* : |
|---|---|---|
| 041-2015 | 47003-PTB-16 | PTB |

Das Messergebnis für den Kurzschlussstrom enthält eine Korrektur der spektralen Fehlanpassung (Mismatch), die durch die Abweichung der spektralen Verteilung des Klasse A Simulators vom Standard-Spektrum AM1.5G /3/ in Kombination mit den verschiedenen spektralen Empfindlichkeiten von Referenzzelle und Messobjekt entsteht /4/.
Dazu wurde die spektrale Verteilung der Bestrahlung (Sonnensimulator) mit einem Spektralradiometer und die spektrale Empfindlichkeit des Messobjektes mit einem Filtermonochromator /5/ gemessen (s. Kalibrierschein Nr: 90003015EMP0118).
*The spectral mismatch - caused by the deviation of the simulator spectrum from the standard spectrum AM1.5G /3/ in combination with the difference between the spectral response of the reference cell andthat of the device under test (DUT) – is calculated according to /4/ and corrected.*
*For the spectral mismatch correction the spectral distribution of the solar simulator is measured with a spectroradiometer, the spectral response of the DUT is measured with a filter monochromator according to /5/ (cf. Calibration Mark: 90003015EMP0118).*

Fraunhofer ISE

CalLab PV Cells



Die Rückführung der Spektralmessung auf SI-Einheiten erfolgte über den Vergleich mit einer Standardlampe.
*The traceability of the measurement of the spectral distribution to SI-Units is achieved using a standard lamp for the calibration of the spectroradiometer.*

| Identitäts-Nr. / *Identity-Nr.* : | Kalibrierschein-Nr./ *Certificate-Nr.* : | Rückführung/ *Traceability* : |
|---|---|---|
| BN-9101-451 | 40002-14-PTB | PTB |

## 3. Messbedingungen

*Measurement conditions*

Standardtestbedingungen (STC) / *Standard Testing Conditions (STC)* :

| | | |
|---|---|---|
| Absolute Bestrahlungsstärke / *Total irradiance* : | 1000 | W/m² |
| Temperatur des Messobjektes / *Temperature of the DUT* : | 25 | °C |
| Spektrale Bestrahlungsstärke / *Spectral irradiance distribution* : | AM1.5G Ed.2 (2008) | |

Die Messung der IV-Kennlinie (Strom-Spannungs-Kennlinie) des Messobjektes erfolgt mit Hilfe eines Vierquadranten-Netzteiles und eines Kalibrierwiderstandes.
*The measurement of the IV-curve is performed with a 4-quadrant power amplifier and a calibration resistor.*

## 4. Messergebnis

*Measurement results*

Mismatch-Faktor / *Mismatch factor* : = 1.0213

(Spektral-Korrektur / *spectral correction* )

Fläche / Area (da)[1]: = ( 0.5530 ± 0.0034 ) cm²

[1] : *(t) = total area, (ap) = aperture area, (da) = designated illumination area /7/*

Kennlinienparameter des Messobjektes unter Standardtestbedingungen (STC) / *IV-curve parameter under Standard Testing Conditions (STC)* :

| | | | | | |
|---|---|---|---|---|---|
| $V_{OC}$ | = ( | 595.2 | ± | 2.0 | ) mV |
| $I_{SC}$ (Ed.2 - 2008)/3/ | = ( | 23.21 | ± | 0.44 | ) mA |
| $J_{SC}$ | = ( | 41.96 | ± | 0.80 | ) mA/cm² |
| $I_{MPP}$ | = | 20.77 | | | mA |
| $V_{MPP}$ | = | 478.4 | | | mV |
| $P_{MPP}$ | = ( | 9.94 | ± | 0.20 | ) mW |
| *FF* | = ( | 71.93 | ± | 0.47 | ) % |
| $\eta$ | = ( | 17.97 | ± | 0.36 | ) % |

Angegeben ist jeweils die erweiterte Messunsicherheit, die sich aus der Standardmessunsicherheit durch Multiplikation mit dem Faktor *k*=2 ergibt. Sie wurde gemäß dem "Guide to the expression of Uncertainty in Measurement" ermittelt. Sie entspricht bei einer Normalverteilung der Abweichungen vom Messwert einer Überdeckungswahrscheinlichkeit von 95%.
*The expanded measurement uncertainty resulting from the standard measurement uncertainty multiplied with a factor k=2 is specified. The calculation was carried out according to the "Guide to the expression of Uncertainty in Measurement". The value corresponds to a Gaussian distribution denoting the deviations of the measurement value within a probability of 95%.*

## 5. Zusatzinformationen

*Additional information*

Nur zum Vergleich / *For comparison purposes* :

Berechneter Wert nach bisherigem Normspektrum / *Calculated value according to previous standard spectrum* :

$I_{sc}$ (Ed.1 - 1989) /2/ = ( 23.02 ± 0.44 ) A

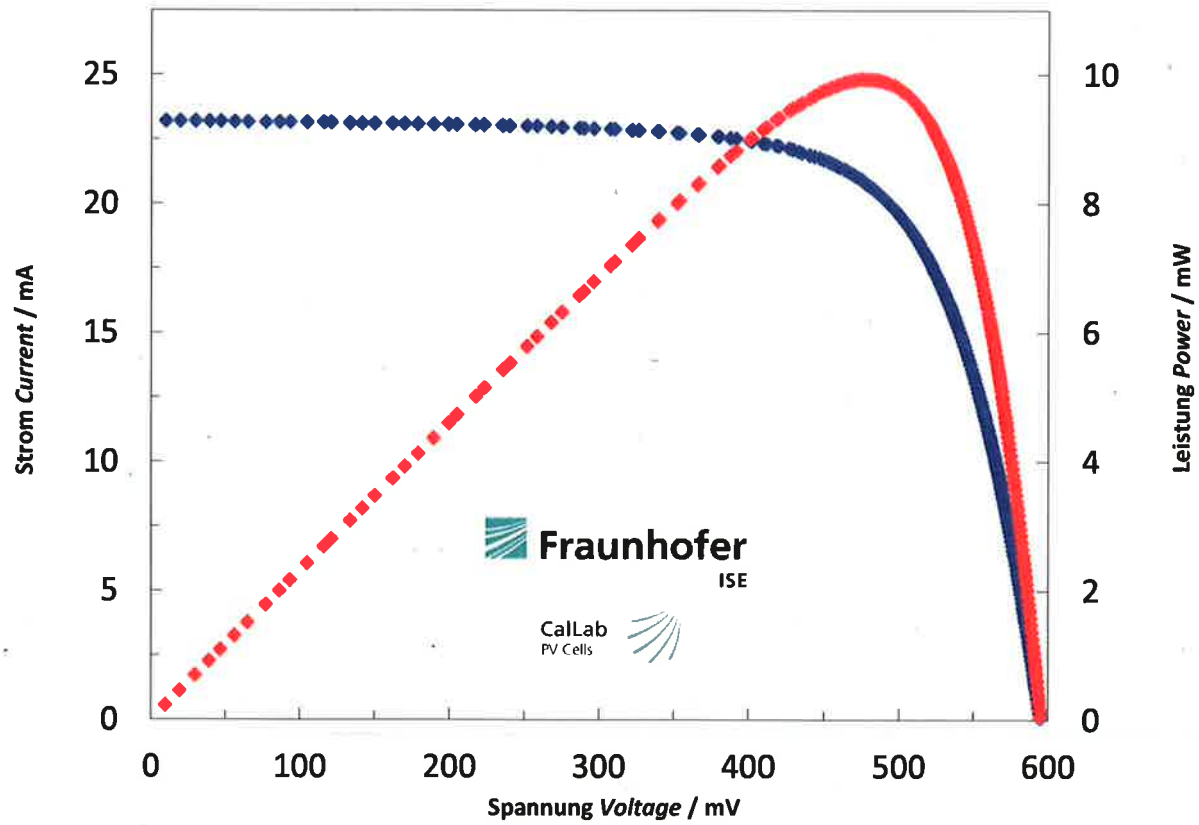

Fraunhofer ISE

1003015EMP0118

CalLab
PV Cells

| Spannung *Voltage* / mV | Strom *Current* / mA | Leistung *Power* / mW |
|---|---|---|
| -96.46 | 23.23 | -2.24 |
| -88.37 | 23.23 | -2.05 |
| -75.08 | 23.24 | -1.75 |
| -67.72 | 23.24 | -1.57 |
| -57.04 | 23.24 | -1.33 |
| -48.36 | 23.23 | -1.12 |
| -37.71 | 23.22 | -0.88 |
| -30.65 | 23.21 | -0.71 |
| -20.02 | 23.20 | -0.46 |
| -8.49 | 23.20 | -0.20 |
| -0.81 | 23.21 | -0.02 |
| 9.89 | 23.20 | 0.23 |
| 19.64 | 23.20 | 0.46 |
| 29.72 | 23.20 | 0.69 |
| 39.18 | 23.19 | 0.91 |
| 46.80 | 23.19 | 1.09 |
| 56.18 | 23.17 | 1.30 |
| 65.07 | 23.16 | 1.51 |
| 76.99 | 23.16 | 1.78 |
| 86.26 | 23.16 | 2.00 |
| 93.28 | 23.16 | 2.16 |
| 104.67 | 23.16 | 2.42 |
| 115.98 | 23.15 | 2.68 |
| 120.87 | 23.14 | 2.80 |
| 133.39 | 23.12 | 3.08 |
| 141.52 | 23.11 | 3.27 |
| 149.99 | 23.11 | 3.47 |
| 161.56 | 23.11 | 3.73 |
| 169.54 | 23.10 | 3.92 |
| 178.32 | 23.08 | 4.12 |
| 188.99 | 23.07 | 4.36 |
| 198.83 | 23.07 | 4.59 |
| 204.42 | 23.06 | 4.71 |
| 216.79 | 23.05 | 5.00 |
| 222.61 | 23.04 | 5.13 |
| 234.97 | 23.02 | 5.41 |
| 239.56 | 23.01 | 5.51 |
| 251.45 | 23.01 | 5.79 |
| 258.26 | 23.00 | 5.94 |
| 267.86 | 22.99 | 6.16 |
| 274.96 | 22.97 | 6.32 |
| 286.66 | 22.93 | 6.57 |
| 289.57 | 22.93 | 6.64 |
| 296.35 | 22.92 | 6.79 |
| 307.47 | 22.90 | 7.04 |
| 310.22 | 22.89 | 7.10 |
| 321.92 | 22.86 | 7.36 |
| 326.47 | 22.84 | 7.46 |
| 339.05 | 22.81 | 7.73 |
| 339.98 | 22.81 | 7.75 |
| 352.01 | 22.75 | 8.01 |

| Spannung *Voltage* / mV | Strom *Current* / mA | Leistung *Power* / mW |
|---|---|---|
| 353.91 | 22.74 | 8.05 |
| 365.61 | 22.68 | 8.29 |
| 366.61 | 22.68 | 8.31 |
| 379.03 | 22.61 | 8.57 |
| 379.94 | 22.60 | 8.59 |
| 387.71 | 22.54 | 8.74 |
| 391.52 | 22.52 | 8.82 |
| 400.70 | 22.44 | 8.99 |
| 402.00 | 22.43 | 9.02 |
| 409.52 | 22.34 | 9.15 |
| 411.49 | 22.32 | 9.18 |
| 418.04 | 22.25 | 9.30 |
| 419.79 | 22.23 | 9.33 |
| 426.56 | 22.15 | 9.45 |
| 428.95 | 22.11 | 9.48 |
| 432.71 | 22.02 | 9.53 |
| 434.67 | 21.98 | 9.56 |
| 439.99 | 21.89 | 9.63 |
| 443.16 | 21.84 | 9.68 |
| 446.79 | 21.77 | 9.73 |
| 449.52 | 21.71 | 9.76 |
| 452.43 | 21.64 | 9.79 |
| 454.78 | 21.57 | 9.81 |
| 457.61 | 21.49 | 9.84 |
| 459.71 | 21.43 | 9.85 |
| 462.90 | 21.34 | 9.88 |
| 464.70 | 21.29 | 9.89 |
| 467.22 | 21.21 | 9.91 |
| 469.23 | 21.14 | 9.92 |
| 470.98 | 21.07 | 9.93 |
| 473.79 | 20.97 | 9.94 |
| 475.17 | 20.91 | 9.94 |
| 476.96 | 20.82 | 9.93 |
| 478.12 | 20.77 | 9.93 |
| 480.50 | 20.67 | 9.93 |
| 482.09 | 20.60 | 9.93 |
| 483.87 | 20.52 | 9.93 |
| 485.27 | 20.44 | 9.92 |
| 487.06 | 20.35 | 9.91 |
| 488.11 | 20.29 | 9.90 |
| 489.98 | 20.18 | 9.89 |
| 491.24 | 20.12 | 9.88 |
| 493.30 | 19.99 | 9.86 |
| 493.55 | 19.97 | 9.86 |
| 496.33 | 19.82 | 9.84 |
| 496.52 | 19.81 | 9.84 |
| 498.57 | 19.67 | 9.80 |
| 498.93 | 19.64 | 9.80 |
| 500.89 | 19.49 | 9.76 |
| 500.99 | 19.49 | 9.76 |
| 503.19 | 19.33 | 9.73 |

Fraunhofer ISE

1003015EMP0118

CalLab
PV Cells

| Spannung *Voltage* / mV | Strom *Current* / mA | Leistung *Power* / mW |
|---|---|---|
| 503.58 | 19.30 | 9.72 |
| 505.68 | 19.16 | 9.69 |
| 505.84 | 19.14 | 9.68 |
| 507.52 | 19.00 | 9.64 |
| 507.70 | 18.98 | 9.64 |
| 509.68 | 18.81 | 9.59 |
| 509.73 | 18.81 | 9.59 |
| 511.69 | 18.65 | 9.55 |
| 511.86 | 18.64 | 9.54 |
| 513.49 | 18.48 | 9.49 |
| 513.56 | 18.47 | 9.49 |
| 515.21 | 18.30 | 9.43 |
| 515.33 | 18.29 | 9.43 |
| 516.98 | 18.14 | 9.38 |
| 517.21 | 18.12 | 9.37 |
| 518.46 | 17.99 | 9.32 |
| 519.02 | 17.93 | 9.31 |
| 520.33 | 17.80 | 9.26 |
| 520.66 | 17.77 | 9.25 |
| 521.82 | 17.63 | 9.20 |
| 522.18 | 17.58 | 9.18 |
| 523.08 | 17.46 | 9.13 |
| 523.47 | 17.41 | 9.11 |
| 524.46 | 17.29 | 9.07 |
| 524.96 | 17.23 | 9.05 |
| 526.10 | 17.10 | 9.00 |
| 526.37 | 17.07 | 8.98 |
| 527.35 | 16.94 | 8.93 |
| 527.91 | 16.88 | 8.91 |
| 528.76 | 16.77 | 8.87 |
| 529.23 | 16.71 | 8.84 |
| 530.10 | 16.59 | 8.80 |
| 530.66 | 16.52 | 8.76 |
| 531.28 | 16.43 | 8.73 |
| 532.15 | 16.32 | 8.68 |
| 532.60 | 16.26 | 8.66 |
| 533.33 | 16.15 | 8.62 |
| 533.93 | 16.07 | 8.58 |
| 534.73 | 15.96 | 8.54 |
| 535.11 | 15.91 | 8.51 |
| 535.90 | 15.79 | 8.46 |
| 536.32 | 15.72 | 8.43 |
| 536.97 | 15.62 | 8.39 |
| 537.40 | 15.55 | 8.36 |
| 538.19 | 15.43 | 8.30 |
| 538.57 | 15.37 | 8.28 |
| 539.36 | 15.24 | 8.22 |
| 539.59 | 15.20 | 8.20 |
| 540.54 | 15.05 | 8.14 |
| 540.65 | 15.03 | 8.13 |
| 541.58 | 14.88 | 8.06 |

| Spannung *Voltage* / mV | Strom *Current* / mA | Leistung *Power* / mW |
|---|---|---|
| 541.79 | 14.85 | 8.05 |
| 542.71 | 14.69 | 7.97 |
| 542.83 | 14.67 | 7.96 |
| 543.65 | 14.52 | 7.89 |
| 543.88 | 14.48 | 7.88 |
| 544.75 | 14.33 | 7.81 |
| 544.76 | 14.33 | 7.80 |
| 545.78 | 14.15 | 7.72 |
| 545.79 | 14.15 | 7.72 |
| 546.75 | 13.98 | 7.64 |
| 546.84 | 13.96 | 7.63 |
| 547.70 | 13.79 | 7.55 |
| 547.78 | 13.78 | 7.55 |
| 548.67 | 13.61 | 7.47 |
| 548.68 | 13.61 | 7.47 |
| 549.51 | 13.44 | 7.39 |
| 549.68 | 13.41 | 7.37 |
| 550.55 | 13.25 | 7.30 |
| 550.67 | 13.23 | 7.29 |
| 551.41 | 13.07 | 7.20 |
| 551.44 | 13.06 | 7.20 |
| 552.31 | 12.89 | 7.12 |
| 552.41 | 12.87 | 7.11 |
| 553.15 | 12.71 | 7.03 |
| 553.27 | 12.69 | 7.02 |
| 553.96 | 12.54 | 6.95 |
| 554.23 | 12.49 | 6.92 |
| 554.85 | 12.35 | 6.85 |
| 554.99 | 12.32 | 6.84 |
| 555.72 | 12.17 | 6.76 |
| 555.80 | 12.15 | 6.75 |
| 556.59 | 11.99 | 6.67 |
| 556.73 | 11.96 | 6.66 |
| 557.31 | 11.82 | 6.59 |
| 557.57 | 11.77 | 6.56 |
| 558.12 | 11.63 | 6.49 |
| 558.29 | 11.59 | 6.47 |
| 559.00 | 11.44 | 6.40 |
| 559.16 | 11.41 | 6.38 |
| 559.77 | 11.26 | 6.30 |
| 559.90 | 11.23 | 6.29 |
| 560.49 | 11.10 | 6.22 |
| 560.84 | 11.02 | 6.18 |
| 561.24 | 10.92 | 6.13 |
| 561.59 | 10.84 | 6.09 |
| 561.91 | 10.75 | 6.04 |
| 562.34 | 10.65 | 5.99 |
| 562.71 | 10.56 | 5.94 |
| 563.10 | 10.47 | 5.90 |
| 563.51 | 10.37 | 5.84 |
| 563.81 | 10.29 | 5.80 |

Fraunhofer ISE

1003015EMP0118

CalLab PV Cells

| Spannung *Voltage* / mV | Strom *Current* / mA | Leistung *Power* / mW |
|---|---|---|
| 564.22 | 10.19 | 5.75 |
| 564.47 | 10.12 | 5.71 |
| 564.94 | 10.00 | 5.65 |
| 565.18 | 9.94 | 5.62 |
| 565.60 | 9.82 | 5.56 |
| 565.90 | 9.75 | 5.52 |
| 566.30 | 9.65 | 5.46 |
| 566.66 | 9.56 | 5.41 |
| 566.98 | 9.47 | 5.37 |
| 567.31 | 9.38 | 5.32 |
| 567.65 | 9.28 | 5.27 |
| 567.96 | 9.20 | 5.22 |
| 568.35 | 9.09 | 5.16 |
| 568.61 | 8.99 | 5.11 |
| 568.71 | 8.95 | 5.09 |
| 569.18 | 8.80 | 5.01 |
| 569.36 | 8.75 | 4.98 |
| 569.85 | 8.61 | 4.91 |
| 570.00 | 8.57 | 4.89 |
| 570.56 | 8.43 | 4.81 |
| 570.69 | 8.39 | 4.79 |
| 571.21 | 8.25 | 4.71 |
| 571.42 | 8.19 | 4.68 |
| 571.77 | 8.08 | 4.62 |
| 572.03 | 8.01 | 4.58 |
| 572.41 | 7.89 | 4.52 |
| 572.58 | 7.84 | 4.49 |
| 573.10 | 7.69 | 4.40 |
| 573.18 | 7.66 | 4.39 |
| 573.65 | 7.51 | 4.31 |
| 573.74 | 7.48 | 4.29 |
| 574.33 | 7.31 | 4.20 |
| 574.38 | 7.30 | 4.19 |
| 574.89 | 7.13 | 4.10 |
| 574.91 | 7.12 | 4.09 |
| 575.46 | 6.96 | 4.00 |
| 575.60 | 6.92 | 3.98 |
| 576.20 | 6.76 | 3.89 |
| 576.21 | 6.75 | 3.89 |
| 576.71 | 6.57 | 3.79 |
| 576.73 | 6.57 | 3.79 |
| 577.16 | 6.42 | 3.70 |
| 577.39 | 6.36 | 3.67 |
| 577.95 | 6.21 | 3.59 |
| 578.02 | 6.19 | 3.58 |
| 578.55 | 6.02 | 3.48 |
| 578.56 | 6.02 | 3.48 |
| 579.12 | 5.83 | 3.38 |
| 579.58 | 5.67 | 3.29 |
| 579.73 | 5.62 | 3.26 |
| 580.19 | 5.47 | 3.17 |

| Spannung *Voltage* / mV | Strom *Current* / mA | Leistung *Power* / mW |
|---|---|---|
| 580.23 | 5.46 | 3.17 |
| 580.72 | 5.29 | 3.07 |
| 580.78 | 5.27 | 3.06 |
| 581.32 | 5.10 | 2.97 |
| 581.40 | 5.08 | 2.95 |
| 581.86 | 4.92 | 2.86 |
| 581.93 | 4.90 | 2.85 |
| 582.41 | 4.73 | 2.75 |
| 582.43 | 4.72 | 2.75 |
| 582.94 | 4.54 | 2.65 |
| 582.97 | 4.53 | 2.64 |
| 583.48 | 4.37 | 2.55 |
| 583.62 | 4.33 | 2.53 |
| 583.99 | 4.19 | 2.45 |
| 584.11 | 4.15 | 2.42 |
| 584.48 | 4.01 | 2.34 |
| 584.62 | 3.96 | 2.31 |
| 585.00 | 3.83 | 2.24 |
| 585.19 | 3.77 | 2.21 |
| 585.62 | 3.63 | 2.13 |
| 585.71 | 3.60 | 2.11 |
| 586.15 | 3.44 | 2.02 |
| 586.19 | 3.42 | 2.01 |
| 586.67 | 3.26 | 1.91 |
| 586.75 | 3.23 | 1.90 |
| 587.21 | 3.07 | 1.80 |
| 587.26 | 3.05 | 1.79 |
| 587.63 | 2.91 | 1.71 |
| 587.82 | 2.84 | 1.67 |
| 588.20 | 2.70 | 1.59 |
| 588.24 | 2.68 | 1.58 |
| 588.65 | 2.51 | 1.48 |
| 588.68 | 2.50 | 1.47 |
| 589.12 | 2.33 | 1.37 |
| 589.21 | 2.30 | 1.36 |
| 589.70 | 2.13 | 1.26 |
| 589.72 | 2.13 | 1.25 |
| 590.09 | 1.96 | 1.16 |
| 590.18 | 1.93 | 1.14 |
| 590.60 | 1.79 | 1.05 |
| 590.76 | 1.73 | 1.02 |
| 591.10 | 1.60 | 0.95 |
| 591.25 | 1.55 | 0.91 |
| 591.57 | 1.42 | 0.84 |
| 591.76 | 1.35 | 0.80 |
| 592.01 | 1.24 | 0.74 |
| 592.19 | 1.18 | 0.70 |
| 592.59 | 1.03 | 0.61 |
| 592.67 | 1.00 | 0.59 |
| 593.07 | 0.85 | 0.51 |
| 593.17 | 0.82 | 0.48 |

Fraunhofer ISE

1003015EMP0118

CalLab
PV Cells

| Spannung *Voltage* / mV | Strom *Current* / mA | Leistung *Power* / mW |
|---|---|---|
| 593.61 | 0.65 | 0.39 |
| 593.64 | 0.64 | 0.38 |
| 593.99 | 0.48 | 0.29 |
| 594.11 | 0.44 | 0.26 |
| 594.52 | 0.28 | 0.17 |
| 594.56 | 0.27 | 0.16 |
| 594.97 | 0.11 | 0.06 |
| 595.06 | 0.07 | 0.04 |
| 595.41 | -0.08 | -0.05 |
| 595.49 | -0.12 | -0.07 |
| 595.78 | -0.27 | -0.16 |
| 595.83 | -0.29 | -0.17 |
| 596.31 | -0.46 | -0.28 |
| 596.33 | -0.47 | -0.28 |
| 596.69 | -0.64 | -0.38 |
| 596.74 | -0.66 | -0.40 |

## 6.Literatur
*Literature*

CalLab PV Cells

/1/ IEC 60904-1-Ed.2:2006, *Photovoltaic devices - Part 1: Measurement of photovoltaic current-voltage characteristics*

/2/ IEC 60904-3-Ed.1:1989, *Photovoltaic devices - Part 3: Measurement principles for terrestrial photovoltaic (PV) solar devices with reference spectral irradiance data*

/3/ IEC 60904-3-Ed.2:2008, *Photovoltaic devices - Part 3: Measurement principles for terrestrial photovoltaic (PV) solar devices with reference spectral irradiance data*

/4/ IEC 60904-7-Ed.3:2008, *Photovoltaic devices - Part 7: Computation of the spectral mismatch error introduced in the testing of a photovoltaic device*

/5/ IEC 60904-8-Ed.3:2014, *Photovoltaic devices - Part 8: Measurement of the spectral responsivity of a photovoltaic (PV) device*

/6/ IEC 60904-9-Ed.2:2010, *Photovoltaic devices - Part 9: Solar simulator performance requirements*

/7/ M.A. Green, K. Emery, Y. Hishikawa, W. Warta, and E. D. Dunlop, *Solar cell efficiency tables (version 39)*. Progress in Photovoltaics: Research and Applications, 2012. 20: p. 12-20.

# Bibliography


[1] T. Feurer, P. Reinhard, E. Avancini, B. Bissig, J. Löckinger, P. Fuchs, R. Carron, T. P. Weiss, J. Perrenoud, S. Stutterheim, S. Buecheler, and A. N. Tiwari, *Progress in thin film CIGS photovoltaics – Research and development, manufacturing, and applications*, Progress in Photovoltaics: Research and Applications **25**, 645 (2017).

[2] *World Energy Outlook 2018*, https://www.iea.org/weo2018/.

[3] *The Paris Agreement | UNFCCC*, https://unfccc.int/process-and-meetings/the-paris-agreement/d2hhdC1pcy.

[4] C. Kost, S. Shammugam, V. Jülch, H.-T. Nguyen, and T. Schlegl, *Levelized Cost of Electricity- Renewable Energy Technologies*, p. 42.

[5] F. Ise, *Photovoltaics Report*, p. 47.

[6] W. M. Soares, D. D. Athayde, and E. H. M. Nunes, *LCA study of photovoltaic systems based on different technologies*, International Journal of Green Energy **15**, 577 (2018).

[7] G. Makrides, B. Zinsser, M. Norton, G. E. Georghiou, M. Schubert, and J. H. Werner, *Potential of photovoltaic systems in countries with high solar irradiation*, Renewable and Sustainable Energy Reviews **14**, 754 (2010).

[8] K. P. Bhandari, J. M. Collier, R. J. Ellingson, and D. S. Apul, *Energy payback time (EPBT) and energy return on energy invested (EROI) of solar photovoltaic systems: A systematic review and meta-analysis*, Renewable and Sustainable Energy Reviews **47**, 133 (2015).

[9] *CIS advantages in real-world conditions*, http://www.solar-frontier.com/eng/technology/Performance/index.html.

[10] *CIGS White Paper Initiative – CIGS Thin-Film Photovoltaics*, http://cigs-pv.net/cigs-white-paper-initiative/.

[11] K. Otte, L. Makhova, A. Braun, and I. Konovalov, *Flexible Cu(In,Ga)Se2 thin-film solar cells for space application*, Thin Solid Films **511–512**, 613 (2006).

[12] *Solar Frontier Achieves World Record Thin-Film Solar Cell Efficiency of 23.35%*, http://www.solar-frontier.com/eng/news/2019/0117_press.html, 2019.

[13] S. Minoura, K. Kodera, T. Maekawa, K. Miyazaki, S. Niki, and H. Fujiwara, *Dielectric function of Cu(In, Ga)Se2-based polycrystalline materials*, Journal of Applied Physics **113**, 063505 (2013).

[14] R. Carron, E. Avancini, T. Feurer, B. Bissig, P. A. Losio, R. Figi, C. Schreiner, M. Bürki, E. Bourgeois, Z. Remes, M. Nesladek, S. Buecheler, and A. N. Tiwari, *Refractive indices of layers and optical simulations of Cu(In,Ga)Se2 solar cells*, Science and Technology of Advanced Materials **19**, 396 (2018).

[15] P. Jackson, R. Wuerz, D. Hariskos, E. Lotter, W. Witte, and M. Powalla, *Effects of heavy alkali elements in Cu(In,Ga)Se2 solar cells with efficiencies up to 22.6%*, physica status solidi (RRL) – Rapid Research Letters **10**, 583 (2016).

[16] J. S. Ward, B. Egaas, R. Noufi, M. Contreras, K. Ramanathan, C. Osterwald, and K. Emery, *Cu(In,Ga)Se2 solar cells measured under low flux optical concentration*, in *2014 IEEE 40th Photovoltaic Specialist Conference (PVSC)*, pp. 2934–2937, 2014.

[17] L. Mansfield, R. Noufi, C. Muzzillo, C. DeHart, K. Bowers, B. To, J. Pankow, R. Reedy, and K. Ramanathan, *Enhanced Performance in Cu(In,Ga)Se Solar Cells Fabricated by the Two-Step Selenization Process With a Potassium Fluoride Post-deposition Treatment*, IEEE Journal of Photovoltaics **4**, 1650 (2014).

[18] *CIGS Solar Cell with World's Highest Level Energy Conversion Efficiency*, https://www.toshiba.co.jp/rdc/rd/fields/14_e06_e.htm.

[19] R. Carron, S. Nishiwaki, T. Feurer, R. Hertwig, E. Avancini, J. Löckinger, S.-C. Yang, S. Buecheler, and A. N. Tiwari, *Advanced Alkali Treatments for High-Efficiency Cu(In,Ga)Se2 Solar Cells on Flexible Substrates*, Advanced Energy Materials **9**, 1900408 (2019).

[20] J. Nishinaga, T. Nagai, T. Sugaya, H. Shibata, and S. Niki, *Single-crystal Cu(In,Ga)Se2 solar cells grown on GaAs substrates*, Applied Physics Express **11**, 082302 (2018).

[21] C. P. Thompson, L. Chen, W. N. Shafarman, J. Lee, S. Fields, and R. W. Birkmire, *Bandgap gradients in (Ag,Cu)(In,Ga)Se2 thin film solar cells deposited by three-stage co-evaporation*, in *Photovoltaic Specialist Conference (PVSC), 2015 IEEE 42nd*, pp. 1–6, 2015.

[22] M. Nakamura, Y. Kouji, Y. Chiba, H. Hakuma, T. Kobayashi, and T. Nakada, *Achievement of 19.7% efficiency with a small-sized Cu(InGa)(SeS)2 solar cells prepared by sulfurization after selenizaion process with Zn-based buffer*, in *2013 IEEE 39th Photovoltaic Specialists Conference (PVSC)*, pp. 0849–0852, 2013.

[23] T. Kobayashi, H. Yamaguchi, and T. Nakada, *Effects of combined heat and light soaking on device performance of Cu(In,Ga)Se2 solar cells with ZnS(O,OH) buffer layer*, Progress in Photovoltaics: Research and Applications **22**, 115 (2014).

[24] J. Haarstrich, H. Metzner, M. Oertel, C. Ronning, T. Rissom, C. A. Kaufmann, T. Unold, H. W. Schock, J. Windeln, W. Mannstadt, and E. Rudigier-Voigt, *Increased homogeneity and open-circuit voltage of Cu(In,Ga)Se2 solar cells due to higher deposition temperature*, Solar Energy Materials and Solar Cells **95**, 1028 (2011).

[25] S. Merdes, F. Ziem, T. Lavrenko, T. Walter, I. Lauermann, M. Klingsporn, S. Schmidt, F. Hergert, and R. Schlatmann, *Above 16% efficient sequentially grown Cu(In,Ga)(Se,S)2-based solar cells with atomic layer deposited Zn(O,S) buffers*, Progress in Photovoltaics: Research and Applications , n/a (2015).

[26] J. Lindahl, U. Zimmermann, P. Szaniawski, T. Törndahl, A. Hultqvist, P. Salomé, C. Platzer-Björkman, and M. Edoff, *Inline Cu(In,Ga)Se Co-evaporation for High-Efficiency Solar Cells and Modules*, IEEE Journal of Photovoltaics **3**, 1100 (2013).

[27] C. Broussillou, C. Viscogliosi, A. Rogee, S. Angle, P. P. Grand, S. Bodnar, C. Debauche, J. L. Allary, B. Bertrand, C. Guillou, L. Parissi, and S. Coletti, *Statistical Process Control for Cu(In,Ga)(S,Se)2 electrodeposition-based manufacturing process of 60x120cm2 modules up to 14,0% efficiency*, in *Photovoltaic Specialist Conference (PVSC), 2015 IEEE 42nd*, pp. 1–5, 2015.

[28] R. N. Bhattacharya, *CIGS-based solar cells prepared from electrodeposited stacked Cu/In/Ga layers*, Solar Energy Materials and Solar Cells **113**, 96 (2013).

[29] T. K. Todorov, O. Gunawan, T. Gokmen, and D. B. Mitzi, *Solution-processed Cu(In,Ga)(S,Se)2 absorber yielding a 15.2% efficient solar cell*, Progress in Photovoltaics: Research and Applications **21**, 82 (2013).

[30] J. AbuShama, R. Noufi, S. Johnston, S. Ward, and X. Wu, *Improved performance in CuInSe2 and surface-modified CuGaSe2 solar cells*, in *Conference Record of the Thirty-First IEEE Photovoltaic Specialists Conference, 2005.*, pp. 299–302, 2005.

[31] S. Siebentritt, M. Igalson, C. Persson, and S. Lany, *The electronic structure of chalcopyrites—bands, point defects and grain boundaries*, Progress in Photovoltaics: Research and Applications **18**, 390 (2010).

[32] E. Korhonen, K. Kuitunen, F. Tuomisto, A. Urbaniak, M. Igalson, J. Larsen, L. Gütay, S. Siebentritt, and Y. Tomm, *Vacancy defects in epitaxial thin film CuGaSe2 and CuInSe2*, Physical Review B **86**, 064102 (2012).

[33] F. Werner, D. Colombara, M. Melchiorre, N. Valle, B. El Adib, C. Spindler, and S. Siebentritt, *Doping mechanism in pure CuInSe2*, Journal of Applied Physics **119**, 173103 (2016).

[34] P. Reinhard, A. Chirilă, P. Blösch, F. Pianezzi, S. Nishiwaki, S. Buecheler, and A. N. Tiwari, *Review of Progress Toward 20% Efficiency Flexible CIGS Solar Cells*

*and Manufacturing Issues of Solar Modules*, IEEE Journal of Photovoltaics **3**, 572 (2013).

[35] F. H. Pianezzi, *Electronic Transport and Doping Mechanisms in Cu(In,Ga)$Se_2$ Thin Film Solar Cells*, Doctoral Thesis, ETH Zurich, 2014.

[36] A. Chirilă, P. Reinhard, F. Pianezzi, P. Bloesch, A. R. Uhl, C. Fella, L. Kranz, D. Keller, C. Gretener, H. Hagendorfer, D. Jaeger, R. Erni, S. Nishiwaki, S. Buecheler, and A. N. Tiwari, *Potassium-induced surface modification of Cu(In,Ga)Se2 thin films for high-efficiency solar cells*, Nature Materials **12**, 1107 (2013).

[37] P. Jackson, D. Hariskos, R. Wuerz, O. Kiowski, A. Bauer, T. M. Friedlmeier, and M. Powalla, *Properties of Cu(In,Ga)Se2 solar cells with new record efficiencies up to 21.7%*, physica status solidi (RRL) – Rapid Research Letters **9**, 28 (2015).

[38] U. Rau, P. O. Grabitz, and J. H. Werner, *Resistive limitations to spatially inhomogeneous electronic losses in solar cells*, Applied Physics Letters **85**, 6010 (2004).

[39] N. Naghavi *et al.*, *Buffer layers and transparent conducting oxides for chalcopyrite Cu(In,Ga)(S,Se)2 based thin film photovoltaics: Present status and current developments*, Progress in Photovoltaics: Research and Applications **18**, 411 (2010).

[40] E. Fortunato, D. Ginley, H. Hosono, and D. C. Paine, *Transparent Conducting Oxides for Photovoltaics*, MRS Bulletin **32**, 242 (2007).

[41] S.-H. Wei and A. Zunger, *Band offsets and optical bowings of chalcopyrites and Zn-based II-VI alloys*, Journal of Applied Physics **78**, 3846 (1995).

[42] M. Contreras, J. Tuttle, D. Du, Y. Qi, A. Swartzlander, A. Tennant, and R. Noufi, *Graded band-gap Cu(In,Ga)Se2 thin-film solar cell absorber with enhanced open-circuit voltage*, Applied Physics Letters **63**, 1824 (1993).

[43] A. M. Gabor, J. R. Tuttle, D. S. Albin, M. A. Contreras, R. Noufi, and A. M. Hermann, *High-efficiency CuInxGa1-xSe2 solar cells made from (Inx,Ga1-x)2Se3 precursor films*, Applied Physics Letters **65**, 198 (1994).

[44] M. Marudachalam, R. W. Birkmire, H. Hichri, J. M. Schultz, A. Swartzlander, and M. M. Al-Jassim, *Phases, morphology, and diffusion in CuInxGa1-xSe2 thin films*, Journal of Applied Physics **82**, 2896 (1997).

[45] W. Witte *et al.*, *Gallium gradients in Cu(In,Ga)Se2 thin-film solar cells*, Progress in Photovoltaics: Research and Applications **23**, 717 (2015).

[46] S. Seyrling, A. Chirila, D. Güttler, F. Pianezzi, P. Rossbach, and A. N. Tiwari, *Modification of the three-stage evaporation process for CuIn1-xGaxSe2 absorber deposition*, Thin Solid Films **519**, 7232 (2011).

[47] P. Reinhard, F. Pianezzi, L. Kranz, S. Nishiwaki, A. Chirilă, S. Buecheler, and A. N. Tiwari, *Flexible Cu(In,Ga)Se2 solar cells with reduced absorber thickness*, Progress in Photovoltaics: Research and Applications **23**, 281 (2015).

[48] P. Szaniawski, P. Salomé, V. Fjällström, T. Törndahl, U. Zimmermann, and M. Edoff, *Influence of Varying Cu Content on Growth and Performance of Ga-Graded Cu(In,Ga)Se2 Solar Cells*, IEEE Journal of Photovoltaics **5**, 1775 (2015).

[49] B. Bissig, P. Reinhard, F. Pianezzi, H. Hagendorfer, S. Nishiwaki, S. Buecheler, and A. N. Tiwari, *Effects of NaF evaporation during low temperature Cu(In,Ga)Se2 growth*, Thin Solid Films **582**, 56 (2015).

[50] P. M. P. Salomé, H. Rodriguez-Alvarez, and S. Sadewasser, *Incorporation of alkali metals in chalcogenide solar cells*, Solar Energy Materials and Solar Cells **143**, 9 (2015).

[51] D. Rudmann, D. Brémaud, H. Zogg, and A. N. Tiwari, *Na incorporation into Cu(In,Ga)Se2 for high-efficiency flexible solar cells on polymer foils*, Journal of Applied Physics **97**, 084903 (2005).

[52] S. Nishiwaki, T. Satoh, Y. Hashimoto, T. Negami, and T. Wada, *Preparation of Cu(In,Ga)Se2 thin films at low substrate temperatures*, Journal of Materials Research **16**, 394 (2001).

[53] A. Chirilă, S. Buecheler, F. Pianezzi, P. Bloesch, C. Gretener, A. R. Uhl, C. Fella, L. Kranz, J. Perrenoud, S. Seyrling, R. Verma, S. Nishiwaki, Y. E. Romanyuk, G. Bilger, and A. N. Tiwari, *Highly efficient Cu(In,Ga)Se2 solar cells grown on flexible polymer films*, Nature Materials **10**, 857 (2011).

[54] T. Dullweber, G. H. anna, U. Rau, and H. W. Schock, *A new approach to high-efficiency solar cells by band gap grading in Cu(In,Ga)Se2 chalcopyrite semiconductors*, Solar Energy Materials and Solar Cells **67**, 145 (2001).

[55] R. Scheer and Hans-Werner Schock, *Chalcogenide Photovoltaics: Physics, Technologies, and Thin Film Devices* (Wiley, 2011).

[56] A. Niemegeers, M. Burgelman, R. Herberholz, U. Rau, D. Hariskos, and H.-W. Schock, *Model for electronic transport in Cu(In,Ga)Se2 solar cells*, Progress in Photovoltaics: Research and Applications **6**, 407 (1998).

[57] R. Klenk, *Characterisation and modelling of chalcopyrite solar cells*, Thin Solid Films **387**, 135 (2001).

[58] G. Sozzi, F. Troni, and R. Menozzi, *On the combined effects of window/buffer and buffer/absorber conduction-band offsets, buffer thickness and doping on thin-film solar cell performance*, Solar Energy Materials and Solar Cells **121**, 126 (2014).

[59] M. Gloeckler and J. R. Sites, *Band-gap grading in Cu(In,Ga)Se2 solar cells*, Journal of Physics and Chemistry of Solids **66**, 1891 (2005).

[60] K. Decock, S. Khelifi, and M. Burgelman, *Analytical versus numerical analysis of back grading in CIGS solar cells*, Solar Energy Materials and Solar Cells **95**, 1550 (2011).

[61] P. M. Salomé, V. Fjällström, P. Szaniawski, J. P. Leitão, A. Hultqvist, P. A. Fernandes, J. P. Teixeira, B. P. Falcão, U. Zimmermann, A. F. da Cunha, and M. Edoff, *A comparison between thin film solar cells made from co-evaporated CuIn1-xGaxSe2 using a one-stage process versus a three-stage process*, Progress in Photovoltaics: Research and Applications **23**, 470 (2015).

[62] R. Mainz, H. Rodriguez-Alvarez, M. Klaus, D. Thomas, J. Lauche, A. Weber, M. D. Heinemann, S. Brunken, D. Greiner, C. A. Kaufmann, T. Unold, H.-W. Schock, and C. Genzel, *Sudden stress relaxation in compound semiconductor thin films triggered by secondary phase segregation*, Physical Review B **92**, 155310 (2015).

[63] T. Nakada, H. Ohbo, T. Watanabe, H. Nakazawa, M. Matsui, and A. Kunioka, *Improved Cu(In,Ga)(S,Se)2 thin film solar cells by surface sulfurization*, Solar Energy Materials and Solar Cells **49**, 285 (1997).

[64] D. Ohashi, T. Nakada, and A. Kunioka, *Improved CIGS thin-film solar cells by surface sulfurization using In2S3 and sulfur vapor*, Solar Energy Materials and Solar Cells **67**, 261 (2001).

[65] T. Lavrenko, T. Ott, and T. Walter, *Impact of sulfur and gallium gradients on the performance of thin film Cu(In,Ga)(Se,S)2 solar cells*, Thin Solid Films **582**, 51 (2015).

[66] T. Kobayashi, H. Yamaguchi, Z. Jehl Li Kao, H. Sugimoto, T. Kato, H. Hakuma, and T. Nakada, *Impacts of surface sulfurization on Cu(In1-x,Gax)Se2 thin-film solar cells*, Progress in Photovoltaics: Research and Applications **23**, 1367 (2015).

[67] H. Hiroi, Y. Iwata, S. Adachi, H. Sugimoto, and A. Yamada, *New World-Record Efficiency for Pure-Sulfide Cu(In,Ga)S2 Thin-Film Solar Cell With Cd-Free Buffer Layer via KCN-Free Process*, IEEE Journal of Photovoltaics **6**, 760 (2016).

[68] J. Hedstrom, H. Ohlsen, M. Bodegard, A. Kylner, L. Stolt, D. Hariskos, M. Ruckh, and H. W. Schock, *Zno/Cds/Cu(in,Ga)Se2 Thin-Film Solar-Cells with Improved Performance*, Conference Record of the Twenty Third Ieee Photovoltaic Specialists Conference - 1993 , 364 (1993).

[69] D. Rudmann, D. Brémaud, A. F. da Cunha, G. Bilger, A. Strohm, M. Kaelin, H. Zogg, and A. N. Tiwari, *Sodium incorporation strategies for CIGS growth at different temperatures*, Thin Solid Films **480–481**, 55 (2005).

[70] M. Ruckh, D. Schmid, M. Kaiser, R. Schäffler, T. Walter, and H. W. Schock, *Influence of substrates on the electrical properties of Cu(In,Ga)Se2 thin films*, Solar Energy Materials and Solar Cells **41-42**, 335 (1996).

[71] D. Rudmann, A. F. da Cunha, M. Kaelin, F. Kurdesau, H. Zogg, A. N. Tiwari, and G. Bilger, *Efficiency enhancement of Cu(In,Ga)Se2 solar cells due to post-deposition Na incorporation*, Applied Physics Letters **84**, 1129 (2004).

[72] R. Caballero, C. A. Kaufmann, T. Eisenbarth, M. Cancela, R. Hesse, T. Unold, A. Eicke, R. Klenk, and H. W. Schock, *The influence of Na on low temperature growth of CIGS thin film solar cells on polyimide substrates*, Thin Solid Films **517**, 2187 (2009).

[73] M. A. Contreras, B. Egaas, P. Dippo, J. Webb, J. Granata, K. Ramanathan, S. Asher, A. Swartzlander, and R. Noufi, *On the role of Na and modifications to Cu(In,Ga)Se/sub 2/ absorber materials using thin-MF (M=Na, K, Cs) precursor layers [solar cells]*, in *Conference Record of the Twenty Sixth IEEE Photovoltaic Specialists Conference - 1997*, pp. 359–362, 1997.

[74] L. Kronik, D. Cahen, and H. W. Schock, *Effects of Sodium on Polycrystalline Cu(In,Ga)Se2 and Its Solar Cell Performance*, Advanced Materials **10**, 31 (1998).

[75] Z.-K. Yuan, S. Chen, Y. Xie, J.-S. Park, H. Xiang, X.-G. Gong, and S.-H. Wei, *Na-Diffusion Enhanced p-type Conductivity in Cu(In,Ga)Se2: A New Mechanism for Efficient Doping in Semiconductors*, Advanced Energy Materials **6**, 1601191 (2016).

[76] F. Pianezzi, P. Reinhard, A. Chirilă, B. Bissig, S. Nishiwaki, S. Buecheler, and A. N. Tiwari, *Unveiling the effects of post-deposition treatment with different alkaline elements on the electronic properties of CIGS thin film solar cells*, Physical Chemistry Chemical Physics **16**, 8843 (2014).

[77] R. Kamada, T. Yagioka, S. Adachi, A. Handa, K. F. Tai, T. Kato, and H. Sugimoto, *New world record Cu(In, Ga)(Se, S)2 thin film solar cell efficiency beyond 22%*, in *2016 IEEE 43rd Photovoltaic Specialists Conference (PVSC)*, pp. 1287–1291, 2016.

[78] P.-P. Choi, O. Cojocaru-Mirédin, R. Wuerz, and D. Raabe, *Comparative atom probe study of Cu(In,Ga)Se2 thin-film solar cells deposited on soda-lime glass and mild steel substrates*, Journal of Applied Physics **110**, 124513 (2011).

[79] O. Cojocaru-Mirédin, T. Schwarz, P.-P. Choi, M. Herbig, R. Wuerz, and D. Raabe, *Atom Probe Tomography Studies on the Cu(In,Ga)Se2 Grain Boundaries*, Journal of Visualized Experiments : JoVE (2013).

[80] A. Vilalta-Clemente, M. Raghuwanshi, S. Duguay, C. Castro, E. Cadel, P. Pareige, P. Jackson, R. Wuerz, D. Hariskos, and W. Witte, *Rubidium distribution at atomic scale in high efficient Cu(In,Ga)Se2 thin-film solar cells*, Applied Physics Letters **112**, 103105 (2018).

[81] P. Reinhard, B. Bissig, F. Pianezzi, E. Avancini, H. Hagendorfer, D. Keller, P. Fuchs, M. Döbeli, C. Vigo, P. Crivelli, S. Nishiwaki, S. Buecheler, and A. N. Tiwari, *Features of KF and NaF Postdeposition Treatments of Cu(In,Ga)Se2 Absorbers for High Efficiency Thin Film Solar Cells*, Chemistry of Materials (2015).

[82] A. Laemmle, R. Wuerz, and M. Powalla, *Efficiency enhancement of Cu(In,Ga)Se2 thin-film solar cells by a post-deposition treatment with potassium fluoride*, physica status solidi (RRL) – Rapid Research Letters **7**, 631 (2013).

[83] E. Avancini, R. Carron, T. P. Weiss, C. Andres, M. Bürki, C. Schreiner, R. Figi, Y. E. Romanyuk, S. Buecheler, and A. N. Tiwari, *Effects of Rubidium Fluoride and Potassium Fluoride Postdeposition Treatments on Cu(In,Ga)Se2 Thin Films and Solar Cell Performance*, Chemistry of Materials **29**, 9695 (2017).

[84] P. Jackson, D. Hariskos, R. Wuerz, O. Kiowski, A. Bauer, and M. Powalla, *Properties of high efficiency Cu (In, Ga) Se2 solar cells*, in *MRS Spring Meeting & Exhibit, San Francisco B* Vol. 7, 2015.

[85] P. Reinhard, F. Pianezzi, B. Bissig, A. Chirila, P. Blosch, S. Nishiwaki, S. Buecheler, and A. Tiwari, *Cu(In,Ga)Se Thin-Film Solar Cells and Modules - A Boost in Efficiency Due to Potassium*, IEEE Journal of Photovoltaics **5**, 656 (2015).

[86] P. Jackson, D. Hariskos, R. Wuerz, W. Wischmann, and M. Powalla, *Compositional investigation of potassium doped Cu(In,Ga)Se2 solar cells with efficiencies up to 20.8%*, physica status solidi (RRL) – Rapid Research Letters **8**, 219 (2014).

[87] C. P. Muzzillo, J. D. Poplawsky, H. M. Tong, W. Guo, and T. Anderson, *Revealing the beneficial role of K in grain interiors, grain boundaries, and at the buffer interface for highly efficient CuInSe2 solar cells*, Progress in Photovoltaics: Research and Applications **26**, 825 (2018).

[88] M. Malitckaya, H.-P. Komsa, V. Havu, and M. J. Puska, *Effect of Alkali Metal Atom Doping on the CuInSe2-Based Solar Cell Absorber*, The Journal of Physical Chemistry C **121**, 15516 (2017).

[89] N. Taguchi, S. Tanaka, and S. Ishizuka, *Direct insights into RbInSe2 formation at Cu(In,Ga)Se2 thin film surface with RbF postdeposition treatment*, Applied Physics Letters **113**, 113903 (2018).

[90] M. H. Wolter, B. Bissig, E. Avancini, R. Carron, S. Buecheler, P. Jackson, and S. Siebentritt, *Influence of Sodium and Rubidium Postdeposition Treatment on the Quasi-Fermi Level Splitting of Cu(In,Ga)Se2Thin Films*, IEEE Journal of Photovoltaics **8**, 1320 (2018).

[91] *Reference Air Mass 1.5 Spectra | Grid Modernization | NREL*, https://www.nrel.gov/grid/solar-resource/spectra-am1.5.html.

[92] W. Shockley and H. J. Queisser, *Detailed Balance Limit of Efficiency of p-n Junction Solar Cells*, Journal of Applied Physics **32**, 510 (1961).

[93] A. Polman and H. A. Atwater, *Photonic design principles for ultrahigh-efficiency photovoltaics*, Nature Materials **11**, 174 (2012).

[94] A. D. Vos, *Detailed balance limit of the efficiency of tandem solar cells*, Journal of Physics D: Applied Physics **13**, 839 (1980).

[95] F. Dimroth *et al.*, *Four-Junction Wafer-Bonded Concentrator Solar Cells*, IEEE Journal of Photovoltaics **6**, 343 (2016).

[96] J. Werner, G. Nogay, F. Sahli, T. C.-J. Yang, M. Bräuninger, G. Christmann, A. Walter, B. A. Kamino, P. Fiala, P. Löper, S. Nicolay, Q. Jeangros, B. Niesen, and C. Ballif, *Complex Refractive Indices of Cesium–Formamidinium-Based Mixed-Halide Perovskites with Optical Band Gaps from 1.5 to 1.8 eV*, ACS Energy Letters **3**, 742 (2018).

[97] X. Wu, J. Zhou, A. Duda, J. C. Keane, T. Gessert, Y. Yan, and R. Noufi, *High-Efficiency CdTe Polycrystalline Thin-Film Solar Cells with an Ultra-Thin CuxTe Transparent Back-Contact*, in *Symposium F – Thin-Film Compound Semiconductor Photovoltaics*, , MRS Online Proceedings Library Archive Vol. 865, p. F114 (6 pages), 2005.

[98] L. Kranz, A. Abate, T. Feurer, F. Fu, E. Avancini, J. Löckinger, P. Reinhard, S. M. Zakeeruddin, M. Grätzel, S. Buecheler, and A. N. Tiwari, *High-Efficiency Polycrystalline Thin Film Tandem Solar Cells*, The Journal of Physical Chemistry Letters **6**, 2676 (2015).

[99] T. Todorov, T. Gershon, O. Gunawan, Y. S. Lee, C. Sturdevant, L.-Y. Chang, and S. Guha, *Monolithic Perovskite-CIGS Tandem Solar Cells via In Situ Band Gap Engineering*, Advanced Energy Materials **5** (2015).

[100] S. H. Moon, S. J. Park, S. H. Kim, M. W. Lee, J. Han, J. Y. Kim, H. Kim, Y. J. Hwang, D.-K. Lee, and B. K. Min, *Monolithic DSSC/CIGS tandem solar cell fabricated by a solution process*, Scientific Reports **5** (2015).

[101] S. Wenger, S. Seyrling, A. N. Tiwari, and M. Grätzel, *Fabrication and performance of a monolithic dye-sensitized TiO2/Cu(In,Ga)Se2 thin film tandem solar cell*, Applied Physics Letters **94**, 173508 (2009).

[102] Q. Han, Y.-T. Hsieh, L. Meng, J.-L. Wu, P. Sun, E.-P. Yao, S.-Y. Chang, S.-H. Bae, T. Kato, V. Bermudez, and Y. Yang, *High-performance perovskite/Cu(In,Ga)Se2 monolithic tandem solar cells*, Science **361**, 904 (2018).

[103] F. Fu, T. Feurer, T. Jäger, E. Avancini, B. Bissig, S. Yoon, S. Buecheler, and A. N. Tiwari, *Low-temperature-processed efficient semi-transparent planar perovskite solar*

*cells for bifacial and tandem applications*, Nature Communications **6**, 8932 (2015).

[104] C. D. Bailie, M. G. Christoforo, J. P. Mailoa, A. R. Bowring, E. L. Unger, W. H. Nguyen, J. Burschka, N. Pellet, J. Z. Lee, M. Grätzel, R. Noufi, T. Buonassisi, A. Salleo, and M. D. McGehee, *Semi-transparent perovskite solar cells for tandems with silicon and CIGS*, Energy Environ. Sci. **8**, 956 (2015).

[105] F. Hao, C. C. Stoumpos, R. P. H. Chang, and M. G. Kanatzidis, *Anomalous Band Gap Behavior in Mixed Sn and Pb Perovskites Enables Broadening of Absorption Spectrum in Solar Cells*, Journal of the American Chemical Society **136**, 8094 (2014).

[106] E. L. Unger, L. Kegelmann, K. Suchan, D. Sörell, L. Korte, and S. Albrecht, *Roadmap and roadblocks for the band gap tunability of metal halide perovskites*, Journal of Materials Chemistry A **5**, 11401 (2017).

[107] J. H. Noh, S. H. Im, J. H. Heo, T. N. Mandal, and S. I. Seok, *Chemical Management for Colorful, Efficient, and Stable Inorganic–Organic Hybrid Nanostructured Solar Cells*, Nano Letters **13**, 1764 (2013).

[108] H. J. Snaith, A. Abate, J. M. Ball, G. E. Eperon, T. Leijtens, N. K. Noel, S. D. Stranks, J. T.-W. Wang, K. Wojciechowski, and W. Zhang, *Anomalous Hysteresis in Perovskite Solar Cells*, The Journal of Physical Chemistry Letters **5**, 1511 (2014).

[109] Y. Han, S. Meyer, Y. Dkhissi, K. Weber, J. M. Pringle, U. Bach, L. Spiccia, and Y.-B. Cheng, *Degradation observations of encapsulated planar CH 3 NH 3 PbI 3 perovskite solar cells at high temperatures and humidity*, Journal of Materials Chemistry A **3**, 8139 (2015).

[110] M. Saliba, T. Matsui, J.-Y. Seo, K. Domanski, J.-P. Correa-Baena, M. Khaja Nazeeruddin, S. M. Zakeeruddin, W. Tress, A. Abate, A. Hagfeldt, and M. Grätzel, *Cesium-containing triple cation perovskite solar cells: Improved stability, reproducibility and high efficiency*, Energy & Environmental Science **9**, 1989 (2016).

[111] B. Roose, Q. Wang, and A. Abate, *The Role of Charge Selective Contacts in Perovskite Solar Cell Stability*, Advanced Energy Materials **9**, 1803140 (2019).

[112] *Best Research-Cell Efficiency Chart | Photovoltaic Research | NREL*, https://www.nrel.gov/pv/cell-efficiency.html.

[113] H. Shen, T. Duong, J. Peng, D. Jacobs, N. Wu, J. Gong, Y. Wu, S. Krishna Karuturi, X. Fu, K. Weber, X. Xiao, T. P. White, and K. Catchpole, *Mechanically-stacked perovskite/CIGS tandem solar cells with efficiency of 23.9% and reduced oxygen sensitivity*, Energy & Environmental Science **11**, 394 (2018).

[114] M. L. Petrus, J. Schlipf, C. Li, T. P. Gujar, N. Giesbrecht, P. Müller-Buschbaum, M. Thelakkat, T. Bein, S. Hüttner, and P. Docampo, *Capturing the Sun: A Review of the Challenges and Perspectives of Perovskite Solar Cells*, Advanced Energy Materials **7**, 1700264 (2017).

[115] Z. Wang, Z. Song, Y. Yan, S. F. Liu, and D. Yang, *Perovskite—a Perfect Top Cell for Tandem Devices to Break the S–Q Limit*, Advanced Science **0**, 1801704.

[116] T. Feurer, B. Bissig, T. P. Weiss, R. Carron, E. Avancini, J. Löckinger, S. Buecheler, and A. N. Tiwari, *Single-graded CIGS with narrow bandgap for tandem solar cells*, Science and Technology of Advanced Materials **19**, 263 (2018).

[117] T. Feurer, F. Fu, T. P. Weiss, E. Avancini, J. Löckinger, S. Buecheler, and A. N. Tiwari, *RbF post deposition treatment for narrow bandgap Cu(In,Ga)Se2 solar cells*, Thin Solid Films **670**, 34 (2019).

[118] J. Löckinger, S. Nishiwaki, P. Fuchs, S. Buecheler, Y. E. Romanyuk, and A. N. Tiwari, *New sulphide precursors for Zn(O,S) buffer layers in Cu(In,Ga)Se2 solar cells for faster reaction kinetics*, Journal of Optics **18**, 084002 (2016).

[119] R. Carron, C. Andres, E. Avancini, T. Feurer, S. Nishiwaki, S. Pisoni, F. Fu, M. Lingg, Y. E. Romanyuk, S. Buecheler, and A. N. Tiwari, *Bandgap of thin film solar cell absorbers: A comparison of various determination methods*, Thin Solid Films **669**, 482 (2019).

[120] D. Abou-Ras, T. Kirchartz, and U. Rau, *Advanced Characterization Techniques for Thin Film Solar Cells* (Wiley-VCH Verlag GmbH & Co. KGaA, Weinheim, Germany, 2016).

[121] T. Walter, R. Herberholz, C. Müller, and H. W. Schock, *Determination of defect distributions from admittance measurements and application to Cu(In,Ga)Se2 based heterojunctions*, Journal of Applied Physics **80**, 4411 (1996).

[122] L. C. Kimerling, *Influence of deep traps on the measurement of free-carrier distributions in semiconductors by junction capacitance techniques*, Journal of Applied Physics **45**, 1839 (1974).

[123] B. Bissig, *Micro- and Macroscopic Characterization of Recombination Losses in High Efficiency Cu(In,Ga)Se2 Thin Film Solar Cells*, Doctoral Thesis, ETH Zurich, 2018.

[124] T. P. Weiss, B. Bissig, T. Feurer, R. Carron, S. Buecheler, and A. N. Tiwari, *Bulk and surface recombination properties in thin film semiconductors with different surface treatments from time-resolved photoluminescence measurements*, Scientific Reports **9**, 5385 (2019).

[125] O. Lundberg, M. Edoff, and L. Stolt, *The effect of Ga-grading in CIGS thin film solar cells*, Thin Solid Films **480–481**, 520 (2005).

[126] J. Song, S. S. Li, C. H. Huang, O. D. Crisalle, and T. J. Anderson, *Device modeling and simulation of the performance of Cu(In1-x,Gax)Se2 solar cells*, Solid-State Electronics **48**, 73 (2004).

[127] Y. Ando, S. Ishizuka, S. Wang, J. Chen, M. M. Islam, H. Shibata, K. Akimoto, and T. Sakurai, *Relationship between bandgap grading and carrier recombination for Cu(In,Ga)Se2-based solar cells*, Japanese Journal of Applied Physics **57**, 08RC08 (2018).

[128] T. Dullweber, O. Lundberg, J. Malmström, M. Bodegård, L. Stolt, U. Rau, H. W. Schock, and J. H. Werner, *Back surface band gap gradings in Cu(In,Ga)Se2 solar cells*, Thin Solid Films **387**, 11 (2001).

[129] M. Powalla *et al.*, *Advances in Cost-Efficient Thin-Film Photovoltaics Based on Cu(In,Ga)Se2*, Engineering **3**, 445 (2017).

[130] S. Rühle, *Tabulated values of the Shockley–Queisser limit for single junction solar cells*, Solar Energy **130**, 139 (2016).

[131] O. Lundberg, J. Lu, A. Rockett, M. Edoff, and L. Stolt, *Diffusion of indium and gallium in Cu(In,Ga)Se2 thin film solar cells*, Journal of Physics and Chemistry of Solids **64**, 1499 (2003).

[132] U. Rau, A. Jasenek, H. W. Schock, F. Engelhardt, and T. Meyer, *Electronic loss mechanisms in chalcopyrite based heterojunction solar cells*, Thin Solid Films **361**, 298 (2000).

[133] T. Dullweber, G. Hanna, W. Shams-Kolahi, A. Schwartzlander, M. A. Contreras, R. Noufi, and H. W. Schock, *Study of the effect of gallium grading in Cu(In,Ga)Se2*, Thin Solid Films **361-362**, 478 (2000).

[134] A. M. Gabor, J. R. Tuttle, M. H. Bode, A. Franz, A. L. Tennant, M. A. Contreras, R. Noufi, D. G. Jensen, and A. M. Hermann, *Band-gap engineering in Cu(In,Ga) Se2 thin films grown from (In,Ga)2Se3 precursors*, Solar Energy Materials and Solar Cells **41**, 247 (1996).

[135] S. Jung, S. Ahn, J. H. Yun, J. Gwak, D. Kim, and K. Yoon, *Effects of Ga contents on properties of CIGS thin films and solar cells fabricated by co-evaporation technique*, Current Applied Physics **10**, 990 (2010).

[136] S.-H. Wei, S. B. Zhang, and A. Zunger, *Effects of Ga addition to CuInSe2 on its electronic, structural, and defect properties*, Applied Physics Letters **72**, 3199 (1998).

[137] J. Verschraegen, M. Burgelman, and J. Penndorf, *Temperature dependence of the diode ideality factor in CuInS2-on-Cu-tape solar cells*, Thin Solid Films **480**, 307 (2005).

[138] O. Gunawan, T. Gokmen, and D. B. Mitzi, *Suns-VOC characteristics of high performance kesterite solar cells*, Journal of Applied Physics **116**, 084504 (2014).

[139] T. Orgis, M. Maiberg, and R. Scheer, *Influence of band gradients on Cu(In,Ga)Se2 solar cell diode factors*, Journal of Applied Physics **114**, 214506 (2013).

[140] T. Hölscher, S. Förster, T. Schneider, M. Maiberg, W. Widdra, and R. Scheer, *Light induced degradation of Cu(In,Ga)Se2 thin film surfaces*, Applied Physics Letters **111**, 011604 (2017).

[141] F. Fu, T. Feurer, T. P. Weiss, S. Pisoni, E. Avancini, C. Andres, S. Buecheler, and A. N. Tiwari, *High-efficiency inverted semi-transparent planar perovskite solar cells in substrate configuration*, Nature Energy **2**, 16190 (2016).

[142] D. J. Schroeder and A. A. Rockett, *Electronic effects of sodium in epitaxial CuIn1-xGaxSe2*, Journal of Applied Physics **82**, 4982 (1997).

[143] S.-H. Wei, S. B. Zhang, and A. Zunger, *Effects of Na on the electrical and structural properties of CuInSe2*, Journal of Applied Physics **85**, 7214 (1999).

[144] K. A. Sense and R. W. Stone, *Vapor Pressure and Molecular Composition of Vapors of the RbF–ZrF4 and LiF–ZrF4 Systems*, The Journal of Physical Chemistry **62**, 1411 (1958).

[145] T. P. Weiss, R. Carron, M. H. Wolter, J. Löckinger, E. Avancini, S. Siebentritt, S. Buecheler, and A. N. Tiwari, *Time-resolved photoluminescence on double graded Cu(In,Ga)Se2 – Impact of front surface recombination and its temperature dependence*, Science and Technology of Advanced Materials **20**, 313 (2019).

[146] H. Elanzeery, F. Babbe, M. Melchiorre, F. Werner, and S. Siebentritt, *High-performance low bandgap thin film solar cells for tandem applications*, Progress in Photovoltaics: Research and Applications **26**, 437 (2018).

[147] M. A. Green, Y. Hishikawa, E. D. Dunlop, D. H. Levi, J. Hohl-Ebinger, and A. W. Y. Ho-Baillie, *Solar cell efficiency tables (version 52)*, Progress in Photovoltaics: Research and Applications **26**, 427 (2018).

[148] R. R. King, D. Bhusari, A. Boca, D. Larrabee, X.-Q. Liu, W. Hong, C. M. Fetzer, D. C. Law, and N. H. Karam, *Band gap-voltage offset and energy production in*

*next-generation multijunction solar cells*, Progress in Photovoltaics: Research and Applications **19**, 797 (2010).

[149] T. Maeda, A. Kawabata, and T. Wada, *First-principles study on alkali-metal effect of Li, Na, and K in CuInSe2 and CuGaSe2*, Japanese Journal of Applied Physics **54**, 08KC20 (2015).

[150] T. Feurer, R. Carron, G. T. Sevilla, F. Fu, S. Pisoni, Y. E. Romanyuk, S. Buecheler, and A. N. Tiwari, *Efficiency Improvement of Near-Stoichiometric CuInSe2 Solar Cells for Application in Tandem Devices*, Advanced Energy Materials **0**, 1901428.

[151] H. J. Queisser, *Defects in Semiconductors: Some Fatal, Some Vital*, Science **281**, 945 (1998).

[152] *Defects in Semiconductors*, in *The Materials Science of Semiconductors*, edited by A. Rockett, pp. 289–356, Springer US, Boston, MA, 2008.

[153] P. Jackson, D. Hariskos, E. Lotter, S. Paetel, R. Wuerz, R. Menner, W. Wischmann, and M. Powalla, *New world record efficiency for Cu(In,Ga)Se2 thin-film solar cells beyond 20%*, Progress in Photovoltaics: Research and Applications **19**, 894 (2011).

[154] E. Wallin, U. Malm, T. Jarmar, O. L. Edoff, Marika, and L. Stolt, *World-record Cu(In,Ga)Se2-based thin-film sub-module with 17.4% efficiency*, Progress in Photovoltaics: Research and Applications **20**, 851 (2012).

[155] S. Siebentritt, L. Gütay, D. Regesch, Y. Aida, and V. Deprédurand, *Why do we make Cu(In,Ga)Se2 solar cells non-stoichiometric?*, Solar Energy Materials and Solar Cells **119**, 18 (2013).

[156] L. Gütay, D. Regesch, J. K. Larsen, Y. Aida, V. Depredurand, A. Redinger, S. Caneva, S. Schorr, C. Stephan, J. Vidal, S. Botti, and S. Siebentritt, *Feedback mechanism for the stability of the band gap of CuInSe2*, Physical Review B **86**, 045216 (2012).

[157] S. B. Zhang, S.-H. Wei, and A. Zunger, *Stabilization of Ternary Compounds via Ordered Arrays of Defect Pairs*, Physical Review Letters **78**, 4059 (1997).

[158] S. B. Zhang, S.-H. Wei, A. Zunger, and H. Katayama-Yoshida, *Defect physics of the CuInSe2 chalcopyrite semiconductor*, Physical Review B **57**, 9642 (1998).

[159] W. Witte, R. Kniese, and M. Powalla, *Raman investigations of Cu(In,Ga)Se2 thin films with various copper contents*, Thin Solid Films **517**, 867 (2008).

[160] A. Gerhard, W. Harneit, S. Brehme, A. Bauknecht, U. Fiedeler, M. C. Lux-Steiner, and S. Siebentritt, *Acceptor activation energies in epitaxial CuGaSe2 grown by MOVPE*, Thin Solid Films **387**, 67 (2001).

[161] S. Siebentritt, A. Gerhard, S. Brehme, and M. C. Lux-Steiner, *Composition dependent doping and transport properties of CuGaSe2*, MRS Online Proceedings Library Archive **668** (2001/ed).

[162] H.-J. Ko, G.-H. Lee, H.-J. Kim, M.-S. Han, C.-H. Jeong, J.-H. Lee, H.-S. Kim, J.-H. Kim, K.-B. Kim, and S.-H. Lee, *Investigation of high-quality CuInSe2 films with various Cu/In ratios*, Journal of Crystal Growth **322**, 91 (2011).

[163] Y. Aida, V. Depredurand, J. K. Larsen, H. Arai, D. Tanaka, M. Kurihara, and S. Siebentritt, *Cu-rich CuInSe2 solar cells with a Cu-poor surface*, Progress in Photovoltaics: Research and Applications **23**, 754 (2015).

[164] V. Deprédurand, D. Tanaka, Y. Aida, M. Carlberg, N. Fèvre, and S. Siebentritt, *Current loss due to recombination in Cu-rich CuInSe2 solar cells*, Journal of Applied Physics **115**, 044503 (2014).

[165] T. Bertram, V. Deprédurand, and S. Siebentritt, *In-Se surface treatment of Cu-rich grown CuInSe2*, in *2014 IEEE 40th Photovoltaic Specialist Conference (PVSC)*, pp. 3633–3636, 2014.

[166] M. Turcu, O. Pakma, and U. Rau, *Interdependence of absorber composition and recombination mechanism in Cu(In,Ga)(Se,S)2 heterojunction solar cells*, Applied Physics Letters **80**, 2598 (2002).

[167] H. Elanzeery, F. Babbe, M. Melchiorre, A. Zelenina, and S. Siebentritt, *Potassium Fluoride Ex Situ Treatment on Both Cu-Rich and Cu-Poor CuInSe2 Thin Film Solar Cells*, IEEE Journal of Photovoltaics **7**, 684 (2017).

[168] F. Babbe, H. Elanzeery, M. Melchiorre, A. Zelenina, and S. Siebentritt, *Potassium fluoride postdeposition treatment with etching step on both Cu-rich and Cu-poor CuInSe2 thin film solar cells*, Physical Review Materials **2**, 105405 (2018).

[169] H. Elanzeery, M. Melchiorre, M. Sood, F. Babbe, F. Werner, G. Brammertz, and S. Siebentritt, *Challenge in Cu-rich CuInSe2 thin film solar cells: Defect caused by etching*, Physical Review Materials **3**, 055403 (2019).

[170] D. Rudmann, *Effects of Sodium on Growth and Properties of Cu(In,Ga)$Se_2$ Thin Films and Solar Cells*, Doctoral Thesis, ETH Zurich, 2004.

[171] *Perovskite/CIGS tandem cell with Record Efficiency of 24.6 percent Paves the Way for Flexible Solar Cells and High-Efficiency Building-Integrated PV*, https://www.imec-int.com/en/articles/perovskite-cigs-tandem-cell-with-record-efficiency-of-24-6-percent, 2018.

[172] D. H. Kim *et al.*, *Bimolecular Additives Improve Wide-Band-Gap Perovskites for Efficient Tandem Solar Cells with CIGS*, Joule (2019).

[173] *Perovskite world record | Oxford PV*, https://www.oxfordpv.com/news/oxford-pv-perovskite-solar-cell-achieves-28-efficiency.

[174] M. Jaysankar, B. A. L. Raul, J. Bastos, C. Burgess, C. Weijtens, M. Creatore, T. Aernouts, Y. Kuang, R. Gehlhaar, A. Hadipour, and J. Poortmans, *Minimizing Voltage Loss in Wide-Bandgap Perovskites for Tandem Solar Cells*, ACS Energy Letters **4**, 259 (2019).

[175] M. Langenhorst, B. Sautter, R. Schmager, J. Lehr, E. Ahlswede, M. Powalla, U. Lemmer, B. S. Richards, and U. W. Paetzold, *Energy yield of all thin-film perovskite/CIGS tandem solar modules*, Progress in Photovoltaics: Research and Applications **27**, 290 (2019).

[176] S. E. Sofia, J. P. Mailoa, D. N. Weiss, B. J. Stanbery, T. Buonassisi, and I. M. Peters, *Economic viability of thin-film tandem solar modules in the United States*, Nature Energy , 1 (2018).